Universität Bremen

IMSAS

Development of the technological process for the production of the electrostatic curved beam actuator for pneumatic microvalves

Vom Fachbereich für Physik und Elektrotechnik
der Universität Bremen

zur Erlangung des akademischen Grades

Doktor-Ingenieur (Dr.-Ing.)

Genehmigte Dissertation

Von

M.Sc. Denis Petrov
Wohnhaft in Pinneberg

Referent:	Prof. Dr.-Ing. W. Benecke
Korreferent:	Prof. Dr.-Ing. W. Lang

Eingerichtet am: 21.05.2012
Tag des Promotionskolloquiums: 16.07.2012

Bremen
2012

To my wife

Table of contents

Abstract

This work focuses on the development of an effective technological process for the production of the electrostatic curved beam actuator capable to be used as a driving element in different devices such as microswitches or microvalves. Main attention was drawn to the investigation of electroplating technique as a critical process in the microactuator fabrication as well as to the design of the actuator. In addition, usability of ceramic substrates for the microactuator and microvalve production was examined. The idea behind it was that ceramic substrates can be preprocessed and delivered already with necessary electrical connections on it. This would make the entire production process simpler and cheaper. Several types of polished alumina (Al_2O_3) substrates were used for this purpose.

Electrostatic actuation principle was chosen for its good scaling properties to small dimensions, low power consumption, smaller size and higher switching speed. Curved shape of the actuator allows to reduce its pull-in voltage and thus to increase the amplitude of motion as compared to the parallel-plate structures. The material of the actuator is nickel. It was chosen for its good mechanical properties and relative simplicity of processing.

Double layer nickel electroplating was used to produce the microactuator. The layers have different stress gradients controlled by current density during the electroplating process, making it possible to achieve the desired bending of the structure. Compared to bimetallic bending cantilever actuators, the curvature of the single-metal beam is less dependable on temperature and aging. Thus, more stable performance under changing working conditions was ensured. In order to avoid sticking of the microactuator to the isolation layer in the closed state, an array of stand-off bumps was added on the back-side of the beam. These bumps reduce the contact area and increase the distance between the actuator and the isolation layer.

Fifteen design variants of the actuator differing in length and width were fabricated in order find the most effective solution for given system requirements. Based on the actuators technological process developed in this work, a simple electrostatic microvalve was designed and produced. Final variants of microvalve were fabricated on a standard 380 μm thick silicon wafer. Gas inlet channel as well as the electrodes and the actuator itself are all placed on the same substrate in order to reduce the size and cost of the system.

During characterization, mechanical stability of the actuators and microvalves were studied by means of drop, temperature and shear tests in order to prove the reliability of the system. System performance tests proved stable pull-in voltages from 8,6 V to 11,6 V. Maximal gas flow through the valve was 110±5 ml/min at applied differential pressure of 2 bar.

1 Chapter I: Introduction

1.1 MEMS: definition, applications, trends

This dissertation is dedicated to the design of a technological production process of an electrostatic microactuator. These devices belong to a broad family of **M**icro-**E**lectro-**M**echanical-**S**ystems or MEMS. Since 1970's they have become an important part of our life. Typically, modern MEMS is a combination of a micromechanical microoptical, or microfluidic part with microelectronic circuit that controls the performance of the system and serves as an interface for external units. Sometimes MEMS are referred to as microsystems. The prefix "micro" means that the dimensions of these devices lie in the micrometer range. The way to produce microsystems is called "microsystems technology" or MST. This technology combines the techniques of integrated circuits (IC) production with the micromachining of silicon, ceramics, glass and polymers.

The applications of MEMS are ubiquitous and one meets them every day at home, at work, or in the streets. It is expected that world MEMS market share will grow up from 8000 M$ in 2010 to approximately 19000 M$ by the year 2015 [1] in spite of global economy crisis. Taking into consideration that nowadays it takes only 3 to 4 years from first developments to first commercial products compared to about 10 years in the past, it is possible to assume that in the nearest future MEMS will totally influence human activities.

In general, there are seven basic MEMS application fields:

- automotive
- aeronautics
- consumer
- military
- industrial
- medical & life science,
- telecommunications

Detailed analysis and description of each MEMS application field is beyond the scope of this work. Thus, only several examples will be given. For instance, the airbag control system in a modern car begins with an acceleration/deceleration sensor or sensors and electronic circuits connected to it (Fig. 1.1).

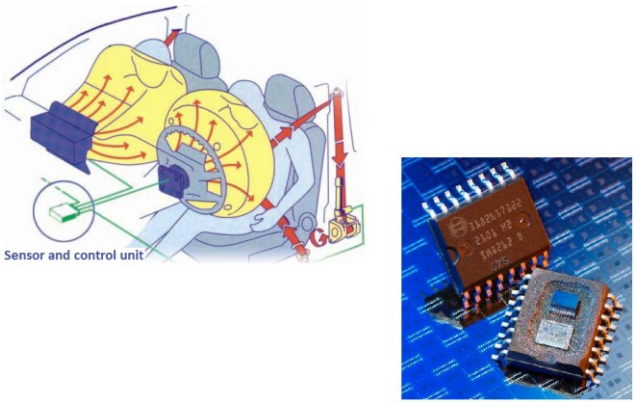

Figure 1.1: Airbag control system (left) and acceleration sensor in a package (right) [5]

The number of microdevices in a car is not restricted only with the above mentioned acceleration/deceleration sensor. Figure 1.2 illustrates the concept of so called "advanced safety vehicle"

equipped with a number of detection devices to improve its safety [2].

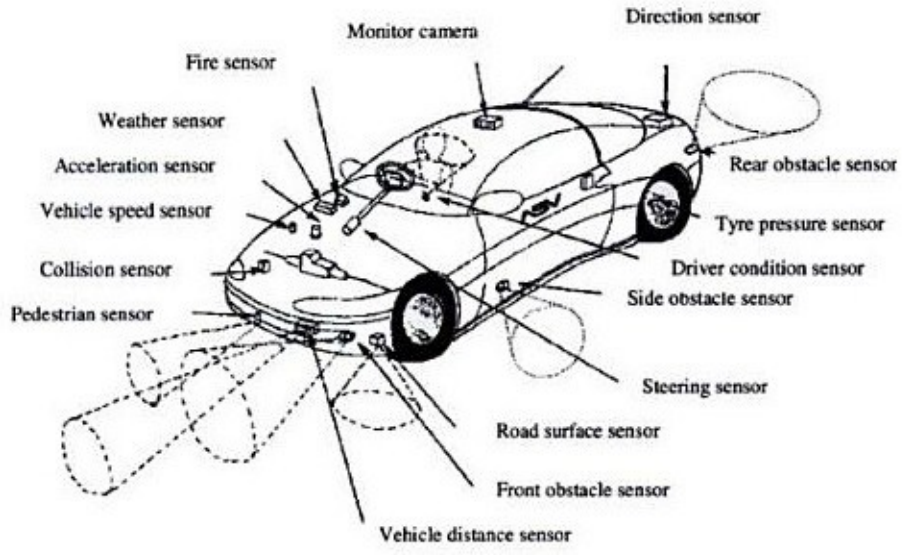

Figure 1.2: Current and future MEMS sensor applications in a car [2]

Another example would be a common ink-jet printer. Tiny nozzles and other elements of the print-head (Fig. 1.3) are fabricated using microsystem technology. Microaccelerometers and microgyroscopes can be met inside modern smartphones such as Apple iPhone, or in the controller of game consoles e.g. Nintendo Wii.

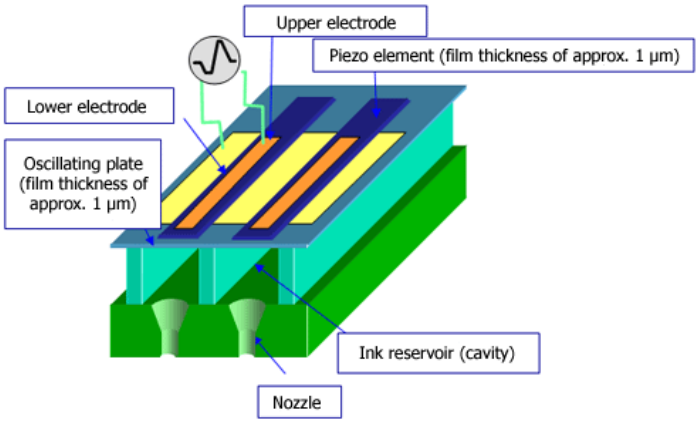

Figure 1.3: Cross-section of a print-head [3]

Microoptical components such as single microlenses, lens arrays, beam splitters, beam shapers, micromirrors and systems based on them can provide new functions impossible in conventional optical devices. Thus, a great number of new applications can emerge from the use of miniaturized optics. Among the examples fiber sensors and computer generated hologram can be named [4].

There are also more specific applications of MEMS. They are used in mobile chemical analysis equipment, such as chromatographs, environmental monitors, process control and medical diagnostic and drug delivery devices [6], [7]. Here, micro flow controllers or valves, micropumps and chemical sensors play an important role. Figure 1.4 demonstrates an instrument for a real-time polymerase chain-reaction (PCR) included a microfluidic modular cartridge with rotary microvalve [8].

Moreover, such systems are getting more and more common in high frequency applications. The most interesting examples in this area are mechanical filters or resonators, microswitches, varactors and inductors [9].

The first and the most obvious merit of microsystems is their small size (normally from 1 µm to a few mm). This leads to smaller and lighter devices, lower power consumption, increase of production volumes and consequent costs reduction. But miniaturization not only saves place and space, but also brings other advantages that broaden the borders of applicability of different physical principles.

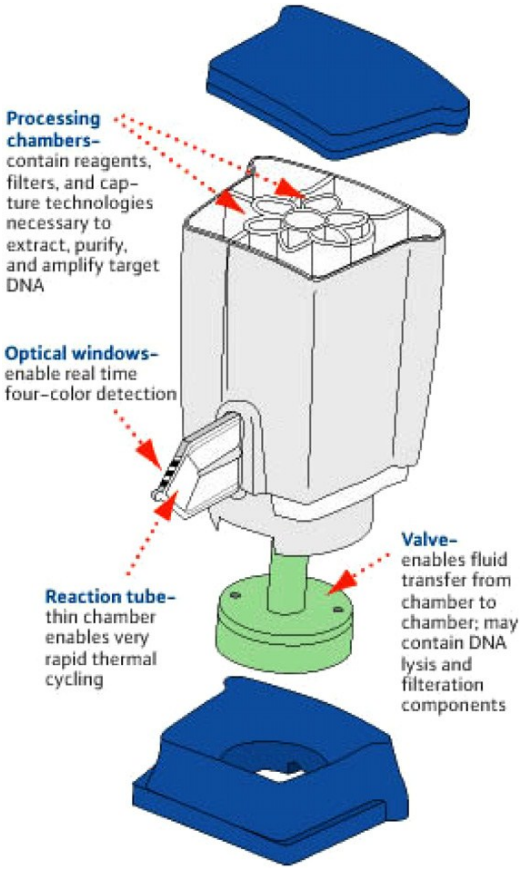

Figure 1.4: The GeneExpert cartridge with a rotary valve for sample preparation and real-time PCR [8]

It is known, for example, that electrostatic force between two charged particles is inversely proportional to the square of the distance between them. This makes it impossible to design large systems based on the electrostatic principle. On the contrary, microsystems widely use this physical effect. Pressure sensors are often built as variable capacitors that measure the pressure applied to one of the plates (diaphragm) by measuring the change in the distance between the plates. The latter is inversely proportional to the capacitance. Thus, narrow spacings must be used in order to receive reasonable output signal.

In medical, life science or chemical industry it is often necessary to analyze different chemical compounds. Except of already mentioned compactness of such units based on MEMS, they allow to use very small and precise amounts of chemicals for processing. This increases safety, effectiveness and extremely reduces costs as there is no need in large chemical storage facilities. Altogether, it results in greater product yield. Reduced volumes involved in the operations also increase the speed of reactants dilution or injection.

The scope of this work is the design of technological process for the production of the electrostatic curved beam actuator. Thus, it is necessary to pay more detailed attention to the basics of microactuator fabrication processes and to the current state of technology of microactuators and their applications.

1.2 Overview of the basic microfabrication techniques

In this subsection, a brief description of basic MEMS technologies and their relation to the topic of this work is given.

Normally, microactuator fabrication can involve a lot of MEMS bulk and surface micromachining production techniques. Figure 1.5 shows examples of simple bulk and surface micromachining sequences.

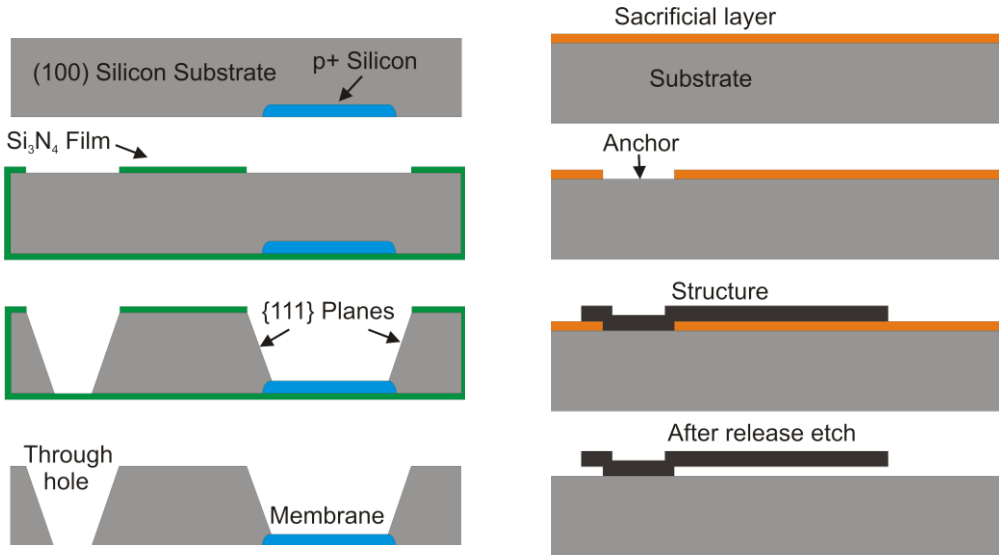

Figure 1.5: Bulk (left) and surface (right) micromachining sequences

Under bulk micromachining one understands processes where the body of the substrate undergoes certain changes e.g. is being dry or wet etched, while surface micromachining means bringing and structuring a sequence of thin films (usually ~1 µm) on the surface of a substrate.

In a nutshell, a standard MEMS fabrication process can be subdivided into the following steps:

1. substrate production
2. thin film deposition
3. photolithography
4. surface modification
5. etching
6. packaging

Step 1 refers to a fabrication of a substrate, on which the following processes will be carried out. Steps from 2 to 5 usually repeat themselves several times in the whole fabrication process in different combinations and sequences. Step 6 implies a block of final operations, to prepare the fabricated system for characterization, delivery and utilization. In this work, thin film deposition (electroplating, sputtering, CVD), photolithography, etching and surface micromachining play the main role.

It is worth noting that although many microfabrication techniques came to MEMS production from IC industry, there are a lot of other processes and materials that have been developed exclusively for MEMS microfabrication. Table 1.1 represents this differentiation.

Table 1.1 IC and MEMS Processes and materials

	Conventional IC	**MEMS**
Processes	- photolithography, - thermal oxidation, - ion implantation, - LPCVD, - PECVD, - evaporation, - sputtering, - wet etching, - plasma etching, - RIE, - ion milling	- anisotropic wet etching of single-crystal silicon, - DRIE, - x-ray lithography, electroplating, - low-stress LPCVD films, - thick-film resist (SU-8), - spray-coating, - micromolding, - batch microassembly
Materials	silicon, silicon dioxide, silicon nitride, aluminum	Piezoelectric films (PZT), magnetic films (Ni, Fe, Co), high temperature materials and ceramics, aluminum alloys, stainless steel, Pt, Au, sheet glass, PVC, PDMS

The main processes used in fabrication of a curved beam electrostatic microactuator will be described in detail in chapter 3 of this work.

1.3 Overview of Microactuators

This section is dedicated to the definition and classification of microactuators followed by discussion of several examples that have been developed in last decades focused on the technological fabrication processes and valve performance. Finally, technical specifications for an electrostatically-actuated microvalve developed in this work will be introduced and a brief description of the microvalve will be given.

1.3.1 Definition and classification

Microactuators have been in development since 1960s. The first examples would be an electrostatic resonant-gate transistor, developed by Nathanson at RCA and a miniature electromechanical resonator inside “Accutron” watch by “Bulova” Corp. [10], [11].

An actuator in general is a mechanical device for moving or controlling (i.e. actuating) a mechanism or system in response to a control signal [12]. In other words, an actuator is an energy transducer that transforms energy from one form into another (Fig 1.6).

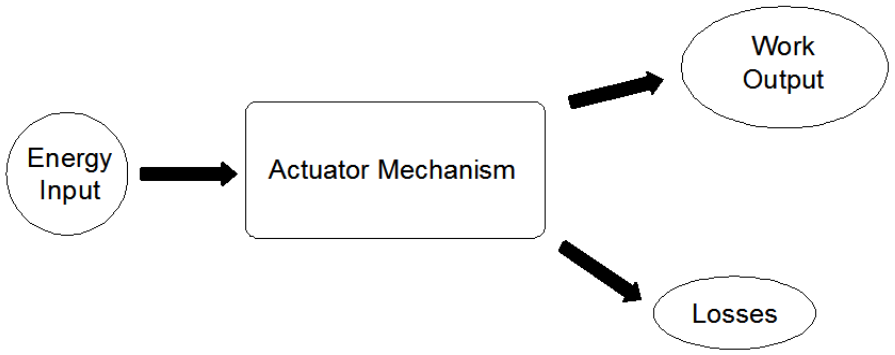

Figure 1.6: Schematic of an actuator function.

The energy input which is typically electric or thermal causes changes in a mechanical state of an actuator mechanism. This in turn results into useful work output (motion). A part of energy is always lost into e.g. heat. Microactuator in turn performs the same task but on a micro level and has dimensions typical for microsystems.

Since first developments, the principles and applications of microactuators have significantly expanded. According to different sources [11], [12], the methods of actuation can be divided into following categories:

- electrical
- magnetic
- thermal/phase
- optical
- mechanical/acoustic
- chemical-biological

Each mechanism has its benefits, drawbacks and applications. For instance, shape memory devices possess very high power density, but on the other hand their efficiency and speed are relatively low. Electrostatic microactuators in turn are very efficient and fast, but their integration into typical on-chip circuits is complicated by their high driving voltages. The following subsections will give a closer look to the principals and applications of different microactuators.

1.3.2 Electromagnetic actuators

Basically, there are several types of electromagnetic actuators. First, the actuators based on the magnetostrictive effect, when ferromagnetic bodies change their dimensions in presence of magnetic field [13]. The relative change in length $\Delta l/l$ is called magnetostriction. The effect is independent of the direction of the magnetic field and is governed by the following expression

$$\frac{\Delta l}{l} = \varepsilon = cB^2 \tag{1.1}$$

where

ε – static strain produced by flux density B
c – material constant, [m^4Wb^{-2}]

This effect is widely used in the design of ultrasonic devices, e.g. medical surgery instruments. In MEMS, magnetostrictive films deposited by sputtering present a good actuation option in case when contactless, high-frequency operation is needed, e.g. in noncontact torque sensing [14].

Another approach utilizes Lorentz force that acts on a current-carrying conductor in a magnetic field making it move [15]. The Lorentz force law defines this force as

$$\overline{F} = q[\overline{v} \times \overline{B}] \tag{1.2}$$

where

q – electrical charge of the particle
v – velocity of the particle
B – magnetic field

Magnetic actuation is favorable for its ability to generate relatively large forces and deflections with low driving voltages. The drawback here is that scaling in the micro-domain is limited due to the fact that electromagnetic force is directly proportional to the characteristic dimension as $F \sim D^3$. That means that a size reduction of 10 causes a magnetic force reduction of 10000.

Finally, there are actuators directly using magnetic attraction forces of permanent magnets. In this case, scaling results appear to be one order of magnitude better [14].

It is obvious that presence of magnetic field is mandatory for all types of electromagnetic actuators. Thus, utilization of magnetic materials is needed. The vast majority of the magnetic actuators developed so far utilize soft magnetic materials like $Ni_{0.8}Fe_{0.2}$, which can be relatively easy deposited by electroplating. Unfortunately, hard magnetic materials cannot be deposited using standard MEMS technological solutions. However, they are still desirable in electromagnetic microactuators because of good scaling properties and potential for larger forces and deflections [16].

1.3.3 Electrostatic actuators

Electrostatic actuation has long been one of the most favorable choices in many MEMS applications such as microvalves, tunable RF capacitors, microswitches or micromotors due to its good scalability, low current consumption and relatively simple producibility. The reason for it is the fact that electrostatic force F_{el} between two charged conductors increases as the distance d between them decreases

$$F_{el,z} = -\frac{\varepsilon_r \varepsilon_0 w L U^2}{2d^2} \tag{1.3}$$

where

ε_r – relative permittivity
ε_0 – permttivity of vacuum
w – conductors width
L – conductors length
U – applied voltage

An example of such a design can be a vertically driven resonant microstructure.

On the other hand, the movement of charged plates can be realized parallel relative to each other. In this case,

$$F_{el,x} = \frac{\varepsilon_r \varepsilon_0 w U^2}{2d} \text{ and } F_{el,y} = \frac{\varepsilon_r \varepsilon_0 L U^2}{2d} \tag{1.4}$$

This approach allows larger displacements. Comb-drive actuators and rotary driven electrostatic micromotors are the most obvious examples here.

Electrostatic actuation is a solution in cases of low force and energy densities. However, small displacement requirement can turn from advantage into a disadvantage because it is a limiting factor in some applications. For example, in microvalves, flow rates will be limited by smaller gaps. Significant pressures cannot be withstood either. Further, the applied voltages are limited by disruptive strength of the isolation layers. Electrostatic actuators are also very sensitive to particles that can impede the motion of the moving parts. Moreover, these particles can lead to sparkovers.

In this work, alternative curved-beam design is presented. It implements one stationary flat electrode and a movable electrode in a shape of a curved cantilever beam. Due to this layout, better balance between force and displacement can be achieved[1].

1.3.4 Piezoelectric actuators

Piezoelectric (PZT) actuators utilize the effect of a mechanical stress appearance in certain crystals under an applied electrical field. In a simplified way, the effect can be described by noting the anions and cations moving in opposite directions under the influence of an electric field. This leads to forces generation which in turn causes lattice deformation in noncentrosymmetric crystals due to the presence of both high and low-stiffness ionic bonds [14].

Going deeper in the theory of piezoelectricity would require an understanding of the piezoelectric equations describing the coupling between mechanical and electrical strains in a piezoelectric material.

If a stress σ is applied to a piece of piezoelectric material (e.g. quartz) the resulting one-dimensional strain ε will obey the Hooke's law

[1] More detailed description of the theoretical principles is given in Chapter 2 of this work

$$\varepsilon = S\sigma \tag{1.5}$$

where $S = E^{-1}$ is the compliance, and E is Young's modulus.

Further on, if a potential difference is applied across the faces of the material, an electric field E appears and one can write

$$D = \varepsilon_0 E = P \tag{1.6}$$

where

D – electric displacement (electric flux density)
ε_0 – permittivity of vacuum
P – polarization (electric dipole moment per unit of material)

Equation 1.5 contains only mechanical parameters while equation 1.6 only electrical ones. These equations can be combined into equations both for direct and inverse piezoelectric effects. In case of actuation, only the latter is of interest

$$\varepsilon = dE + S^E\sigma \tag{1.7}$$
$$\varepsilon = gD + S^D\sigma \tag{1.8}$$

where

d and g – piezoelectric constants in mV^{-1} and mC^{-1} respectively
S^E – the compliance at constant field
S^D – the compliance at constant electric flux density

Solving equations 1.7 and 1.8 for σ gives

$$\sigma = -eE + E_{(Y)}{}^E\varepsilon \tag{1.9}$$
$$\sigma = -hD + E_{(Y)}{}^D\varepsilon \tag{1.10}$$

where

$e = d/S^E$ and $h = g/S^D$ – piezoelectric constants
$E_{(Y)}{}^E$ – the Young's modulus under constant electric field
$E_{(Y)}{}^D$ – the Young's modulus under constant electric flux density

Another important parameter is the electromechanical coupling coefficient k, which is a measure of the interchange of electrical and mechanical energy

$$k = \sqrt{ge} \tag{1.11}$$

Large forces (up to several MPa) can be generated using PZT actuation. Among the other advantages based on the example of PZT micromotor and summarized in [14] are high energy densities and low driving voltages.

However, generated displacements are relatively small. The latter can be overcome by utilizing bi-morph film or stack design (Fig. 1.11c). Another disadvantage is limited miniaturization opportunity due to the falling-off of the piezoelectric effect with the bulk of the material [14].

1.3.5 Thermal actuators

Thermal actuation occurs due to the property of materials to expand or contract as they undergo temperature changes. These approaches are considerably useful when large forces accompanied by large strokes are needed. Thermally actuated microsystems often possess relatively simple design. However, they demonstrate slow response times, high power consumption and sensibility to the ambient temperature conditions [10].

From physical point of view, heat transmission is described by Fourier's law, Newton's law of cooling, and the Stefan-Boltzmann radiation law.

Fourier's law describes heat transport in solids through conduction. Consider a rectangular slab (Fig. 1.7) of material held between two parallel plates of area A at temperatures T_1 and T_2. Then, the total amount of heat Q flowing through a slab is

$$Q = -\kappa \frac{A(T_1 - T_2)}{d} t \tag{1.12}$$

where

κ – bulk heat conductivity, [$Wm^{-1}K^{-1}$]
d – plate separation
t – time

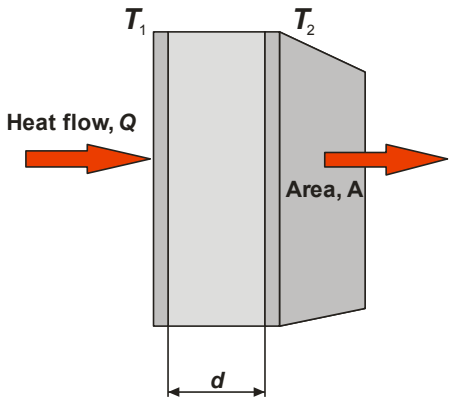

Figure 1.7: Heat conduction in a solid between two plates at different temperatures.

Consequently, heat conduction or heat flux, q, is the heat flow per unit area and time, meaning

$$q = \frac{Q}{At} = -\frac{\kappa}{d}(T_1 - T_2) \tag{1.13}$$

or in more general form known as Fourier's law of heat conduction

$$q(r,t) = -\kappa \nabla T(r,t) \tag{1.14}$$

where

r(x,y,z) – position vector in the heat conductor
∇T – temperature gradient

Newton's law of cooling is a discrete analog of the Fourier's law and describes heat transfer in fluids through convection

$$q = hA(T_1 - T_2) \tag{1.15}$$

where

h – constant convective heat transfer coefficient, [$Wm^{-2}K^{-1}$]
A – surface area of the heat being transferred

It is worth noting that term "constant" with respect to heat transfer coefficient means that this coefficient is temperature or rather temperature difference independent. This is the only case when Newton's law of cooling in this form is applicable to the description of convection heat transfer.

As it has already been mentioned above, the radiation mode of heat transfer is governed by the fundamental Stefan-Boltzmann law

$$q = \sigma A T^4 \tag{1.16}$$

where

T – absolute temperature
A – surface area

The constant of proportionality σ = 5,670400×10^{-8} $Js^{-1}m^{-2}K^{-4}$ called the Stefan-Boltzmann constant. It derives from other known constants of nature.

As can be seen from Eq. 1.16, radiant heat transfer is proportional to the fourth power of the absolute temperature, whereas in cases of conduction and convection it was linearly proportional to temperature differences.

Equation 1.16 describes the radiation from the ideal emitter, or blackbody. In real situation, bodies emit less energy and their thermal emission can be described by

$$q = \varepsilon \sigma A T^4 \tag{1.17}$$

where ε is the emissivity of the surface ranging from 0 to 1.

Thermal actuators can be realized as bimorph (e.g. bimetallic), thermopneumatic or shape memory alloy based devices. A brief insight to each of the approaches is given in the following subsections.

1.3.5.1 Bimorph actuators

Bimorph actuation scheme is one of the basic and widely used approaches. The principle is in the utilization of two materials[2] with distinct thermal expansion coefficients α_L (CTE). The materials must be bonded together. Hence, the structure is usually a sandwiched strip or membrane as schematically illustrated in Fig. 1.8 [1].

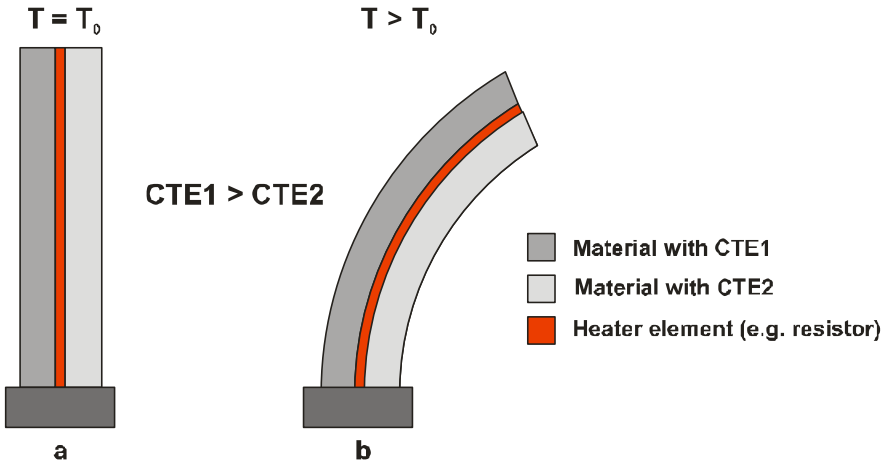

Figure 1.8: Schematic representation of a bimorph actuation principle.

As temperature changes from the initial state, a bimorph cantilever or membrane will bend due to incompatible CTEs. The structure will return to its initial state once the applied heat is removed.

One of the basic advantages of bimorph actuators is their nearly linear deflection vs. applied power behavior. Unfortunately, these devices require high power for operation and have low

[2] Very often, metals are used as the materials for bimorph actuators. Thus, term “bimetal” and “bimetallic” can be met in literature.

bandwidth determined mainly by thermal time constants [17]. However, they remain a popular choice for many MEMS application, such as microvalves and micropumps.

1.3.5.2 Thermopneumatic actuators

Thermopneumatic actuators are relatively popular in MEMS due to their ability to deliver large forces through long strokes [15]. Constructively, they consist of a sealed cavity filled with fluid media. The media expands and evaporates upon heating thus, raising the pressure inside the cavity. This, in turn, makes one of the cavity walls used as flexible element bulge outward. Schematic representation of this principle is shown in Figure 1.11e.

1.3.5.3 Shape memory alloy actuators

Some metal alloys (e.g. NiTi, NiTiPd), after plastic deformation, return to their original shape after being heated. This effect is called "thermal shape memory" or simply "shape memory" and occurs due to a crystalline phase change known as "thermoelastic martensitic transformation" [49] when a temperature-dependent phase transition between martensite and austensite phases of the alloy takes place. The metal alloys having this capability are called shape memory alloys (SMA). Large forces are achievable here, which makes this phenomenon a good choice for actuation. But acting speeds are much lower than in case of electrostatic or piezoelectric devices. Another possible demerit of SMA actuators is the need of mechanical biasing structures such as springs to generate a return force, enabling cyclical behavior.

1.3.6 Optical actuators

Optical actuation means transformation of the photonic energy of incident light into mechanical motion. This can be achieved by using photovoltaic effect to generate first voltage and/or electrical current that will in turn power a mechanical part of such a system, e.g. motor, piezoelectric or any other electrically driven actuator. However, such a design seems to be neither sufficiently small nor effective. Fortunately, another solution exists. In the heart of it, there are materials which exhibit the so called "photostriction effect". Photostriction is the generation of strain by irradiation of light. In a nutshell, this effect is a superposition of the photovoltaic and the piezoelectric effects. Working schema will look very similar to what is depicted in Figure 1.7 for a bimorph actuator. Only heating must be replaced with incident light.

Photostriction is rare. It can be met in certain ceramic materials. The most widely if not the only one used material at the moment[3] is lanthanum-modified lead zirconate titanate PLZT [18]. PLZT is an artificial ceramics made of Lead, Lanthanum, Zirconium and Titanium. Among the other ceramics being investigated are PMN-PT doped with Tungsten and PZN-PT.

Until not, not very many research has been carried out on this very promising field. However, several applications such as photo-driven relay, microwalking device have already been demonstrated [19].

[3] To the authors best knowledge.

1.3.7 Biological actuators

Apart of those created by humans, there are microactuators created by nature itself. In fact, they belong to the most versatile and efficient at all. Although they have limited lifetime and require sometimes very specific environmental conditions, they offer a great diversity of functions, low cost, self-assembly and nanoscale size to name a few.

There are three main types of biological actuators [17]:

- cytoskeleton/microtubules
- cilia/flagella
- muscle

Cytoskeleton is a framework of the cell. It is present in all cells and is very dynamic. Its main function is to adapt the shape of a cell to the external conditions, provide movements of the whole cell, intra and intercellular transport, cellular division etc. Microtubules in turn are one of the active matter components of the cytoskeleton. They have a diameter of 25 nm and serve as structural cell components and are involved in many processes within the cell including e.g. mitosis, cytokinesis and others. Microtubules are self-assembled polymers of α- and β-tubulin. Many intracellular components are transported within cells not by diffusion but by movement along microtubules.

Cilia and flagella are thin cylindrical structures found in most microorganisms and animals, but not in higher plants. Their function is to move (propel) cells or to transport substances relative to them, for example, moving mucus along the respiratory passages, or making spermatozoids move in the direction . Flagella are typically longer than cilia and their movement is generated in a different way. However, their structures are very identical. They consist of a bundle of microtubules surrounded by an extension of the cell's membrane. Motion of cilia and flagella is created by the microtubules sliding past one another. This requires motor molecules of dynein, which link adjacent microtubules together, and the energy of adenosine triphosphate (ATP). Dynein powers the sliding of the microtubules against one another — first on one side, then on the other.

Muscle is a contractive tissue of higher animals, where specialized cells group together to generate force and motion. Muscles are classified as skeletal, smooth and cardiac ones. Skeletal muscles can be well voluntary controlled, whereas cardiac and smooth muscle contraction occurs without conscious thought. Muscle cells contain contractive filaments that move past each other and change the size of the cell. ATP is used for "fuel". The two key molecules involved in the muscle actuation process are actin and myosin. Myosin generates traction along fixed actin filaments using its head. Moreover, many myosin molecules can form bands that fit in between actin filaments. The contraction of muscle is controlled by the release of Ca^{+} ions into the muscle fibers.

Up to now it is still too early to speak of the applications of biological actuators in micromachining. Still, they can potentially bridge the gap between micron-scale and nanoscale structures, and their unique properties such as self-assembly can also bring the technology to a new level of reliability and reproducibility.

1.3.8 Applications of microactuators. Future trends.

While laboratory developments of almost all of the above mentioned types of microactuators have been successfully demonstrated, their broad commercialization has been more difficult [9]. Nevertheless, there are examples of successful commercial introduction of microactuators, such as piezoelectric microactuators used in ink-jet printer heads [20]. In biomedicine, SMA and PZT microactuators are used as micromanipulators or microgrippers (Fig. 1.9) and microscalpels [21].

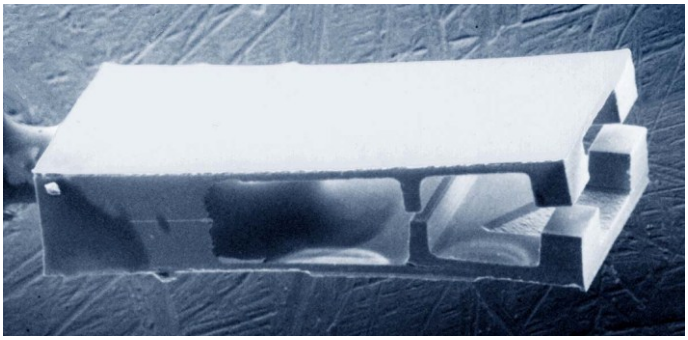

Figure 1.9: Surgical SMA microgripper [21]

There is a growing interest in introduction of chemical microactuators in such spectacular fields as microturbomachinery and microcombustion engines for aero-space applications [9]. Other promising applications of microactuators include micromotors, controllers of micromirrors and other optical elements, micropumps and microvalves. These complex devices in turn can be used in biomedicine, automotive aerospace and other fields of application.

In the nearest future it is likely to expect more interest and research in the fields of so called "smart" actuators, i.e. those that are based on smart materials and structures that capable to return both sensing and actuating functions (e.g. piezoelectric and converse piezoelectric effects) [19]. A lot of work towards development of biomechanical microactuators is also being carried out.

A detailed review of each microactuators application field lies beyond the scope of this work. However, it is still necessary and interesting to take a deeper look into at least one of them. This will give an understanding of practical microactuators utilization, current developments and trends. In the following subsections, applications of microactuators in microvalves are described.

1.4 Microvalves: basic information

Over the last decades, microfluidic systems and microvalves in particular have become indispensable in automotive, aerospace, healthcare and many other applications. However, in spite of great number of research and development in this field, microfluidic components are still far from wide commercialization [7]. High flow rates, switching speeds, operation stability and low costs are the basic requirements to be met during the design and manufacturing of microvalves and their components. These requirements are hard to be met all at once. Thus, further research in this direction appears to be important in order to find the most efficient technical solutions.

A microvalve can be defined as is a MEMS device that controls the flow of a fluid (gas, liquid) by changing its volume, speed or direction. Typically, this function is implemented with the help of a movable element (membrane, beam, or ball) that opens or closes a channel through which a fluid flows. However, there are other principles of microvalve operation, such as for example, rheological one, that does not necessarily include a mechanical component.

There are two main classes of microvalves: active and passive. Both classes include mechanical and non-mechanical actuation principles. Passive microvalves do not require power for actuation. The vast majority of them are so-called mechanical check valves. Check valves are designed in such a manner that they only allow a fluid to flow in one direction and block it in the opposite one. An example of a check valve design is represented in Fig. 1.10.

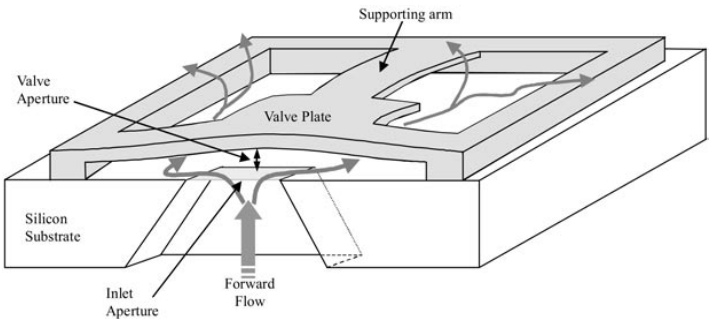

Figure 1.10: Check valve concept [22]

Non-mechanical passive microvalves include different capillary mechanisms. These devices as well as non-mechanical active microvalves are beyond the scope of this work and will not be discussed here. Detailed classification and overview of such systems is given in [7]. Further, only examples of active mechanical microvalves will be presented since they are closely related to the topic of this dissertation. Figure 1.11 schematically illustrates the basic actuation principles of such microvalves.

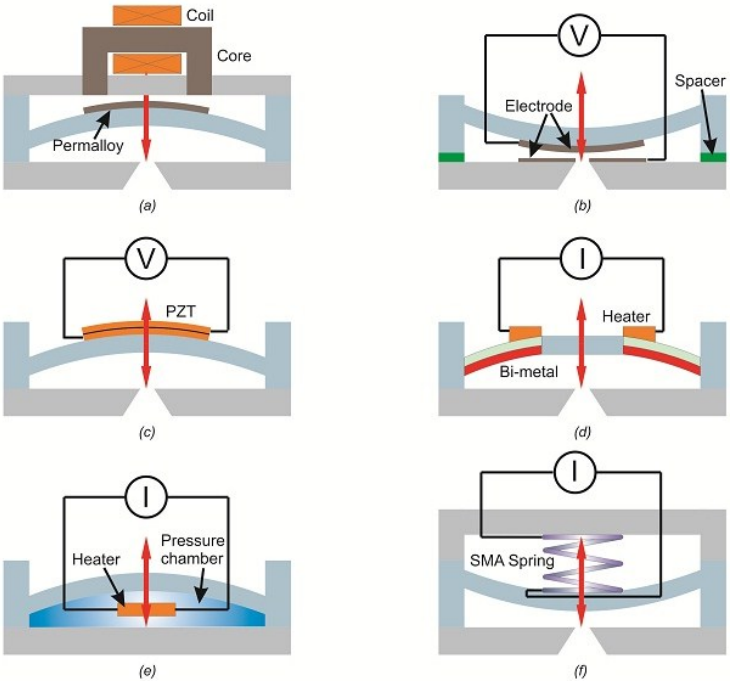

Figure 1.11: Actuation principles of active mechanical microvalves: (a) electromagnetic; (b) electrostatic; (c) piezoelectric; (d) bimetallic; (e) thermopneumatic and (f) shape-memory alloy actuation [7]

Active mechanical microvalves can be further classified by their operational mode as normally-open and normally closed. The former one lets the fluid flow pass through the valve when no power is applied to it, whereas the latter on the contrary blocks the flow under the same condition.

1.4.1 Electromagnetic microvalves

Possibly the first ever produced microvalve was an injection valve in a gas chromatographic analyzer introduced by Terry *et al.*. in 1979 [23]. In this device, an electromagnetic actuation principle was realized with a solenoid plunger (Fig. 1.12).

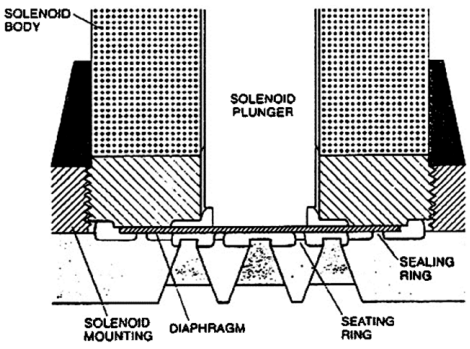

Figure 1.12: The microvalve with a solenoid plunger by Terry et al. [23]

The valve was fabricated on a 2-inch silicon wafer. Anisotropic KOH silicon etching techniques were used in order to form the through holes, the valve cylinder and the seating rings. Solenoid was fabricated separately and then connected to the valve body by threading.

Since then, multiple different electromagnetically actuated microvalves using external magnetic fields have been reported [7]. One of the biggest technological disadvantages of this method is relative complexity of assembles. Magnets or solenoids must be somehow connected to the device after fabrication. This makes batch production difficult if not impossible and also complicates miniaturization. There are however integrated magnetic inductors fabricated using MEMS-based technology [7]. Figure 1.13 demonstrates such assemble realized utilizing a low-temperature biochemically compatible polymer bonding process [24]. This assemble consists of three main parts: glass motherboard, structured with bulk micromachining etching techniques, glass spacer substrate with etched through-holes, and a silicon-based active microvalve element with silicon membrane, also structured by etching.

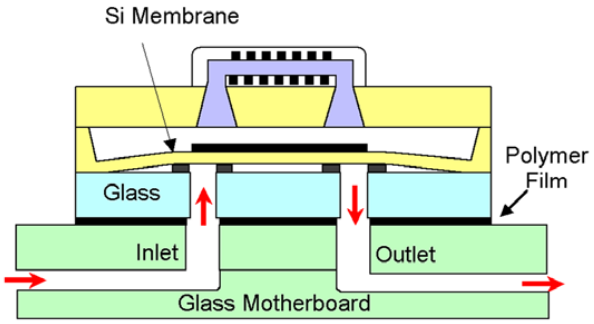

Figure 1.13: Magnetic microvalve with an integrated magnetic inductor by Oh et al. [24]

Large strokes are among the benefits of this approach, both with external or integrated inductors [25]. Flow rates up to 1300 ml/min at operating current of 1A and differential pressures of more than 200 kPa were achieved by Oh et al. [24]. Moderate response time from 3 ms to 10 ms is usually demonstrated by electromagnetic microvalves [26].

1.4.2 Electrostatic microvalves

Electrostatically actuated microvalves have been in active development since 1990 when such design was introduced by Ohnstein et al. [27]. Such devices have been basically used in pneumatic applications. They possess high efficiency, offer high switching speeds and have little dependence on the ambient temperature. However, due to the nature of the electrostatic force their driving voltages must be relatively high (up to more than 350 V) in order to withstand high differential pressures. If high voltages are not achievable, electrostatic valves demonstrate moderate performance in terms of pressure range and flow rates. Very often, silicon etching techniques accompanied by metal deposition techniques are used in fabrication of electrostatic valves. For example, relative majority of electrostatic microvalve designs use membranes of different shape and material as an active element. Yang et al. [28] reported an electrostatically driven microvalve with measured flow rate of 45 ml/min at room temperature with operating voltage of 136 V. A silicon membrane was used as its active element. The valve has a comparatively complicated design (Fig. 1.14).

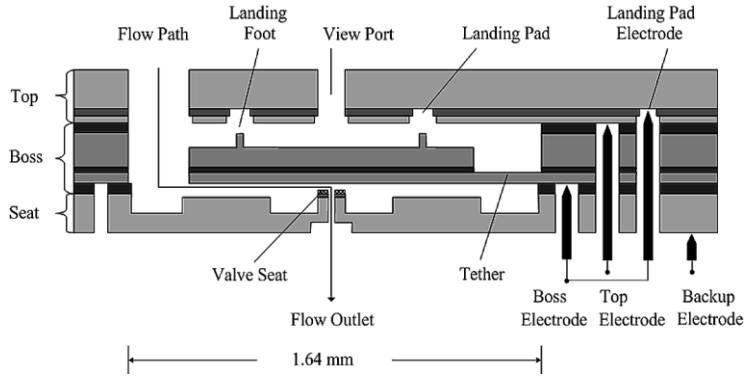

Figure 1.14: Electrostatic fuel valve [28]

Fabrication included direct bonding of multiple silicon-on-insulator (SOI) wafers, deep-reactive ion etch (DRIE) as well as different thin-film deposition and structuring techniques.

However, not only membranes but also cantilever beams (like in this dissertation) and S-shape stripes (Fig. 1.15) have been used as movable open/close-elements. In the latter case, an S-shape Fe-Ni alloy stripe moves back and forth as voltage is alternately applied between each of the electrodes and the film.

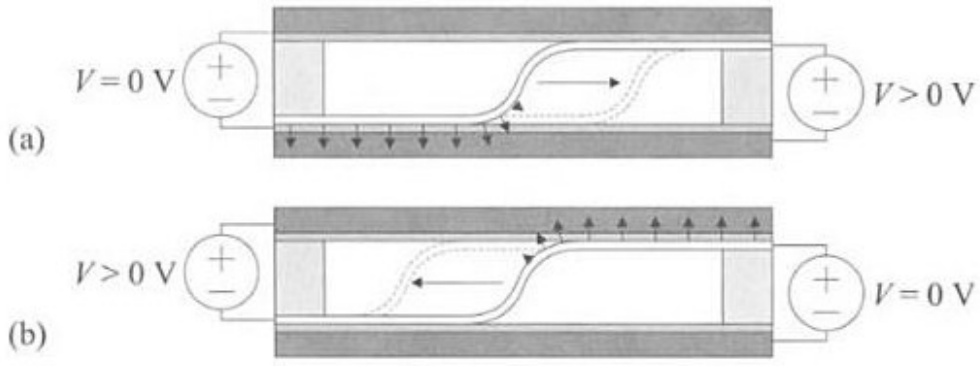

Figure 1.15: A concept of microvalve with an S-shaped electrostatic microactuator

(a) pulled down to the bottom electrode

(b) pulled up to the upper electrode [9]

The fabrication process included thermal oxidation of both silicon wafers, KOH etching of the inlet and outlet ports, the spacing material was a 2 mm thick silicon rubber resin. Prefabricated Fe-Ni alloy stripe was clamped between Si wafers and silicon resin.

1.4.3 Piezoelectric microvalves

Piezoelectric (PZT) microvalves are widely used when large bending forces and small displacements are needed. Although large strokes, which are hard to achieve with piezoelectric actuation, are normally desirable in microvalves, there are already several commercially

available designs of such systems [7]. The inability to perform large displacements has been successfully overcome by different design approaches, e.g. stacked piezoelectric disks, or hydraulic amplification [7]. However, high voltages are usually needed to activate such a device. A microvalve operated at 500 V with maximal flow rate of 12 ml/min was reported by Roberts et al. in 2003 [29]. Rogge et al. [30] developed a normally closed microvalve with a 25-fold hydraulic amplification achieving a valve stroke of 50 μm at driving voltages of up to 300 V with a response time of 2 ms. Maximal flow rate of 70 ml/min was achieved by Shao et al. [31]. One of the concepts of a piezoelectric microvalve with stacked PZT is shown on Fig. 1.16.

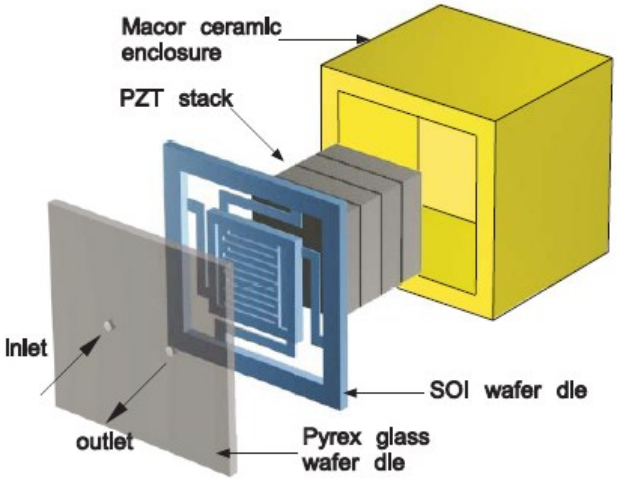

Figure 1.16: A concept of a piezoelectrically actuated microvalve with stacked PZT [26]

This valve was fabricated using two wafers: an SOI wafer with the device layer and a Pyrex glass wafer with inlet and outlet ports created with an electrochemical discharge machining process. SOI wafer was etched using DRIE techniques whereas glass wafer was wet etched. Finally, both wafers were bonded together by the anodic bonding.

Another example of a piezoelectrically actuated microvalve with thin film PZT was demonstrated on Fig 1.11 (c).

1.4.4 Thermally actuated microvalves

Thermally actuated microvalves utilize bimetallic, thermopneumatic and shape memory alloy actuation principles.

1.4.4.1 Bimetallic microvalves

Bimetallic microvalves usually have a thin-film bi-layer of metals serving as heater-elements deposited on the membrane. When heated (i.e. by electric current), these elements deform due to the difference in thermal expansion coefficients, thereby deforming the membrane. Jerman [32] reported a bimetallic microvalve with Al/Si membrane (Fig. 1.17) and measured flow rate of 150 ml/min at differential pressure of 350 kPa. A leakage flow rate of N_2 gas was about 30 µl/min at

pressure of 34.5 kPa. An anisotropic silicon etch was used to produce the diaphragm. The backside corner compensation provided an octagonal approximation to its outer diameter, while the inner one achieved almost circular shape. Aluminum was used as a metallization.

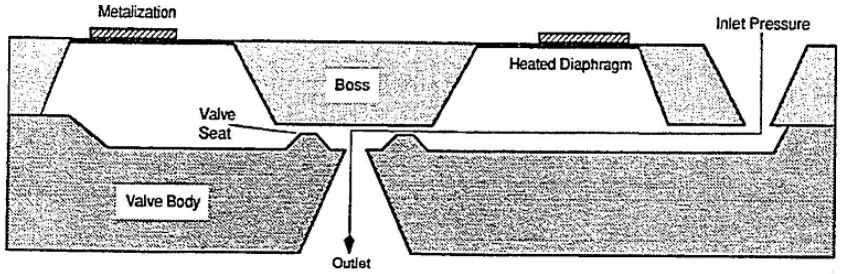

Figure 1.17: Cross section of a bimetallically actuated diaphragm microvalve [32]

Another bimetallic microvalve was reported by Barth [33] with 30 μm thick Ni film deposited on a Si membrane and demonstrated a flow rate of more than 1000 ml/min opening against pressure of 1035 kPa. Power consumption of this valve was 1.02 W in 0.2 s.

1.4.4.2 Thermopneumatic microvalves

In thermopneumatic microvalves, large forces and large strokes are achievable, but slow operating speed and difficulty of manufacturing due to the necessity of a sealed cavity for a fluid are among the main disadvantages[4].

There have been relatively many publications dedicated to the research and development of thermopneumatic microvalves. The microvalve developed by Zdeblick [34] is considered to be the first ever developed thermopneumatic microvalve. The device has a flow rate of 2l/min and is capable to open against pressures of 690 kPa at 2 W of applied power. Takao *et al.* [35] designed a valve with a PDMS membrane for large stroke and high sealing performance. PDMS material provided an adhesion between glass and silicon in the structure. At 30 kPa, leakage was about 1μl/min. Rich and Wise [36] presented a microvalve with polysilicon heater grids above the cavity floor. The cavity was partly filled with pentane to increase thermal efficiency and sealed with a volatile fluid below a corrugated membrane. Flow rate of the valve was about 400 ml/min at differential pressure of 11.3 Pa. Figure 1.18 shows a normally open thermopneumatic microvalve designed by Yang *et al.* [37] using a composite membrane and 3M Fluorinert fluids. Flow rate of N_2 gas was about 1 l/min at 228 kPa with power consumption of less than 40 mW. The membrane deflection was about 134 μm at 28.3 kPa.

[4] To the authors opinion, the term "thermopneumatic" is not precise since apart from gases, liquids such as deionized water have also been used in such designs. In the latter case, term "thermohydraulic" would be more appropriate.

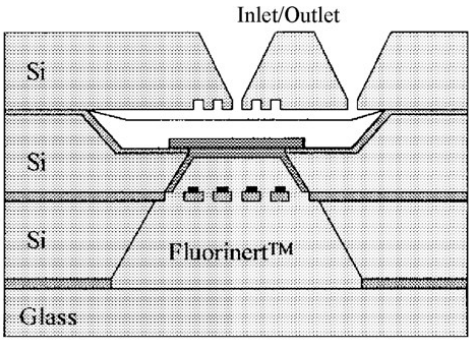

Figure 1.18: The thermopneumatic microvalve with composite silicone rubber/Parylene membrane by Yang et al. [37]

1.4.4.3 Shape memory effect microvalves

Utilizing shape memory effect, microvalves can introduce high output forces enough to withstand high differential pressures and flows [7]. Shape memory effect also allows compact and simple structures. Among the disadvantages of the method are low efficiency and low operational bandwidth (typically 1 -5 Hz), though operational frequencies up to 30 Hz have been reported [7], [38].

An example and working principle of a normally closed SMA actuated microvalve is demonstrated on Figure 1.19. An external metal spring keeps the valve closed when no heating is applied to the SMA [33]. Once heated, the deformed SMA returns to its original shape thus lifting the bossed valve membrane against the spring and opening the valve.

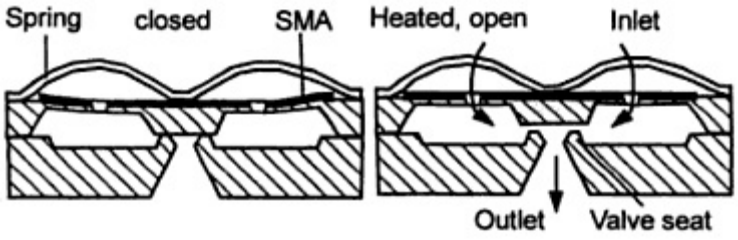

Figure 1.19: A normally closed SMA microvalve with external metal spring [33]

Kohl et al. presented different gas microvalves with SMA thin film [39]. NiTi, NiTiCu and NiTiPd SMA were used for the actuation (Fig 1.20).

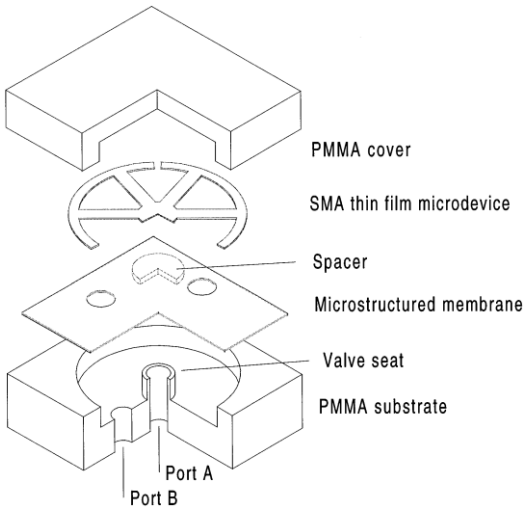

Figure 1.20: Schematic cross-section of a thin film SMA microvalve [39]

A pressure chamber with inlet and outlet ports A and B was realized by mechanical micromachining of a PMMA substrate. A polyimide membrane with lithographically structured holes was integrated onto the pressure chamber by membrane transfer for a silicon substrate. The SMA microdevice was interconnected to the cover by adhesive bonding. Flow rates of 360 ml/min at differential pressures below 260 kPa were achieved with stroke of about 20 μm at power between 110 mW and 220 mW.

A miniaturized normally closed pinch-type microvalve was reported by Pemble and Towe [40]. It employed wires of NiTi SMA to control flows in Si tubing. A maximum flow rate of 16.8 ml/min at a differential pressure of 20.7 kPa with a power consumption of 298 mW was permitted.

1.4.5 Microvalves on alternative principles

This brief overview of microvalves would not be complete without mentioning of several different approaches to the realization of microvalves. Among them one can outline bistable devices and microvalves utilizing different combinations of principles discussed above.

A common drawback of all the previously discussed typical active microvalves is that continuous power must be applied in order to keep the device open in normally closed mode or closed in normally open one. Bistable microvalves solve this problem since they only require power to switch between two stable positions.

An interesting design that illustrates this approach was proposed by Fazal et al. [41]. A miniature stepper motor mounted on a spring and a screw connected to its rotor to deflect the membrane of the microvalve were used by this group (Fig. 1.21).

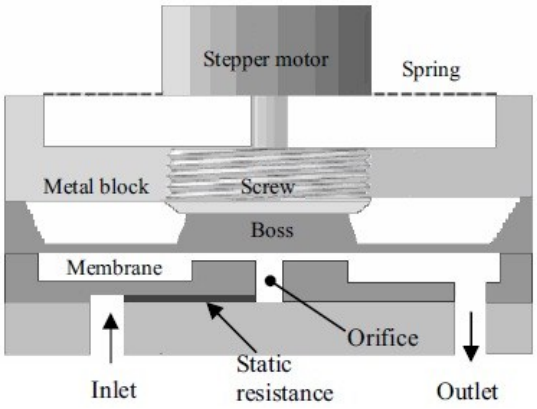

Figure 1.21: A stepper-motor actuated microvalve [41]

This approach allows withstanding high pressures and does not require any power to maintain any intermediate state of the system. Moreover, there is no interaction between a working fluid and the actuation mechanism. The construction consists of two silicon wafers and one Pyrex wafer bonded together. Standard micromachining techniques, such as KOH and DRIE etching were used. Air flow rates of 220 ml/min at a pressure difference of 400 kPa were reported.

Another realization of a bistable microvalve using thermal buckling was presented by Goll et al. [42]. Buckling of the polysilicon membrane with a compressive stress was introduced by thermal treatment and mechanical loading. The closed microvalve could withstand inlet gas pressure up to 47 kPa. Bohm et al. [43] reported a bistable electromagnetic microvalve using a NeFeB permanent magnet, a 800-turn solenoid coil and a spring biased armature to achieve bistable actuation with a stroke of 200 μm (Fig. 1.22).

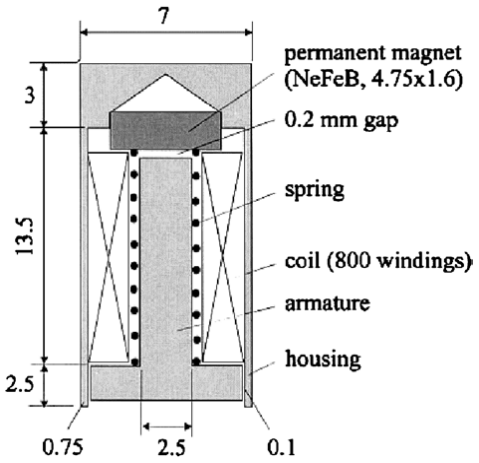

Figure 1.22: The bistable electromagnetic microvalve with an integrated magnet [43]

The application of the positive current to the coil reduced the holding force of the armature with the magnet and hence the spring could push the armature downward to close the valve. A negative current pulse would then open the valve again.

The valve consists of a micromachined and conventionally machined bi-stable electromagnetic actuator parts connected together in one assemble. The silicon valve part is a "sandwich" construction of two silicon wafers etched in KOH. There is also a layer of chemical resistant silicon rubber bonded in between to provide the flexibility needed to move the valve boss, as well as for improved sealing.

Additionally, combinations of the actuation mechanisms e.g. pneumatic-electrostatic or electromagnetic-electrostatic are used to design bistable microvalves. A design proposed by Bosch et al. [44] utilized the latter combination in a microvalve for gas flow regulation. It incorporated a membrane part with an integrated planar coil, which was bonded to another part defined as electrode. A membrane part was additionally placed between permanent magnets.

Flow rates up to 3 ml/min at a static gas pressure of 16 kPa were achieved. Table 1.2 summarizes the merits and drawbacks of different microvalve concepts.

Table 1.2: Comparison of basic microvalve principles and their properties

Method	Size	Efficiency	Pressure range	Flow rate	Speed	Temperature range	Price
Electromagnetic	medium	high	high	high	medium	high	medium
Electrostatic	small	high	medium	medium	high	high	low
Piezoelectric	medium	high	high	medium	high	medium	medium
Bimetallic	small	high	high	high	medium	low	low
Thermopneumatic	medium	low	high	high	low	low	medium
SMA	small	low	high	high	low	low	medium

1.4.6 Microvalves applications

Since microvalves belong to a broad MEMS family, they applications often intersect with those of other MEMS systems. The most promising application fields for microvalves are

- biomedical
- chemical analysis
- aerospace
- automotive
- environmental monitoring

In short, microvalves can be used everywhere where precise micromechanical control of small amounts of fluids is required. Further advantages include fast response time, low power consumption, small dead volume, improved fatigue properties and of cause small size and low cost due to batch production possibility. In the following subsections several examples and proposals of such applications will be given.

1.4.6.1 Microvalves in biomedical and chemical analysis systems

There are a lot of expectations in medical and biomedical markets concerning MEMS solutions in a wide variety of applications among which the most typical ones are:

- hearing aids
- Lab-On-a-Chip (LOC)
- blood pressure
- heart pacemakers
- DNA arrays
- smart syringes
- *in vitro* diagnostics
- drug delivery

The biomedical applications of BioMEMS have been growing only for about last ten years. It is also necessary to say that in comparison with automotive industry, where the market for microsystems is already mature for broad commercial applications, the market for BioMEMS is still in its development phase with chemical, flow and pressure sensors as its main driving forces.

However, as an integral part of BioMEMS, microvalves can be met both in therapeutic and diagnostic systems. An example of therapeutic application would be drug and gene delivery system. A diagnostic application is so called micro-total-analysis-systems (μTAS). Apart from size and weight, biocompatibility and overall security of the device must be foreseen. Moreover, if placed inside human body, the system must be controlled wirelessly and have an autonomous energy source [45]. This makes the task of designing and producing such a microvalve more complex.

A good example of commercially available microvalve for medical application would be a thermopneumatic microvalve device produced by Redwood Microsystems (Fig. 1.23).

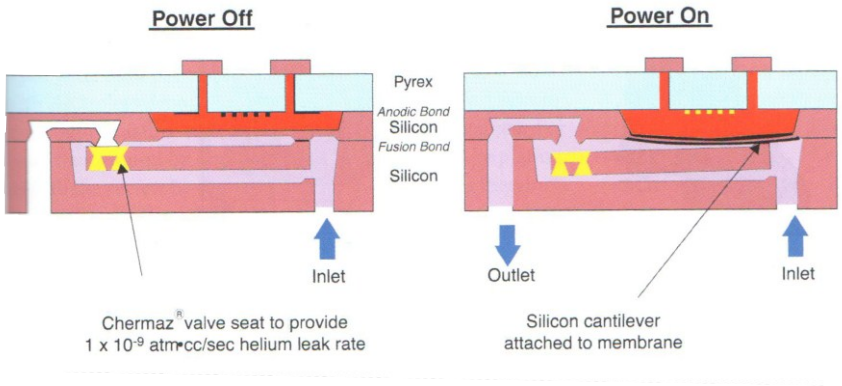

Figure 1.23: Thermopneumatic microvalve and its working principle (adapted from [15])

The performance of the device is reported to be comparable with macroscopic solenoid valves.

1.4.6.2 Aerospace applications of microvalves

Aerospace applications provide tremendous opportunities for different MEMS devices to be incorporated in many systems. First of all, one speaks here of MEMS sensors and gyros. However, there is also some place for microvalves. For example, in many cases sufficient and effective cooling is required (prevention of telescope overheating in order to minimize the infrared spectrum information distortion). In such systems microvalves can play a significant role [26]. The valves can be distributed in an array of cooling elements (Fig. 1.24), which will be placed across the structure to be cooled.

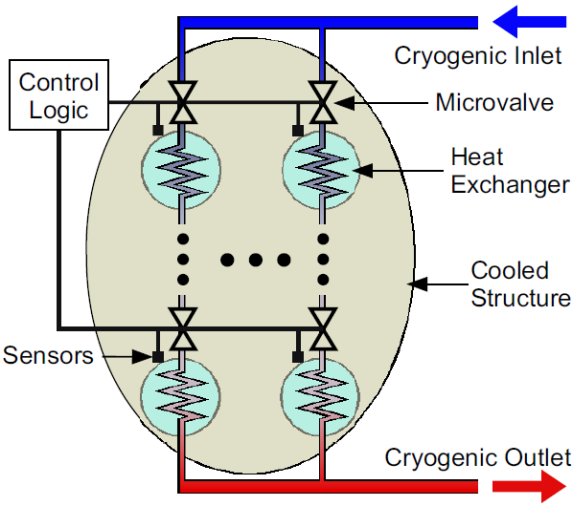

Figure 1.24: A distributed cooling system concept [26]

The effective temperature controlling is achieved by independent work of each element in response to the feedback from local sensors.

Since aerospace application requirements are extremely strict, mass, size and stable performance in a wide range of temperatures and pressures of the valve become very critical.

1.4.6.3 Microvalves in automotive industry

A typical car has about 50 valves that need to be opened and closed automatically and regulated closely [46]. Additionally, current trends to miniaturization and weight reduction could make utilization of microvalves in automotive production very attractive. Microvalves can be used for example in a car air-conditioning systems, or in micro-nozzle systems for fuel injection.

Until now however, to the author's best knowledge, there are no commercially available examples of microvalves built in a car.

1.4.6.4 Microvalves in environmental monitoring

MEMS are attractive in many environmental applications Micromachined devices are expected to be in such areas as sensors for detection of air and water pollution and such instruments as gas chromatography systems, microspectrometers and infrared detectors [15].

Miniature and accurate valves are good candidates to be used as sample injection-valves in hand-held gas chromatography systems (GC), which are usually large and fragile. Two companies have come up with commercially available bimetallic valves capable to be used in hand-held GCs. The first one is Hewlett-Packard with its normally-closed Ni/Si-membrane-valve, and the second one is IC Sensors with also normally-closed valve, but with aluminum region on a Si-diaphragm (Fig. 1.17). The already mentioned thermopneumatic valve made by Redwood Microsystems (Fig. 1.23) could also serve as a valve for GCs. However, it is thermally inefficient due to large volume of working fluid, difficult to assembly, and quite slow (~400 ms).

1.5 System and process specifications

The review of different microactuators and their applications given above clearly states the main requirements to be normally met by these devices. In a nutshell, they are

- small size
- low energy consumption
- high robustness
- high stability
- application flexibility
- high switching speed
- high operating temperature range
- low costs

The technological process developed in this work should result in a microactuator with following characteristics:

- actuation voltage: < 60 V
- switching speed: < 3 ms
- temperature range from: -10°C to +60°C
- working medium: gaseous (air, N_2)
- chip size: 8 × 8 × 2.5 mm^3

The process itself must incorporate mainly standard and easily achievable fabrication techniques. Furthermore, the possibility of microactuator integration into different devices must be foreseen in the process. For this work, a microvalve was chosen as a test-system for this task.

Though electrostatically actuated microvalves perform relatively poorly in terms of flow and pressure ranges, the electrostatic actuation principle, it is still a favorable one since it allows high switching speeds and small sizes at low costs. Apart of this, the characterization of technological process and its electroplating part is one of the main objectives of this work. Electrostatically actuated structures can be readily produced utilizing this method.

Finally, most of the electrostatically driven microvalves use parallel plate configuration of the charged electrodes (one of which is integrated with movable membrane, or is a membrane by itself). In this dissertation another approach is presented. A curved double-layer monometallic beam serves as a movable open/close element (Fig 1.25).

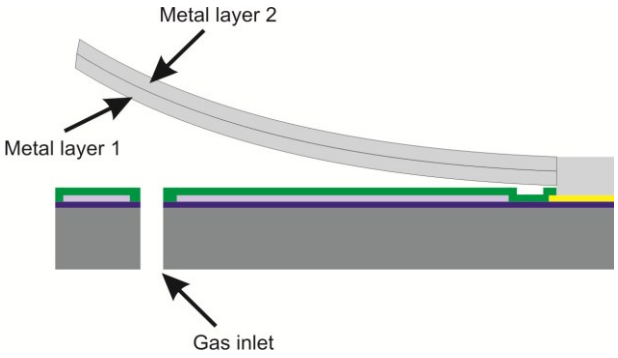

Figure 1.25: A general representation of a curved beam actuator for a microvalve.

This method allows increasing the gap between the electrodes thus, increasing the achievable flow rates while actuation voltage can still remain low. In general, the minimal gap near the anchor point as shown on Fig. 1.25 is mostly responsible for a minimal pull-in voltage. Should this voltage be applied between the electrodes, the upper electrode i.e. curved beam will be continuously attracted to the bottom one thus, closing the gap. On the other hand, since the gap increases towards the free end of the beam, it also allows higher flow rates.

The concept described above was realized on silicon substrates using the methods of microsystems manufacturing. A possibility of ceramic substrates utilization was also studied.

1.6 Structure of the dissertation

After the introduction, this work takes the reader through the Chapter 2 dedicated to the design and development of the actuator (and microvalve). Theoretical questions regarding the actuator micromechanics and fluid dynamics are discussed.

Chapter 3 describes the development of the technological process for microvalve fabrication. Main attention will be paid to the microelectroplating process and dry etching methods as the most critical ones in the fabrication chain. Technological process is presented. Also, the possibility of ceramic substrates utilization was studied in Chapter 3.

Chapter 4 deals with the characterization of the actuator and the microvalve. The mechanical robustness of the system is proved. This is necessary to assure that the fabrication process was designed correctly. Several actuator and microvalve performance tests are also described in Chapter 4.

Finally, in the Conclusion, all the work is summarized and possible directions and proposals for future development are given.

2 Chapter II: Theory and design

In this chapter, theoretical aspects of the actuator design as well as design itself will be discussed. First, definitions of electrostatic actuation, mechanical and electromechanical behavior of the actuator followed by estimation of the related system parameters will be given. Then, a brief theoretical description of flow behavior in a microvalve channel will be presented and estimations of microvalve channel geometry will be discussed. In the conclusion, final design variants will be presented.

2.1 Electrostatic actuation

Any design approach is based on a certain principle around which all the subsequent actions are concentrated. In the present work this principle is the electrostatic interaction. The following subsections describe nature of this phenomenon, the basics of electrostatic actuation, which will in turn help to derive the design equations for the curved beam actuator.

2.1.1 Basics of electrostatic actuation

Electrostatic interaction is based on the Coulomb's law, which states that the magnitude of the electrostatics force of interaction between two point charges in vacuum is directly proportional to the scalar multiplication of the magnitudes of charges and inversely proportional to the square of the distances between them [47].

In scalar form, this statement is described by the following expression

$$F_{el} = k_e \frac{q_1 \cdot q_2}{r^2}, \tag{2.1}$$

where

q_1 and q_2 – point charges,

r – distance between two point charges,

k_e – proportionality constant, or Coulomb's constant which is related to the defined properties of space

$$k_e = \frac{1}{4\pi\varepsilon_0}, \tag{2.2}$$

where, in turn

ε_0 – electric constant.

Figure 2.1 illustrates the mechanism of Coulomb's law.

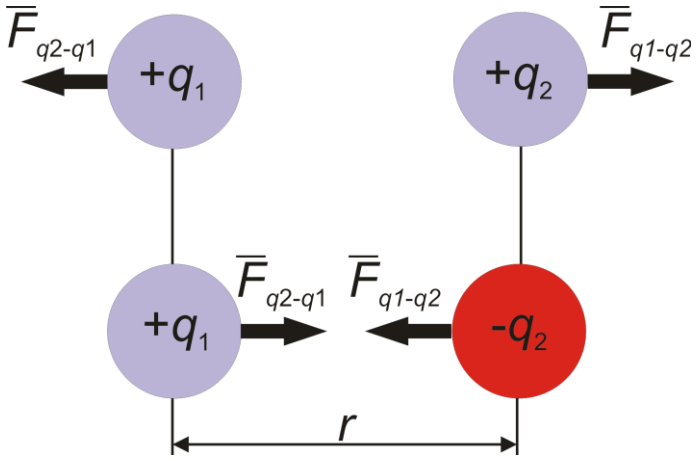

Figure 2.1: The mechanism of electrostatic interaction.

In vector form, the Coulomb's law can be written as

$$\vec{F}_{12} = k\frac{q_1 \cdot q_2}{r_{12}^2}\frac{\vec{r}_{12}}{r_{12}} \tag{2.3}$$

where

r_{12} – distance between charge 1 and charge 2
$\vec{r}_{12}$ – vector from charge 1 to charge 2, equal in magnitude to r_{12}

Obviously, the charges of the same sign are pushed away from each other, whereas the charges which have different sign are pulling towards each other.

If there are more than two charges, the superposition principle may be used to determine the force due to a system of N charges on a small test charge q

$$\vec{F} = kq\sum_{i=1}^{N}\frac{q_i(\vec{r}-\vec{r}_i)}{|r-r_i|^3} \tag{2.4}$$

For a charge distribution an integral over the region containing the charge is equivalent to an infinite summation, treating each infinitesimal element of space as a point charge dq. Equations 2.5 – 2.7 represent the charge distribution per unit length, unit area, or unit volume respectively

$$dq = \lambda(r')dl' \tag{2.5}$$

$$dq = \sigma(r')dA' \tag{2.6}$$

$$dq = \rho(r')dV' \tag{2.7}$$

Here $\lambda(r')$ is the charge per unit length, $\sigma(r')$ is the charge per unit area, and $\rho(r')$ is the charge per unit volume at position r'.

The force on an elementary charge q' at the position r is then given by

$$\vec{F} = kq' \int \frac{\vec{r} - \vec{r}'}{|r - r'|^3} dq \tag{2.8}$$

The phenomenon described above has practical meaning. When voltage U is applied, a parallel plate capacitor can be seen as a system of charges of opposite polarity distributed over two separated flat areas parallel to each other and separated by a distance d (Fig. 2.2).

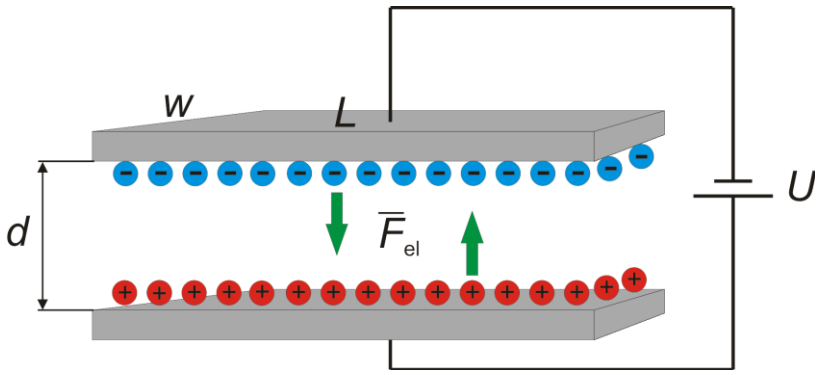

Figure 2.2: Parallel plate capacitor.

The capacitance of this system is given by

$$C = \varepsilon \frac{A_{el}}{d} \tag{2.9}$$

where

$\varepsilon = \varepsilon_0 \varepsilon_r$ – permittivity, with ε_0 – relative permittivity of the dielectric material between the plates, and $\varepsilon_r = 8.85 \times 10^{-12}$F/m – vacuum permittivity

$A_{el} = wL$ – area of the plates, with w – plate width, L – plate length

The attracting force F_{el} will appear between these two plates. To derive this force, we can start by writing the expression for the total potential energy of the capacitor

$$E_{pot} = \frac{1}{2} CU^2 = \frac{1}{2} \varepsilon \frac{A_{el}}{d} U^2 \tag{2.10}$$

The force between the plates is obtained by deriving Equation 2.10

$$F_{el} = \frac{dE_{pot}}{dd} = \frac{1}{2}\varepsilon\frac{A_{el}}{d^2}U^2 \tag{2.11}$$

If for example one plate remains fixed, and a counteracting force is somehow (e.g. spring) applied to another one, the system may act as an actuator. This can be schematically represented as:

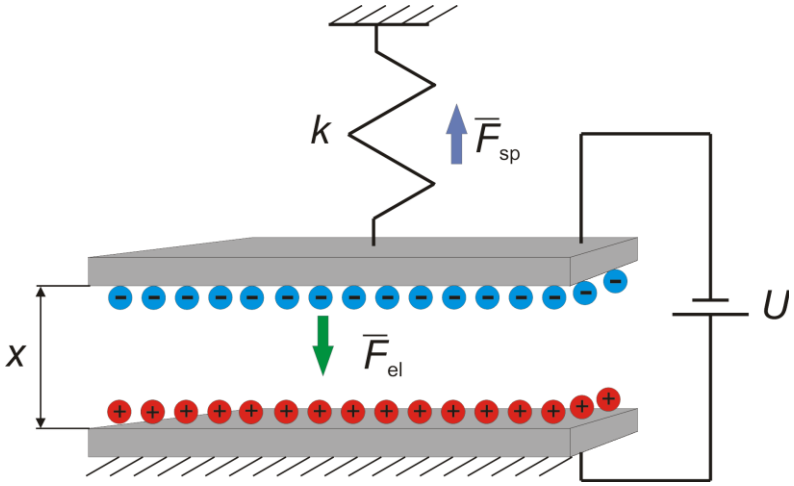

Figure 2.3: Schematic of an electrostatic actuator.

As the distance between the plates is subject to change in this case so are the capacitance C and consequently the force F_{el} (see Eq. 2.09 – 2.11). If d is the initial distance without any applied voltage then after the voltage was applied, the upper plate will move to the position $d - x$, where x is the displacement.

The spring will act in an opposite direction with force F_{sp} trying to restore the initial state of the system. The force of the sprig is given by

$$F_{sp} = kx \tag{2.12}$$

where k is the spring constant.

At equilibrium, $F_{el} = F_{sp}$, hence

$$kx = \frac{1}{2}\varepsilon\frac{A_{el}}{(d-x)^2}U^2 \tag{2.13}$$

It is now easy to find an expression for a pull-in voltage of a parallel plate electrostatic actuator, for example as it is done in [48].

The total force acting on a movable plate is

$$F_{tot} = F_{el} - F_{sp} = \frac{1}{2}\varepsilon\frac{A_{el}}{(d-x)^2}U^2 - kx \tag{2.14}$$

Deriving Equation 2.14 one obtains the stiffness of the system

$$\frac{dF_{tot}}{dx} = \varepsilon \frac{A_{el}}{(d-x)^3} U^2 - k \tag{2.15}$$

Substituting Eq. 2.13 returns stiffness around the equilibrium point

$$\frac{dF_{tot}}{dx} = \frac{2kx}{d-x} - k \tag{2.16}$$

The unstable point is defined by $\frac{dF_{tot}}{dx} = 0$ resulting in

$$x = \frac{1}{3} d \tag{2.17}$$

Substituting Eq. 2.17 to Eq. 2.13 gives the pull-in voltage of parallel plate electrostatic actuator

$$U_{pi} = \sqrt{\frac{8}{27} \frac{kd^3}{\varepsilon A_{el}}} \tag{2.18}$$

The pull-in voltage turns out to depend on the actuators geometry and elastic properties of the spring material as well as on the dielectric properties. Of cause, depending on application, additional influencing parameters such as differential pressure (in case of a microvalve) can contribute to pull-in voltage.

Often there is no separate spring attached to a movable plate. Instead, the plate itself acts as a spring. This is true for cantilever beams and membranes. In this work, a bended cantilever beam concept is used. The following subsection describes the theory behind the mechanical and electrical properties of such a system.

2.1.2 Curved cantilever beam microactuator concept

Figure 2.4 schematically represents the basic mechanical concept of the prototype curved beam electrostatic microactuator developed in this work. Consider a cantilever beam of length L_a consisting of two layers of metal with thickness d_1 and d_2, internal stress σ_1 and σ_2, and Young's modulus E_1 and E_2. Suppose also that the properties of the material remain constant inside the layer.

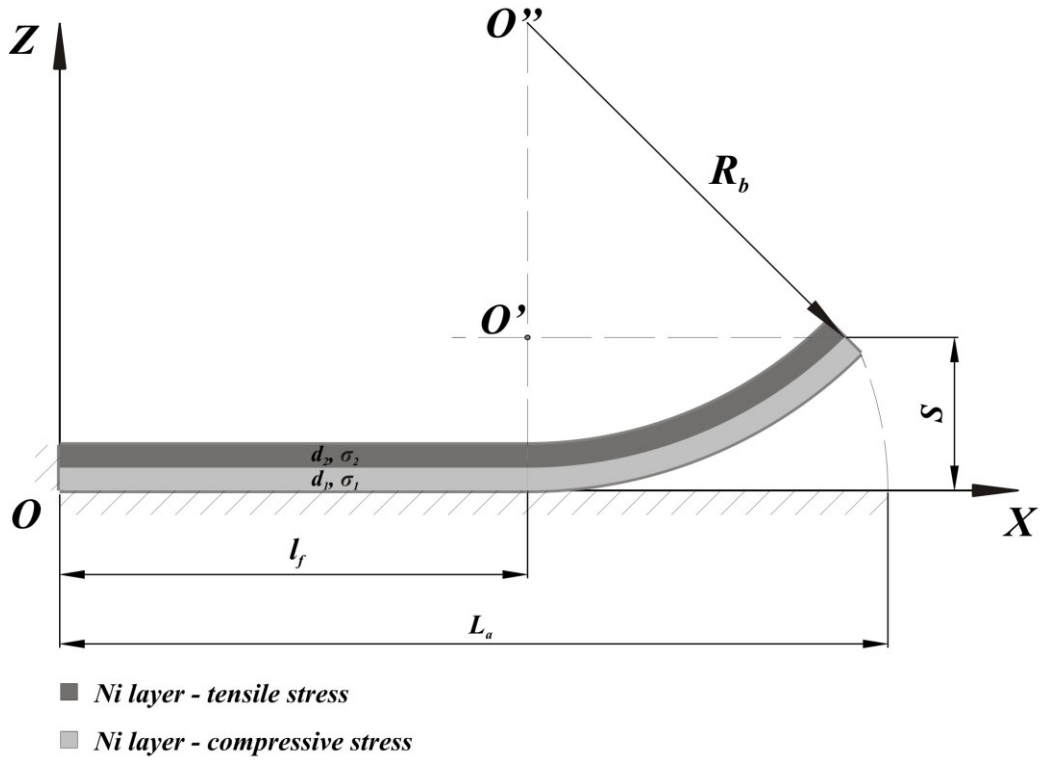

Figure 2.4: Microactuator mechanical concept [49]

In order to achieve the desired vertical deflection *s* at the tip of the actuator a single metal double-layer approach was used. In this case, bending of a beam is caused by difference in internal stresses inside these layers. The internal stress gradient appears due to variation of the electroplating process parameters for each layer[5]. If there is a tensile stress inside one of the layers whereas the other one has compressive stress, the beam will bend until the internal bending forces become balanced. In equilibrium state the system will have certain bending radius R_b. Knowing this radius, it is possible to geometrically estimate the deflection.

In Figure 2.5, the electrostatic working principal is shown

[5] Discussed in Chapter 3 Technology and fabrication.

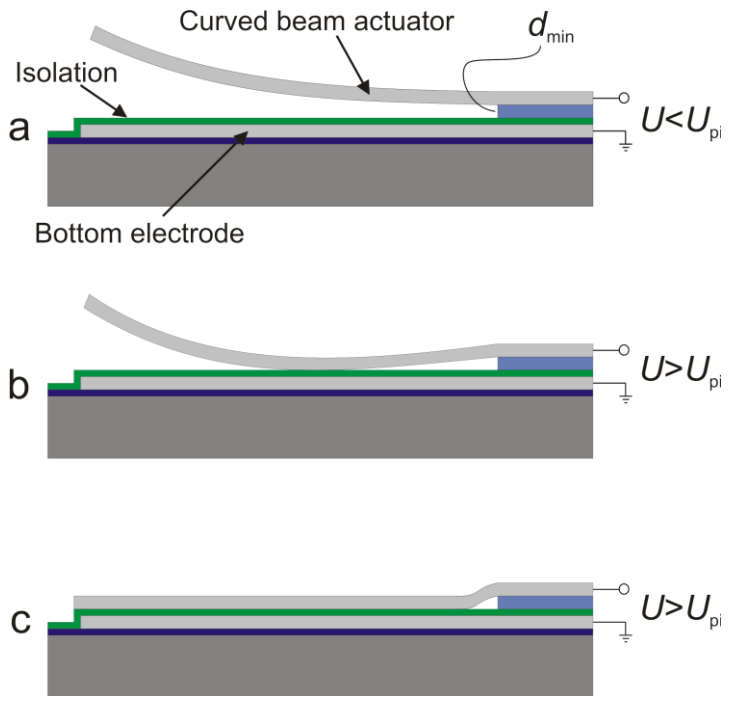

Figure 2.5: The electrical working principal of the curved beam electrostatic microatuator

The flat unmovable electrode is situated on the substrate and is electrically isolated from both the movable electrode which is a curved cantilever beam and the substrate. The minimal distance d_{min} between the electrodes is close to the anchor point of the cantilever beam. This distance together with a number of other parameters defines the pull-in voltage U_{pi}.

As Figure 2.5a shows, if there is no applied voltage or this voltage is lower than U_{pi} the actuator stays in its initial equilibrium position where its curvature is only defined by internal stresses. However, as soon as applied voltage exceeds U_{pi} the beam will bend towards the bottom electrode until it lies almost completely flat on the isolation layer (Fig. 2.5b and 2.5c).

In order to define such design parameters as deflection s at any moment of time and pull-in voltage U_{pi}, it is necessary to define the geometry of the beam's bending line $w(x,U)$, which is influenced on one hand by already mentioned internal stress gradient and on the other hand by electrostatic forces acting on the beam [50]. This statement is illustrated in Figure 2.5

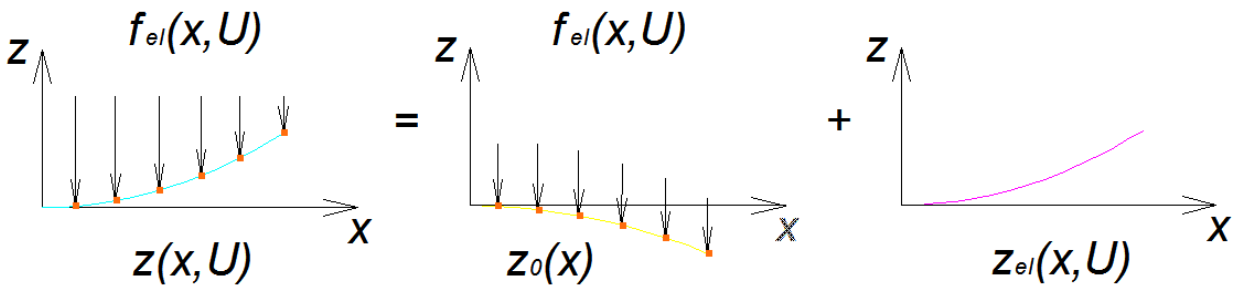

Figure 2.6: Actuators bending curve as a result of internal stress gradient and external electrostatic force

Thus, $z_0(x)$ is a bending line due to only internal stresses and $z_{el}(x,U)$ is a bending line due to electrostatic force[6]. Their superposition gives the resulting bending line $z(x,U)$

$$z(x,U) = z_0(x) + z_{el}(x,U) \tag{2.19}$$

Let us first determine the expression for a bending due to electrostatic force.

The bended beam and fixed electrode naturally form a capacitor with variable distance between them along the X-axis. Therefore, it is necessary to subdivide all the length into elementary discrete elements (capacitors) of length Δx and width w. Furthermore, the distance between the electrodes d_{cap} must be defined as

$$d_{cap}(x,U) = z(x,U) + d_{eff} \tag{2.20}$$

with

$$d_{eff} = \sum_j \frac{d_{iso,j}}{\varepsilon_j} \ , \tag{2.21}$$

where

$d_{iso,j}$ – thickness of the isolation layer j
ε_j – permittivity of the isolation layer j

The capacitance of the elementary capacitor considering Equation 2.10 will then be

$$C(x,U) = \varepsilon \frac{w}{d_{cap}(x,U)} \Delta x \,, \tag{2.22}$$

and consequently the electrostatic force between the plates of the elementary capacitor

$$F_{cap}(x,U) = \frac{1}{2} U^2 \frac{dC(x,U)}{dd_{cap}(x,U)} \tag{2.23}$$

Hence, dividing Equation 2.23 by Δx one receives electrostatic load per unit length

$$f_{el}(x,U) = \frac{1}{2} \varepsilon \frac{w}{d_{cap}{}^2(x,U)} U^2 \tag{2.24}$$

[6] The latter is obviously also a function of a longtitudal distance x, since the gap between the electrodes changes as well.

Now, taking into consideration the resulting load torque

$$M_L(x,U) = \int_{\xi=x}^{L} f_{el}(\xi,U)\cdot(\xi - x)d\xi \tag{2.25}$$

and the differential equation for the bending line at small deflections as a function of the bending strength c_R

$$\frac{z''_{el}(x)}{\sqrt{(1+z'^{2}_{el}(x))}} = \frac{M_L}{c_R} \approx z''_{el}(x) \tag{2.26}$$

one can get the final differential expression for the deflection caused by electrostatic force combining the Equations 2.24, 2.25, and 2.26

$$z''_{el}(x,U) = \frac{1}{2}\varepsilon U^2 \int_{\xi=x}^{L} \frac{w(\xi)}{c_R(\xi)} \cdot \frac{(\xi - x)}{\left[d_{eff} + z_0(\xi) + z_{el}(\xi,U)\right]^2} d\xi \tag{2.27}$$

Equation 2.27 is strongly nonlinear. It can only be solved numerically [50]. However, in most cases it is only necessary to know the parameters at the initial and final position. These parameters define for example the maximal deflection of the beam, which in turn can be used during microvalve flow calculations if the actuator is used as a microvalve open/close element, or on the other and, for definition of the necessary pull-in voltage. Initial bending of the beam is only defined by its geometry and material properties. It will be derived in the following subsections.

2.1.3 Beam bending radius and deflection

As it has already been mentioned in subsection 2.1.2, in the initial position, before pull-in voltage is applied, the bending of the beam will only be caused by internal stress gradient due to mechanical properties of the material and the geometry of the beam. This bending will stay constant. Thus, the bending radius R_b will stay constant as well and can be defined as a reciprocal of the second derivative of the bending line [50], [51]

$$R_b = \frac{1}{z(x,U)} = \frac{c_R}{M_L(x;U)}\ , \tag{2.28}$$

or taking into considerations that no voltage is applied in the initial position

$$R_b = \frac{1}{z''(x)} = \frac{c_R}{M_L} \tag{2.29}$$

Now, the load torque M_L and the bending strength c_R must be defined. In order to do that, the neutral axis of the multilayered beam should be found. According to the definition, "a neutral axis is an axis in the cross section of the beam along which there are no longitudinal stresses and strains" [52]. In the simplest case, i.e. the cross section is symmetric, isotropic and is not curved before a bend occurs the neutral axis is a central axis of symmetry. The situation changes if the body of a beam is not isotropic. For example, as in our case, it consists of several layers of materials with different elastic properties.

Consider a beam of j layers as shown in Figure 2.7

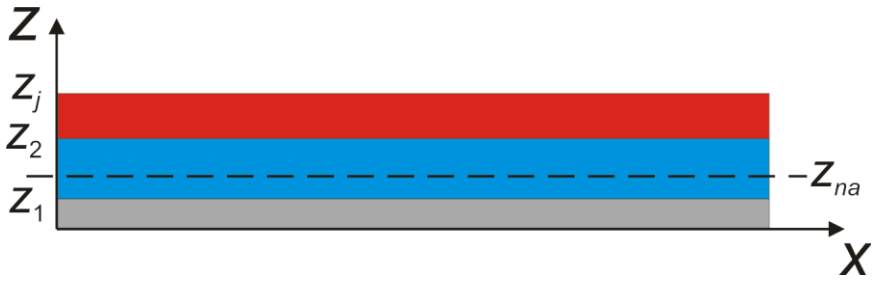

Figure 2.7: Neutral axis in a beam of j layers

The position of the neutral axis depends on the width b_j and on the Young's modulus E_j of each layer

$$z_{na} = \frac{\int_z b(z)E(z)zdz}{\int_z b(z)E(z)dz} = \frac{\int_0^{z_1} b_1E_1zdz + \int_{z_1}^{z_2} b_2E_2zdz + \ldots + \int_{z_{j-1}}^{z_j} b_jE_jzdz}{\int_0^{z_1} b_1E_1dz + \int_{z_1}^{z_2} b_2E_2dz + \ldots + \int_{z_{j-1}}^{z_j} b_jE_jdz} \tag{2.30}$$

We agree on the material parameters within the bulk of the layers to be constant. Moreover, the widths are the same for all the layers and are constant. Thus, after integration, for a system of two layers, the position of the neutral axis will be

$$z_{na} = \frac{1}{2}\frac{E_1{z_1}^2 + E_2({z_2}^2 + 2z_1z_2)}{E_1z_1 + E_2z_2} \tag{2.31}$$

Now, it is possible to define the internal load torque M_L responsible for the bending of the beam, and the bending strength c_R.

The internal load torque depends on mechanical stresses σ_j inside the corresponding layers. Figure 2.8 depicts a system of j layers and internal stresses inside them. Negative values of σ_j are for compressive stress, positive ones are for tensile stress.

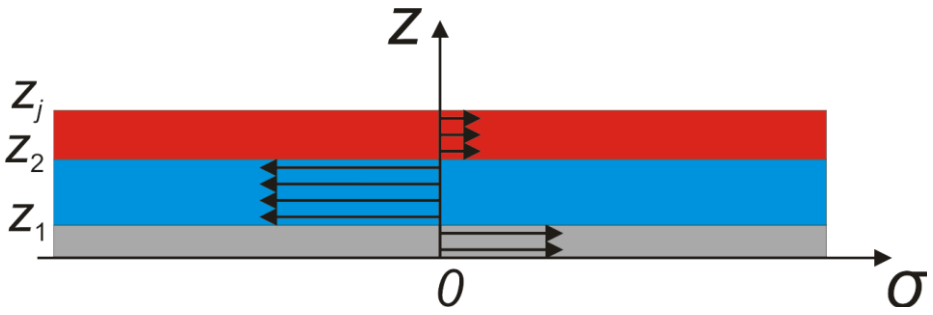

Figure 2.8: Mechanical stresses inside a multilayered beam

There are two main reasons causing internal stress. First is a different process temperature during the production of layers. Later on, when a system is situated under a certain common temperature, different coefficients of thermal expansion will make it bend.

The second reason is connected to the material grain growth. Even if the same material is used, on the border between two layers continuous grain growth is interrupted and the grains begin to grow anew. Moreover, if different process parameters are used, grain size can differ from that in the previous layer. Thus, stress gradient between the two layers appears [51].

As stated in [53], the internal load torque for a system of j layers is

$$M_L = \int_z \sigma(z)b(z)(z-z_{na})dz = \int_0^{z_1} \sigma_1 b_1 (z-z_{na})dz + \int_{z_1}^{z_2} \sigma_2 b_2 (z-z_{na})dz + \ldots + \int_{z_{j-1}}^{z_j} \sigma_j b_j (z-z_{na})dz \quad (2.32)$$

After integration, and taking into consideration that the width b is the same for all the layers, for a system of two layers, the internal torque will be defined as

$$M_L = b\left\{\sigma_1\left[\frac{1}{2}z_1^2 - z_1 z_{na}\right] + \sigma_2\left[\frac{1}{2}(z_2^2 + 2z_1 z_2) - z_2 z_{na}\right]\right\} \quad (2.33)$$

The bending strength c_R which also defines the spring's elastic force can be found using the following equation

$$c_R = \int_z b(z)E(z)(z-z_{na})^2 dz = \int_0^{z_1} b_1 E_1 (z-z_{na})^2 dz + \int_{z_1}^{z_2} b_2 E_2 (z-z_{na})^2 dz + \ldots + \int_{z_{j-1}}^{z_j} b_j E_j (z-z_{na})^2 dz \quad (2.34)$$

Again, after integration for the system of two layers

$$c_R = bE_1\left[\frac{1}{3}z_1^3 - z_1^2 z_{na} + z_1 z_{na}^2\right] + bE_2\left[\frac{1}{3}\left\{z_2^3 + 3z_1 z_2 (z_1 + z_2)\right\} - \left\{z_2^2 + 2z_1 z_2\right\}z_{na} + z_2 z_{na}^2\right] \quad (2.35)$$

Using Equations 2.30, 2.34 and 2.36 one can find the static deflection of the bended beam due to internal stress gradient s_t at its tip point. Considering the data from Figure 2.4 and the approximation $R_b >> L_a$, after simple geometrical calculations [50], [51], one can write

$$s_t = R_b\left[1-\cos\left(\frac{L_a - l_f}{R_b}\right)\right] \approx \frac{1}{2}\frac{(L_a - l_f)^2}{R_b} = \frac{M_L (L_a - l_f)^2}{2c_R}, \tag{2.36}$$

where

L_a – total length of the beam
l_f – length of the flat part of the beam resting on the bottom electrode
R_b – beam bending radius

Similarly, deflection of the beam at any other point can be found by replacing the total length L_b by the corresponding length of the beam at this point.

2.1.4 Beam pull-in voltage

Pull-in voltage U_{pi} is one of the critical parameters to be defined during the design of the actuator and represents the operational limits between stable and unstable behavior of an electrostatic system. It is important to detain the beginning of the pull-in in order to achive better performance of the device [54].

It is out of the scope of the present work to develop a high precision analytical model for a curved cantilever beam. Such models exist [54], [55] and return excellent results, but they require a huge number of mathematical calculations including usage of special mathematical software to solve the systems of differential equations. Another approach based on FEM simulations exist. This method is also a good one in case when high precision is needed. But due to high complexity of the model[7] and non-linear behavior of a curved beam, model generation and meshing itself become very complex and time-consuming. Fringing effects [55] are not considered in this work, either.

In the following, a simple model for estimation of a pull-in voltage for a given set of parameters will be derived. The theoretical formulation is based on the models developed in [50], [51], [54], [56].

Figure 2.4 represented the geometry of a curved cantilever beam. For such geometry, voltage dependent tip deflection $s_{el}(U)$ can be defined as [56]

$$s_{el}(U) = \frac{L_b b k \varepsilon_0 U^2}{4 E_{eff} I}\int_0^{L_b}\left(\frac{x}{d_{sl}+s_t}\right)^2 dx, \tag{2.37}$$

where

k – effective dielectric constant, approximated value $k = 1,2046$ [56]
s_t - static deflection of the bended beam due to internal stress gradient as in Eq. 2.36

[7] A multiphysics problem: electrostatics and mechanics.

d_{sl} – minimal gap between the curved beam and the isolation layer
I – moment of inertia
E_{eff} – effective Young's modulus, $E_{eff} = E/(1-\nu^2)$ for beams with $b \geq 5(z_1+z_2)$ [54]
ν – Poisson's ratio

According to [48], pull-in occurs when

$$s_{el}(U) = \frac{z(x,U)}{3} \tag{2.38}$$

Taking into consideration Eq. 2.38 and solving 2.37 with respect to U returns

$$U_{pi} = \sqrt{\frac{2E_{eff}Is_t}{L_b bk\varepsilon_0 \int_0^{L_b}\left(\frac{x}{d_{sl}+s_t}\right)^2 dx}} \tag{2.39}$$

The definite integral in Eq. 2.39 can be represented as

$$\int_0^{L_b}\left(\frac{x}{d_{sl}+s_t}\right)^2 dx = 2R_b\left[\frac{\tan^{-1}\left(\frac{L_b}{\sqrt{2d_{sl}R_b}}\right)}{\sqrt{2d_{sl}R_b}} - \frac{L_b}{2d_{sl}R_b+L_b^2}\right] = \Pi, \tag{2.40}$$

where

R_b – beam bending radius as in Eq. 2.29

Substituting the definite integral in Eq. 2.39 with Eq. 2.40 results in

$$U_{pi} = \sqrt{\frac{2E_{eff}Is_t}{L_b bk\varepsilon_0 \Pi}} \tag{2.41}$$

2.1.5 Breakdown voltage

An important question during the design of any electrostatically actuated device is at what voltage electrical breakdown will happen. In other words, when will the electrical arc take place? This would define the highest voltages, which the device can withstand without damages.

To a certain extent, the answer to this question is given by Paschen's Law. The law states that the breakdown voltage U_{BD} is a function of the product of the gas pressure p and the distance between the electrodes d

$$U_{BD} = f(p \cdot d) = \frac{Apd}{\ln(pd) + B} \tag{2.42}$$

where

A and B – coefficients depending on the composition of the gas [57].
Figure 2.8 illustrates the curves for different gases.

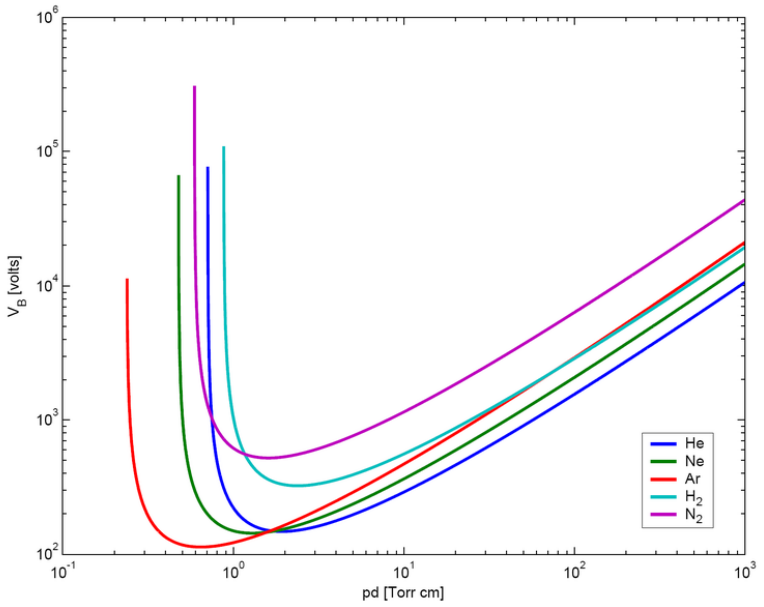

Figure 2.9: Breakdown voltage vs. gas pressure [57]

It can be clearly seen that for high voltage applications the voltage gain on the left side of the minimum can be used.

Paschen's Law is only valid for electrodes with uniform electric field. Hence, it can only be carefully applied in this work, where one of the electrodes is curved. Furthermore, its validity is limited for small distances between the electrodes due to the fact that at high field strength, collision ionization at the electrodes prevails [58]. This means that for the distances smaller then several tenths of microns the dielectric strength of the electrodes gap cannot be improved by decreasing gas pressure p [51].

2.1.6 Stiction phenomena and antistiction stand-off bumps.

Stiction (or sticking) is a phenomenon of adherence of two surfaces to each other. In case of microstructures it can be adherence of an actuator beam to the surface of the bottom electrode, or rather to the isolation layer covering this electrode.

Stiction is caused by solid-to-solid binding forces appearing when two flat surfaces are placed very close to each other. These forces can be large enough to overcome the spring force of the beam, which is responsible for returning it to the initial state after the voltage is turned off. In this case the beam will stay in contact with bottom electrode and the device (valve or relay) will not function. In surface micromachining stiction often first occurs after the wet etching of the sacrificial layer when drying process is initiated. The structures undergo deflection due to

capillary forces caused by surface tension of the remaining liquid between microstructures. Deflection decreases the gap between the structures and this in turn lets solid-to-solid forces pin them together.

One possible solution could be additional force applied to the beam to tear it off the surface. This solution is used in this work in a form of the prestressed actuator beam. Internal stress gradient makes the beam bend upwards after the release etching, working against stiction forces. Among the other methods are usage of structure supporting organic pillars, supercritical CO2 drying, and coating of structures with self-assembly monolayers (SAMs). Dry etching methods are used to avoid stiction, but they do not guarantee that stiction will not appear later. There are, however, other possibilities which are hidden in the design of the beam itself.

Stiction strength is directly proportional to the surface energy of the structures. Hence, by decreasing the surface energy one can decrease stiction. The surface energy depends on the material. For Ni it is quite high, about 2,34 J/m^2 [59][8]. Ni was chosen as a material for the actuator in this work for its good manufacturability and mechanical properties. Hence, this solution cannot be used in this work.

Fortunately, the surface energy is also directly proportional to the total contact area [5]. Therefore, reduction of the total contact area will reduce stiction. This can be done by incorporating small 15 µm ×15 µm stand-off bumps on the bottom surface of the beam. During the operation, only these bumps will touch the isolation layer of the bottom electrode. The concept is shown in Figure 2.10

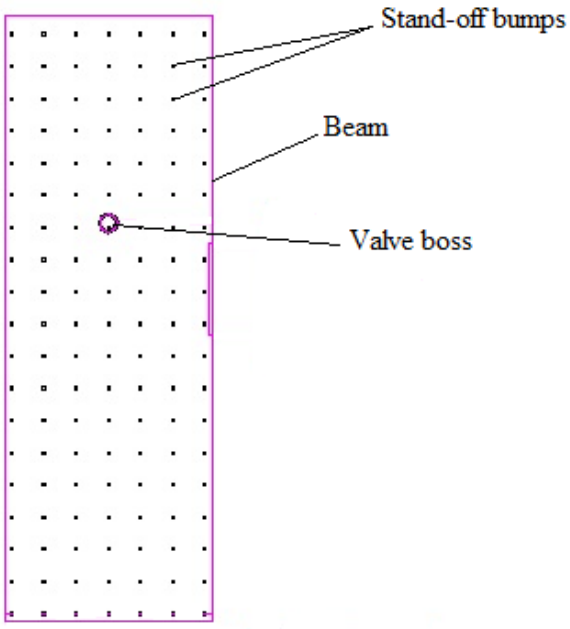

Figure 2.10: Anti-stiction bumps on the bottom side of the actuator

The distance between the bumps is 195 µm. The big circular bump in the middle serves as a valve boss for a microvalve application of the actuator. It can also be used as a contact bump in for example relay application.

[8] Compared to e.g. polycrystalline silicon (0,14±0,07 J/m2), or solidified gelatin (0,12±0,008 J/m^2) [5]

Now, it is necessary to define the maximum height of the beams h_b with respect to the distance between them a_b, the thickness of the actuator t, and to the applied voltage U.

The consideration here is that the parts of the actuator beam between the bumps should never touch the isolation of the bottom electrode. Otherwise the whole conception of the contact surface minimization will not be valid anymore.

Consider an elementary square section of the beam supported by 4 anti-stiction bumps as shown in Figure 2.11

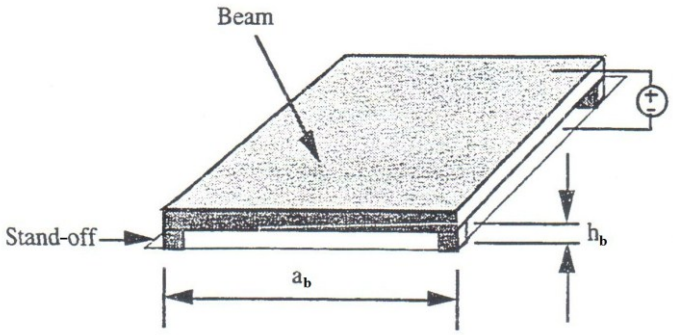

Figure 2.11: A single section of a deflected beam supported by stand-off bumps at it's four corners (adapted from [5])

Electrostatic force between the plate and the bottom electrode is inversely proportional to the distance between them. Non-linear nature of the electrostatic force makes it difficult to determine the exact solution for the deflection of the center of the plate. But for the worst case, which is exactly the bumps height h_b, a simple approximation can be derived. That is, an electrostatic force for the $h_b/2$ will be calculated and then applied uniformly over the entire plate [5]. The uniformity of the force leads to the possibility of an analytical solution for the deflection at the centre of the square section if it is supported at four corners with periodic boundary conditions as it is shown in Figure 2.11.

As stated in [60], the maximum deflection at the center of a plate described above is given by

$$\delta_{\max} = \frac{12\alpha(1-\nu^2)a_b^4 f_a}{Et^3} \tag{2.43}$$

where

f_a – uniform force per unit area
α – coefficient for a square array (α = 0,00581)
ν – Poisson's ration (ν_{Ni} = 0,31)
E – Young's modulus

The electrostatic force F_{el}, applied to the section is in this case (see Eq. 2.12)

$$F_{el} = \frac{1}{2}\varepsilon \frac{A_{el}}{\left(\frac{h_b}{2}\right)^2} U^2 \tag{2.44}$$

The force per unit area is defined as

$$f_a = \frac{F_{el}}{A_{el}} = \frac{\varepsilon U^2}{2\left(\frac{h_b}{2}\right)^2} \tag{2.45}$$

Substituting Equation 2.45 in Equation 2.43 returns

$$\delta_{\max} = \frac{24\alpha(1-\nu^2)a_b^4 \varepsilon U^2}{Et^3 h_b^2} \tag{2.46}$$

Substituting $h_b/2$ for maximum deflection and solving for h_b yields

$$h_b \geq \sqrt[3]{\frac{48\alpha(1-\nu^2)a_b^4 \varepsilon U^2}{Et^3}} \tag{2.47}$$

Equation 2.47 defines the minimum anti-stiction bump height. The maximum height can be limited by a desired device parameter, e.g. maximum leak rate of the valve.

For given geometry, material properties of Ni and maximum applied voltage U = 60 V [9], $h_b \geq$ 200 nm.

2.1.7 Actuator reaction time

Very often, an operational speed of the device becomes an indispensible parameter. For example, it is always important to know how fast a relay can switch, or how fast a valve can open or close. The principle of the actuator's movement is shown in the Figure 2.12[10].

The beam is assumed to be initially in an upward deflected state (Fig. 2.12 a). When the pull-in voltage is applied, the beam simultaneously begins to uncurl and move downward to the bottom electrode. When a portion of the beam reaches the height of approximately 1/3 of the $d_{\min}$, the beam will rapidly pull-down to the surface (Fig. 2.12 b and c). This pull-down time is neglected. After the voltage is turned off, the beam will return to its initial state. Residual charges can make this phase slower than closing phase. But in the presence of internal stress gradient contributing to the restoring deflection, their influence can be neglected too.

[9] Worst case as defined in specifications (see 1.5)

[10] This is simply a copy of Figure 2.5 repeated here in order to make reading more comfortable.

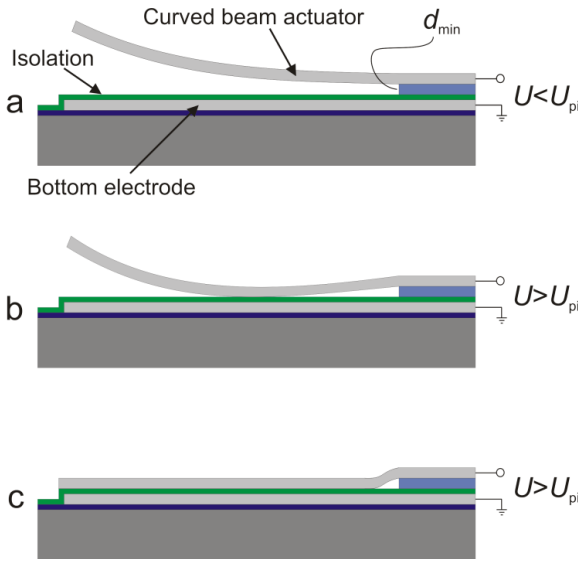

Figure 2.12: Microactuator's closing behavior

Maximum speed at which a cantilever beam can vibrate is defined by its undamped circular frequency ω_0 [61]

$$\omega_0 = \sqrt{\frac{1}{cm_{eff}}} = \left\{ \begin{array}{l} m_{eff} = \frac{33}{140} m = \frac{33}{140} \rho V \\ \frac{1}{c} = k_s = \frac{E_{eff} b \sum_i z_i^3}{4 L_b^{\ 3}} \end{array} \right\} = \sqrt{\frac{35 E_{eff} b (z_1^3 + z_2^3)}{33 L_b^{\ 3} \rho V}} = \frac{1}{L_b^{\ 2}} \sqrt{\frac{35 E_{eff} (z_1^3 + z_2^3)}{33 \rho (z_1 + z_2)}} \quad (2.48)$$

The undamped natural frequency is related with the circular frequency as:

$$f_n = \frac{\omega_0}{2\pi} \quad (2.49)$$

Knowing this frequency, one can easily estimate the time of one vibration cycle, or actuators reaction time t_r. Since the beam will only undergo one half of the complete cycle, we should take only one half of this time, e.g.

$$t_r = \frac{2}{f_n} \quad (2.50)$$

This approach allows only an approximate estimation of the actuators closing speed. For more precise calculations, damping and beam stiffness must be taken into consideration. In order to reduce damping and also to provide better and faster sacrificial layer etching, the array of technological through-beam orifices was foreseen.

2.1.8 Dimensioning of the actuator's beam

Having derived all the necessary equations in previous subsections, one can calculate the actuators mechanical and geometrical parameters. First of all, it is necessary to summarize and classify the most important parameters (Table 2.1)

Table 2.1: Classification of basic parameters for actuator's dimensioning

Parameter	Sign	Type	Value	Comments
Width	b	Design	500…1500 µm	Limited by chip dimensions
Length	L_b		2500…4500 µm	
Ni layer 1 thickness	z_1	Design/Process	0…2 µm	Thickness of the microform
Ni layer 2 thickness	z_2		15…20 µm	Thickness of the microform
Sacrificial layer thickness	d_{sl}		0.2…1 µm	-
Isolation layer thickness	d_{iso}		0.2…0.6 µm	-
Ni layer 1 stress	σ_1	Process	-15..-30 MPa	Limited by desired beam deflection
Ni layer 2 stress	σ_2		10..20 MPa	
Ni Young's modulus	E	Material	200 Gpa	Material property
Pull in voltage	U_{pi}	Output	< 60 V	Specifications, Eq. 2.42
Beam deflection	s_t		< 60 µm	Eq. 2.37
Anti-stiction bump height	h_b		-	To be calculated, Eq. 2.49
Switching time	τ_{min}		< 3 ms	Specifications, Eq. 2.54

The design parameters are freely[11] defined by engineer and can be varied to achieve optimal output parameters. Design/Process and process parameters have more limitations due to the nature of technological processes involved here.

The main equations involved into the calculations are

Eq. 2.36 – static deflection s_t
Eq. 2.41 – pull-in votage U_{pi}
Eq. 2.47 – stand-off bumps height h_b
Eq. 2.50 – actuator's reaction time t_r

The stand-off bumps height h_b was calculated in the subsection 2.1.6 and as should be not less than 200 nm.

[11] Can be varied in the limits of technical specifications

2.1.8.1 Static deflection

Static deflection due to internal stress gradient depends on design and design/process parameters of the actuator. Figure 2.10 presents the dependence of static deflection on the length of the actuator cantilever beam L_b at constant beam width b = 500 µm. Material and process parameters were also set constant: $E_1 = E_2 = E$ = 200 GPa, σ_1 = 20 MPa, σ_2 = -12 MPa, z_1 = 2 µm, z_2 = 18 µm

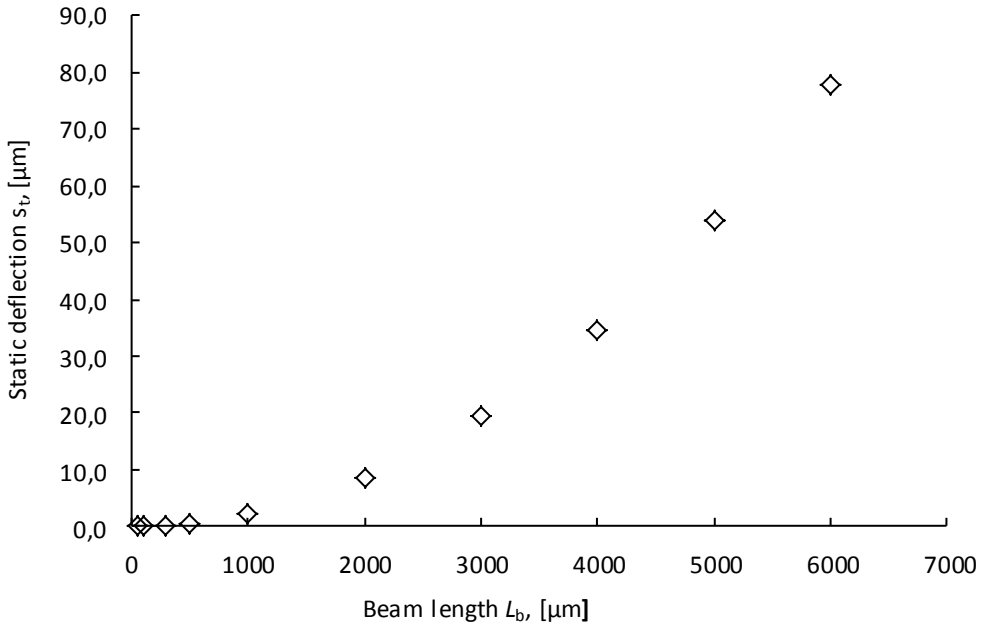

Figure 2.10: Static deflection of the double layered nickel actuator

Proper deflections of 10 to 40 µm can be achieved at lengths of 2000 to 4500 µm.

Mathematically, static deflection s_t does not depend on b, but depends on L_b, σ_1/σ_2 and z_1/ z_2. Figure 2.11 illustrates some possible variations of s_t in dependence on the ratios $z_1/ z2$ and σ_1/σ_2. Here, L_b = 3000 µm and b = 500 µm.

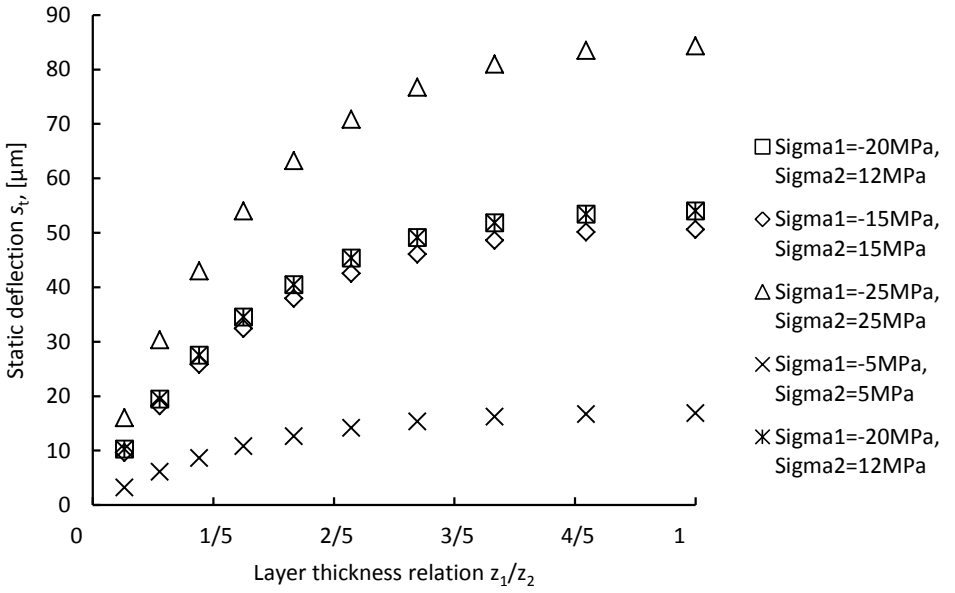

Figure 2.11: Actuator static deflection vs. layer thickness ratio

Deflections of 10 to 25 µm can be achieved at the ratios of z_1/ z_2 from 1/5 to 1/1. Higher deflections occur at higher values of internals stresses.

2.1.8.2 Pull-in voltage

The following graphs illustrate estimations of pull-in voltage U_{pi}. First, dependence of pull-in voltage on the length of the actuator L_b at constant width b = 500 µm and ratio z_1/ z_2 = 1/9 was determined (Fig. 2.12).

Apart from obvious fact that higher internal stresses result in higher pull-in voltages, it is interesting to mention that up to the length of approximately 500 µm pull-in voltage drops very quickly but at lengths above 500 µm it again begins to slightly increase. And the higher the internal stress is, the stronger is the increase in pull-in voltage. Pull-in voltage drop with increasing actuator length was described in literature [54, 55]. But to the authors best knowledge there was no investigation of the lengths above 1000 µm and the results derived in this investigation can be useful for the future designs of the beams with comparable dimensions. Furthermore, it was found that mathematically pull-in voltage does not depend on the width of the actuator.

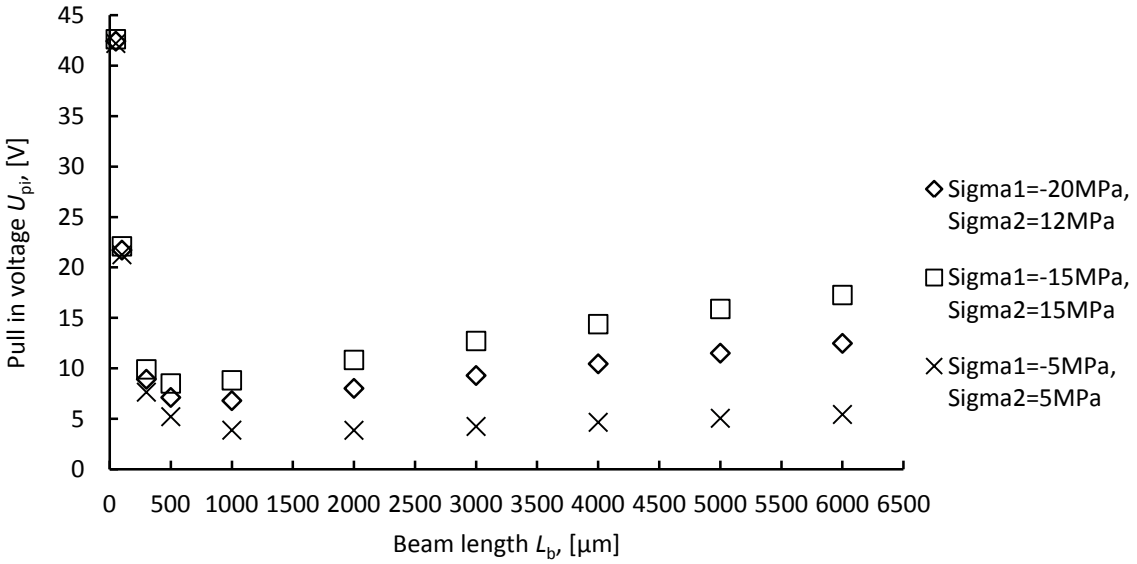

Figure 2.12: Pull-in voltage vs. actuator length

On the other hand, it was interesting to investigate the dependence of pull-in voltage on the ratio z_1/ z_2. This dependence is depicted on Figure 2.13. The result is very similar to the one for the static deflection. Again, with increasing internal stress, pull-in voltage increases. It also increases as the ratio z_1/ z_2 increases.

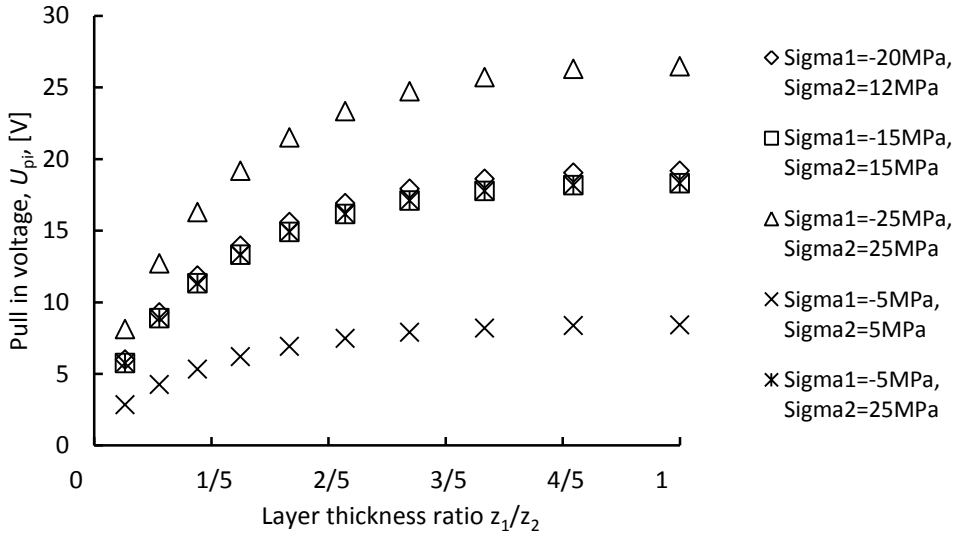

Figure 2.13: Pull-in voltage vs. layer thickness ratio. L_b = 3000 µm, b = 500 µm

Another parameter that influences pull-in voltage is the thickness of the sacrificial layer or the minimal gap between the curved beam and the isolation layer d_{sl}. Figure 2.14 illustrates this dependence.

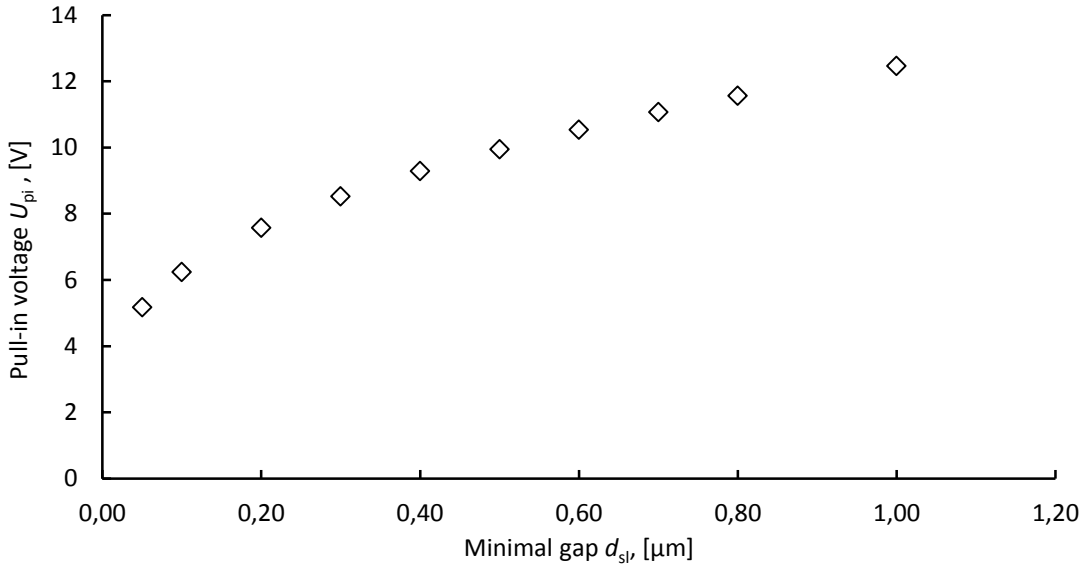

Figure 2.14: Pull-in voltage vs minimal gap. L_b = 3000 µm, b = 500 µm

At chosen design and design/process parameters, pull-in voltage is far below the specifications limit of 60 V. This fact increases the flexibility in the dimensioning during the design of the beam.

The next graphic (Fig. 2.15) can be used as an estimation tool to determine the pull-in voltage at given geometry and design parameters. Here, L_b = 3000 µm, b = 500 µm, σ_1 = -20 MPa, σ_2 = 12 MPa, z_1 = 2 µm and z_2 = 18 µm.

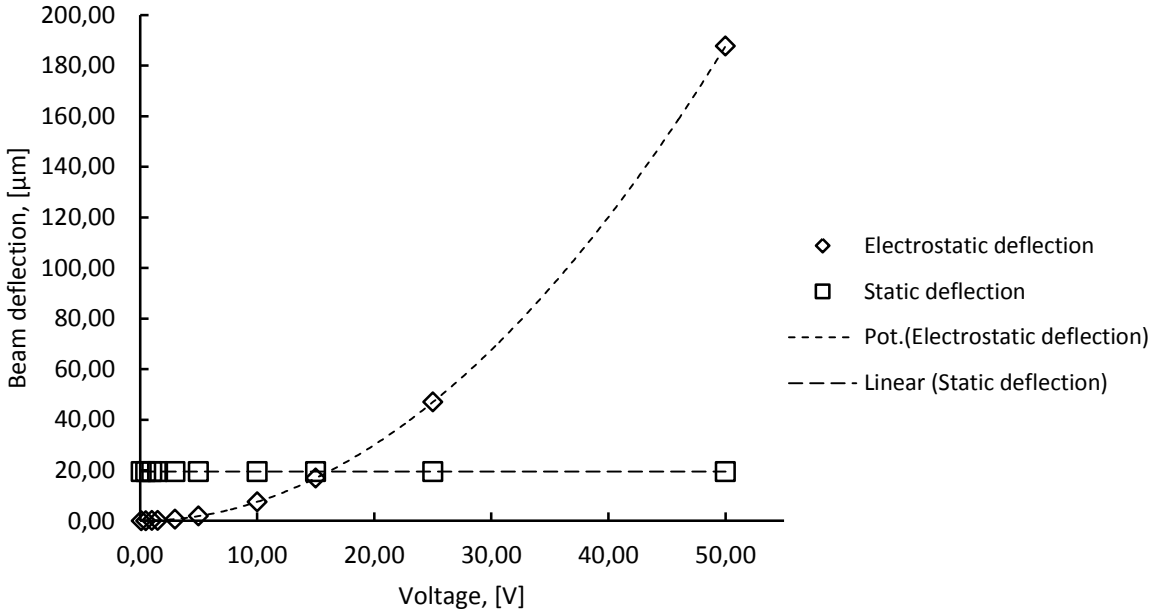

Figure 2.15: Graphical estimation of the pull-in voltage by static and electrostatic deflection

The parabolic curve depicts the deflection of the beam due to applied voltage. The horizontal line is the constant deflection of the beam due to internal stress and geometry. At the point of

intersection the beam will be completely deflected to the surface. However, as it was mentioned before, pull-in occurs at 1/3 of the complete deflection. Hence, in this example pull-in occurs at deflection of about 7 µm that corresponds to approximately 10-11 V. The calculated (Eq. 2.41) value for such a beam is 11,16 V.

2.1.8.3 Actuator' reaction time

As follows out of the Eq. 2.49 – 2.51, the actuator's reaction time t_r depends on the beam's length L_b, layer thicknesses z_1 and z_2 and constant material properties. Therefore, the reaction time was estimated as a function of length L_b and layer thickness ratio z_1/z_2 (Fig. 2.16).

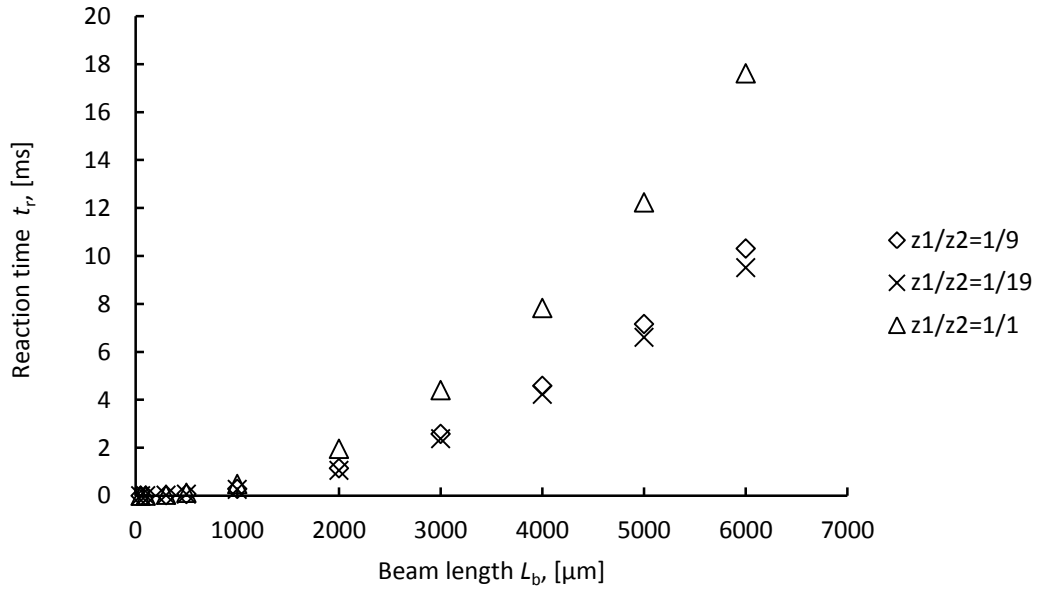

Figure 2.16: Actuators reaction time vs. beam length and layer thickness ratio

The reaction time does not depend on the beam's width *b*. Obviously, it increases with increasing beam's length. The only parameter that could decrease the reaction time and can be influenced by designer at chosen material is the ratio of the layer thicknesses. However, Fig. 2.16 demonstrates that this influence in the decrease direction is also very weak. Moreover, the change of the ratio is limited by technological reasons and the fact that higher ratio also decreases the beam's deflection (Fig. 2.11). Thus, the ratio of $z_1/z_2 = 1/9$ was finally chosen.

2.1.8.4 Actuators dimensioning summary

In correspondence with the above discussed calculations the following fifteen actuator beam design variants were proposed (Tab. 2.2)

Table 2.2: Actuator geometry design variations

Design ID	Length L_b, [µm]	Width b, [µm]	σ_1, [MPa]	σ_2, [MPa]	z_1, [µm]	z_2, [µm]
1.1	2500	850	-20	12	2	18
1.2	2500	600	-20	12	2	18
1.3	2500	500	-20	12	2	18
2.1	3000	1000	-20	12	2	18
2.2	3000	750	-20	12	2	18
2.3	3000	600	-20	12	2	18
3.1	3500	1200	-20	12	2	18
3.2	3500	900	-20	12	2	18
3.3	3500	700	-20	12	2	18
4.1	4000	1300	-20	12	2	18
4.2	4000	1000	-20	12	2	18
4.3	4000	800	-20	12	2	18
5.1	4500	1500	-20	12	2	18
5.2	4500	1100	-20	12	2	18
5.3	4500	900	-20	12	2	18

It was decided to keep the internal stresses σ_1 and σ_2 as well as the layer thicknesses z_1 and z_2 constant in order to avoid overwhelming process variations. Moreover, the calculations above showed that at chosen values of stresses and thicknesses, specification limits should not be violated. Instead, the geometry was greatly varied.

Longer beams would allow higher deflection that on the one hand would result in higher pull-in voltages, but on the other hand are necessary for microvalve operation, which will be discussed in the next subsections.

2.2 Microvalve design

In this subsection, basic fluid flow calculations regarding gas flow through microvalve are presented. This is important since microvalves are thought to be one of the main applications of the actuator being developed in this work. The aim of the calculations is to determine the geometry and dimensions of the gas flow channel and the optimal position of the actuator above the channel opening, i.e. the optimal valve lift at which the desired flow can be achieved.

2.2.1 Constitutive equations

The fluids in fluid mechanics are subdivided into compressible (gases) and incompressible (liquids) ones. In this work, only the case of compressible fluids will be discussed, as the working medium was chosen to be nitrogen (N_2) or air.

The constitutive equations can be classified as thermal and isentropic [62]. The main thermal equation for the ideal gas is

$$P = \rho R_S T \tag{2.51}$$

where

P – gas pressure
ρ – gas density
$R_S = R/M$ – specific gas constant with R – molar gas constant, and M – gas molar mass
T – temperature

Table 2.3 summarizes the basic properties and constants for air and nitrogen.

Table 2.3: Properties of N_2 and air at normal conditions

Standard conditions				
Temperature	T_0	*K*	273,15	273,15
Pressure	P_0	*Pa*	101325	101325
Properties			**N_2**	**Air**
Density	ρ_0	*kg/m³*	1,2505	1,2920
Molar mass	M	*kg/kmol*	28,016	28,98
Molar gas constant	R	*J/kmol K*	8314,472	8314,472
Specific gas constant	R_S	*J/kg K*	296,8	286,9
Isentropic coefficient	κ	-	1,40	1,40

Knowing the properties of a gas at normal conditions, it is possible to calculate the state of the gas at different condition using the following expression

$$\frac{\rho}{\rho_0} = \frac{p}{p_0}\frac{T_0}{T} \tag{2.52}$$

Consider a system of two volumes filled with the same gas. Gas in volume two has pressure p_1, temperature T_1 and density P_1, whereas the gas in volume 2 has pressure P_2, temperature T_2 and density ρ_2, and $P_1 > P_2$.

The gas flows from the volume with higher pressure in the direction of the volume with lower pressure, as it is shown in Figure 2.17.

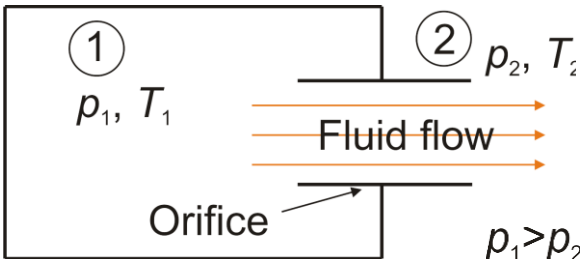

Figure 2.17: Schematic representation of the gas flow through the orifice

In case of a microvalve, the distances are very short and the speeds of the flow can reach the speed of sound. Hence, there is not enough time for the heat exchange between the gas and ambient environment, e.g. dq =0. Therefore, the first law of thermodynamics can be written as

$$0 = dU + PdV\,, \tag{2.53}$$

where

U – system internal energy
P – pressure
V - volume

and the process can be considered as adiabatic [63]. Additionally, we consider the process thermodynamically ideal (R = const, k = const) and frictionless [64].

Following the above stated, the isentropic change of the gas state from 1 to 2 (Fig. 2.17) can be described by the following isentropic equation:

$$\frac{\rho_2}{\rho_1} = \left(\frac{P_2}{P_1}\right)^{\frac{1}{\kappa}} \tag{2.54}$$

and

$$pV^{\kappa} = const \tag{2.55}$$

Finally, the interrelation between density, pressure, temperature and the speed of sound is given by

$$\frac{\rho_2}{\rho_1} = \left(\frac{P_2}{P_1}\right)^{\frac{1}{\kappa}} = \left(\frac{T_2}{T_1}\right)^{\frac{1}{\kappa-1}} = \left(\frac{c_2}{c_1}\right)^{\frac{2}{\kappa-1}} \tag{2.56}$$

Thermal and isentropic constitutive equations are indispensable for further calculations of flow rate.

2.2.2 Theoretical mass and volume flows. Ideal case.

Theoretical mass flow rate is given by [62] – [64]

$$m_{th} = A \cdot \Psi_A \cdot \sqrt{2 P_1 \rho_1}\,, \tag{2.57}$$

where

A – area of the orifice cross section
Ψ_A – outflow function.

The outflow function is defined as

$$\Psi_A = \sqrt{\frac{\kappa}{\kappa - 1}\left[\left(\frac{P_2}{P_1}\right)^{\frac{2}{\kappa}} - \left(\frac{P_2}{P_1}\right)^{\frac{\kappa-1}{\kappa}}\right]} \tag{2.58}$$

The graph in Figure 2.18 depicts the outflow function values corresponding to different pressure ratios.

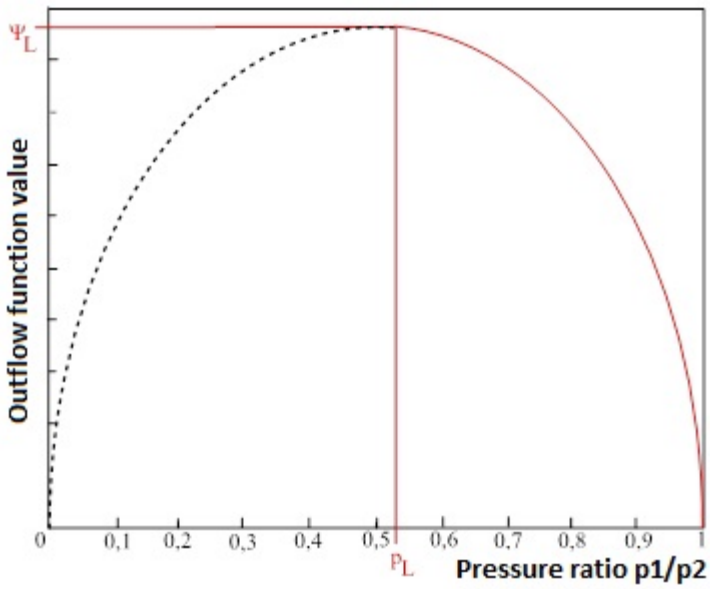

Figure 2.18: Qualitative representation of the outflow function. Dashed line shows the theoretical graph (adapted from [64])

Obviously, if the pressures in both compartments are the same ($p_1 = p_2$), the outflow function is zero and there is no mass flow at all. If, for example, the input pressure value keeps constant and the output pressure value goes down, then the value of the function will rise until it reaches its maximum:

$$\Psi_{A,\max} = \Psi_L = \left(\frac{2}{\kappa+1}\right)^{\frac{1}{k-1}} \sqrt{\frac{\kappa}{\kappa+1}} \tag{2.59}$$

The pressure ratio at which the outflow function reaches its maximum value is called a "Laval pressure ratio", or "critical pressure ratio" which is unique for each fluid:

$$P_L = \left(\frac{2}{\kappa+1}\right)^{\frac{\kappa}{\kappa-1}} \tag{2.60}$$

Although theoretically predicted, the mass flow rate will not decrease (dashed line in Figure 2.18) if the pressure rate is further decreased. It will stay constant. This is due to the effects taking place when the fluid flows with sonic speeds [62] – [64].

The corresponding volumetric flow rate is

$$V_{th} = \frac{R_S T}{p} m_{th} \tag{2.61}$$

However, these equations only describe behavior of the ideal gas under ideal conditions (no friction). In reality, flows will be influenced by geometry of the channel and orifice and by friction as well.

2.2.3 Theoretical mass and volume flows. Influence of geometry.

Figure 2.19 schematically illustrates the behavior of the gas flow passing through a straight channel of length L. Due to intensive bending at the inlet zone, the flow contracts and its real diameter at the outlet is slightly narrower than that of the orifice[12]. This in turn leads to a lower mass flow compared to a theoretical value in the ideal case. The relation between the minimal area of the narrowed flow cross section near the outlet A and the area of the orifice cross section A_{in} is called contraction coefficient:

$$\alpha = \frac{A}{A_{in}} \tag{2.62}$$

[12] This point of minimum is sometimes called *vena contracta*.

If the edges are smooth, the value of the coefficient of discharge is close to 1. With sharper edges, it becomes lower.

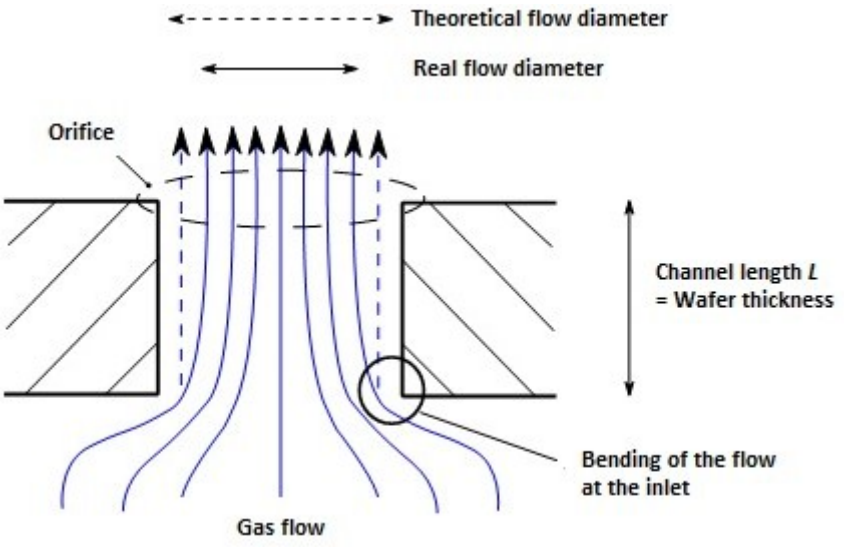

Figure 2.19: On the influence of the channel geometry on the gas flow (adapted from [62])

The second parameter arises from the fact that higher friction, caused by the flow contraction, reduces the energy and consequently the theoretical speed of the flow at the outlet $c_{2,\mathrm{th}}$. Thus, real speed c_2 is given by

$$c_2 = \varphi \cdot c_{2,th} \tag{2.63}$$

where

φ – flow speed coefficient.

Both parameters are dependent on the geometry of the inlet and outlet orifices as well as on gas. Usually, their values are determined by measurements. The empirical values for microvalves are [62], [65]

$$\varphi \approx 0{,}97..0{,}99$$
$$\alpha \approx 0{,}99..1$$

The product of the contraction coefficient and the flow speed coefficient is called a coefficient of discharge:

$$C_d = \alpha \cdot \varphi \tag{2.64}$$

Therefore, the actual mass flow rate is

$$m_{fr} = \underbrace{C_d \sqrt{\frac{2}{R_S T_1}} A_{in}}_{const.} \Psi_A p_1 \tag{2.65}$$

Now, it is necessary to define, how the geometry of the flow channel will influence the flow. In this work, a straight cylindrical channel was used (see Fig. 2.19). It was produced using a Deep Reactive Ion Etching (DRIE) technique in a silicon wafer. Therefore the geometry of a channel is a cylinder with certain diameter and length.

The pressure drop in the channel due to friction of the flow against the walls is given by

$$\Delta P = \rho \lambda \frac{L}{D_h} \frac{c^2}{2} \tag{2.66}$$

where

ρ – gas density
L – length of the channel
c – speed of the flow
D_h – hydraulic diameter
λ – coefficient of friction

For a cylindrical channel with round cross section, the hydraulic diameter D_h matches the diameter of the cross section D [62].

The coefficient of friction λ is defined by Reynolds number as

$$\lambda = \frac{0{,}2236}{\sqrt[4]{\mathrm{Re}}} \tag{2.67}$$

The Reynolds number gives a measure of the ratio of inertial forces to viscous forces and is given by

$$\mathrm{Re} = \frac{cD}{\mu} \tag{2.68}$$

where μ is kinematic gas viscosity.

For example, by given channel length L = 380 µm; area of the channel cross section A_{in} = 0,0078 mm², cross section perimeter length U = 0,3 mm and incoming pressure P_{in} = 10 bar the pressure drop is about 0,65 bar. Since it is not possible to determine the exact flow speed inside the channel it is assumed to be sonic. Therefore, the pressure drop is not more than 1%.

2.2.4 Valve lift and flow channel cross-section

As it was already described in previous subsections, curved cantilever beam performs open and close function in a microvalve. In the opened position it is hangs above the gas inlet channel at some distance, which is called a valve lift and will be defined in the following. The valve lift determines the flow rate of the valve.

In order to simplify the calculations, several approximations should be made. First, only a small area of the beam is situated above the inlet channel opening. Therefore, this section of the beam can be approximated as a flat plate (Fig. 2.20).

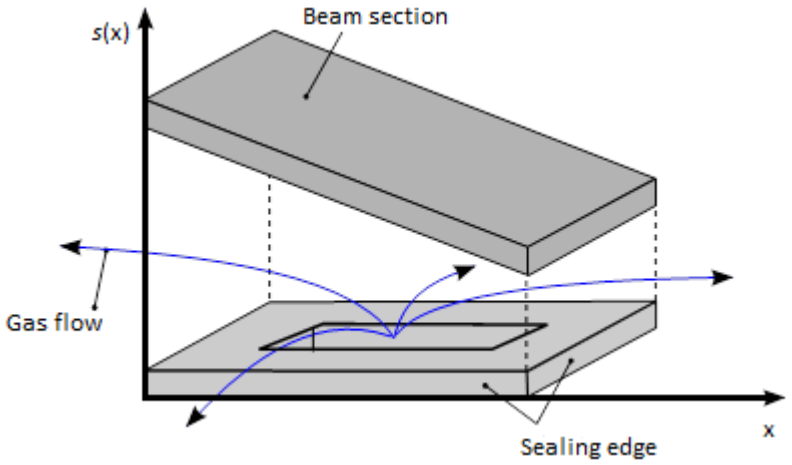

Figure 2.20: Position of the actuator above the gas inlet channel

Obviously, the beam section is positioned under a certain angle against the inlet cross section and the valve lift $s(x)$ slightly changes along the x axis. For calculations, a mean value of $s(x)$

$$s_{mean} = \frac{1}{2}(s_{\max} + s_{\min}) \tag{2.69}$$

The positions $s_{\max}$ and $s_{\min}$ are defined in Figure 2.21 and can be calculated with Eq. 2.36

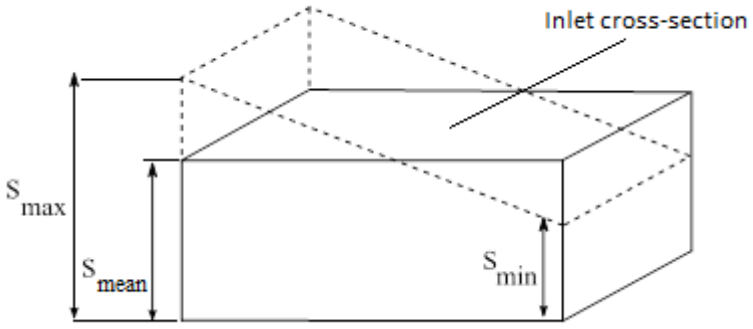

Figure 2.21: To the calculation of the s_{mean}

In the following s_{mean} will be addressed simply as s.

The flow rate depends on a flow cross-section A_{st}. The latter can be derived using the value of the cross sectional perimeter U of and the valve lift s

$$A_{st} = U \cdot s \tag{2.70}$$

In this work, the flow channel is a cylinder with a circular cross-section. Therefore,

$$U = D \cdot \pi, \tag{2.71}$$

where

D – is the diameter of the circle,

and

$$A_{in} = A_{st} = \frac{\pi \cdot D^2}{4} = U \cdot s = D \cdot \pi \cdot s \tag{2.72}$$

where

A_{in} – area of the gas incoming cross-section of the gas channel

Equation 2.72 describes the situation when incoming flow rate equals the outcoming flow rate [62] and leads to

$$s = \frac{D}{4} \tag{2.73}$$

Equation 2.73 states that valve lift must be at least 4 times smaller than the perimeter of the channel's cross-section in order to have the incoming and outcoming flow rates equal.

2.2.5 Dimensioning of the microvalve

In order to achieve the demanded specifications, a proper geometry of the gas inlet channel and the position of the actuator above the channel must be calculated. Those are defined by a mass flow rate m_{fr} (Eq. 2.65) and a valve lift s (Eq. 2.73) correspondingly. However, it is more habitual to consider gas flow in volume units of [ml/min] than in [kg/s], thus volume flow as a function of mass flow rate is represented as

$$V_{fr} = R_s \frac{T_2}{P_2} m_{fr} \cdot 6 \cdot 10^7, \tag{2.74}$$

where

R_s – specific gas constant (for N_2, R_s = 296,78 J/kg·K)
T_2 – outlet gas temperature, [K]
P_2 – outlet gas pressure, [Pa]
m_{fr} – mass flow rate, [kg/s]

Figure 2.22 represents a simplified[13] cross-sectional drawing of a microvalve chip with basic dimensions.

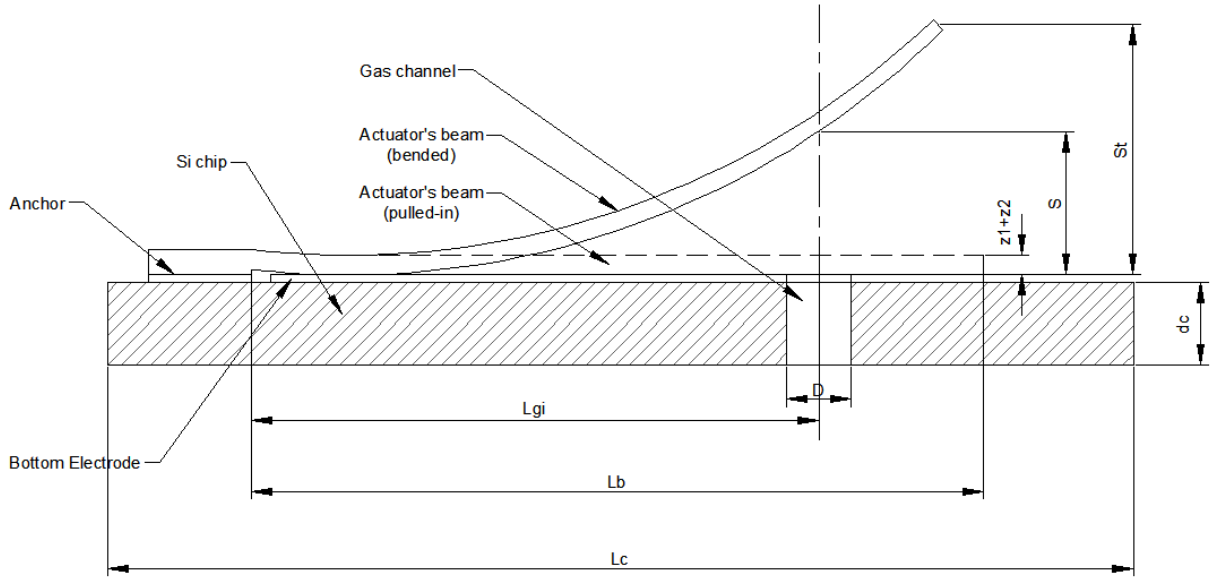

Figure 2.22: A cross-sectional view of a microvalve chip with basic dimensions (not to scale)

As it was described in pervious subsections, due to technological limitations the gas channel was chosen to be a DRIE-etched cylindrical channel with fixed length of d_c = 380 μm[14]. The length of a chip L_c = 6800 μm is constant and should be enough to accommodate all the actuator's design variants (see Table 2.2). The parameter L_{gi} defines the position of the gas channel along the actuator's beam and hence, influences the valve lift s.

2.2.5.1 Valve lift

In order to find out the minimal valve lift s through a gas channel, the diameter of the channel D should be defined. This diameter in turn will limit the gas flow rate. By convention, a gas channel diameter D and pressure ratio P_1/P_2 were put to be design parameters, i.e. they can be varied by a designer and used as a basis for the following calculations.

[13] Isolation layer and anti-stiction stand-offs are not shown. Drawing is not to scale.

[14] Corresponds to wafer thickness

Figure 2.23 represents the dependence of the volume flow rate against the inlet pressure P_1 at different channel diameters D. Output pressure P_2 = 1 bar[15].

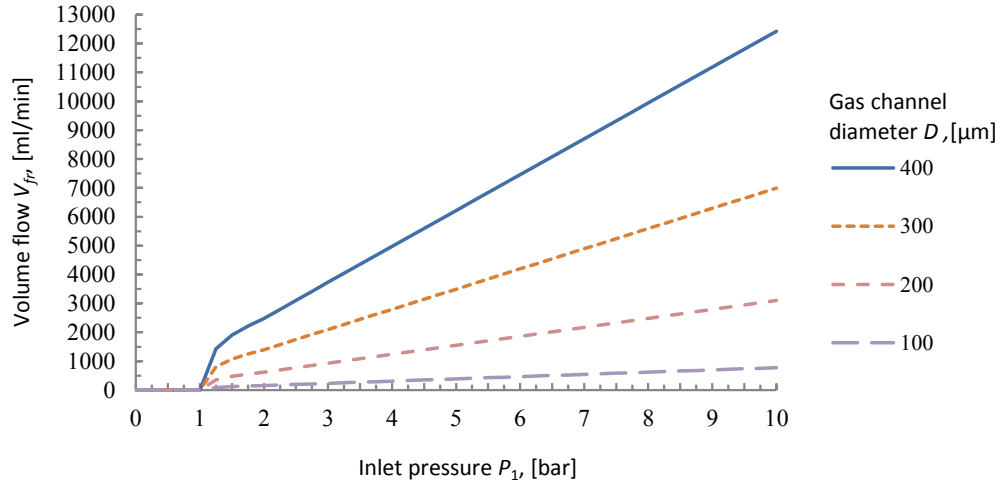

Figure 2.23: Volume flow rate as a function of inlet pressure at different channel diameters

This graph, however, does not take into consideration the valve lift s. This is done in Figure 2.24.

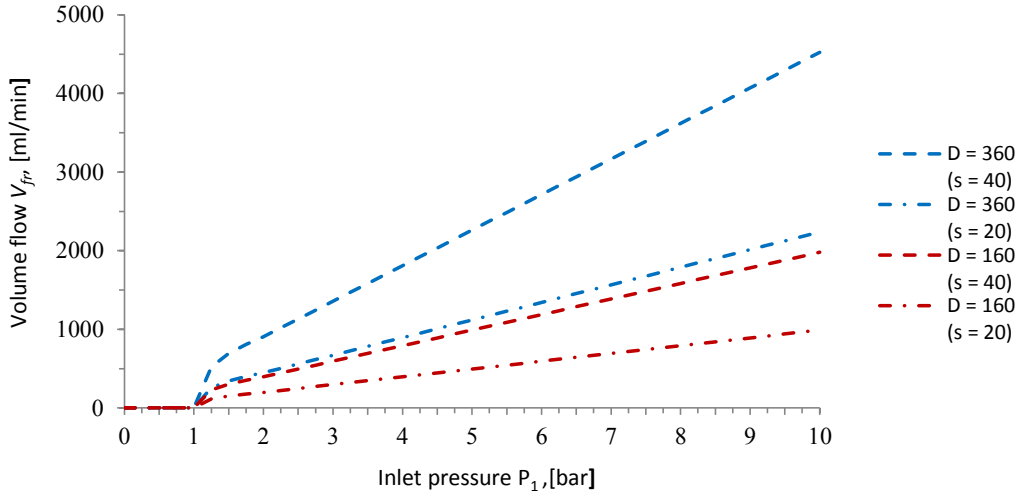

Figure 2.24: Volume flow as a function of inlet pressure at different valve lifts

[15] Atmospheric pressure. On graphs, bars rather than Pascals are used to ease the perception

As follows from the graph, larger diameters and valve lifts result in higher volumetric flows at a given inlet pressure. Additionally, larger diameters require higher values of the valve lifts. Lager valve lifts in turn, would result in higher pull-in voltages and larger gas channel diameters would increase the risk of leakage. To avoid the latter, the width of the beam should be increased, which is an unwanted change in the design. Thus, the valve lift *s* was chosen to lie in the range of < 20 µm at the length L_{gi} (see Fig. 2.22).

2.2.6 Design check

In order to check the design, a simple method was chosen. In the closed state, the actuator of any design proposed (see Table 2.2) must be able to withstand an inlet gas pressure up to 8-9 bar.

There are three main forces acting on the beam as it is in the pulled-in position:

- F_{el} – electrostatic force between the beam and bottom electrode.
- F_{pn} – pneumatic force of gas flow
- F_{to} – tear-off force due to internal stress gradient

Figure 2.25 schematically illustrates this concept.

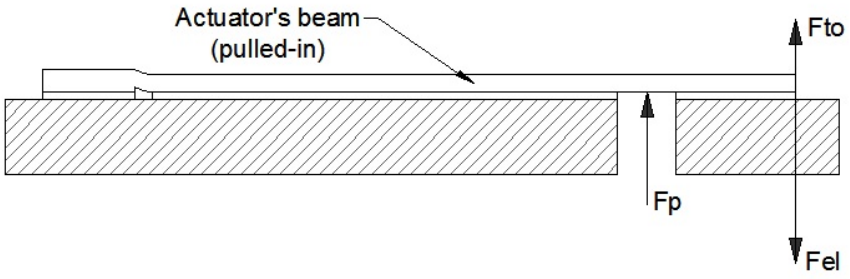

Figure 2.25: Forces acting on the actuator's beam in the pulled-in state

The force F_{el} keeps the actuator pulled in, while the forces F_{to} and F_p work against pull-in state.In order to keep the actuator stably closed, the following condition must be fulfilled

$$F_{el} > F_p + F_{to} \tag{2.75}$$

In a closed state, the actuator and bottom electrode can be treated as a parallel plate capacitor. Therefore, F_{el} can be calculated using Equation 2.12.

Pneumatic force of a gas pressure F_p can be calculated as

$$F_p = (P_1 - P_2) \cdot A_{in}, \tag{2.76}$$

where

P_1 – inlet gas pressure (here P1 = 9 bar)
P_2 – outlet gas pressure (here P2 = 1 bar)
A_{in} – cross-sectional area of a gas inlet channel

Gas inlet channel is a cylinder with circular cross-section of a diameter D. Thus,

$$A_{in} = \pi \frac{D^2}{4} \tag{2.77}$$

The tear-off force F_{to} is defined as [51]

$$F_{to} = ks_t = 3\frac{c_R}{L_b^3} s_t \tag{2.78}$$

Now, it is possible to estimate the influence of all the forces and to check if the actuator beam will stay closed at given geometries and conditions. The geometrical parameters were taken from Table 2.2. The diameter D was chosen to lie between 100 and 300 µm. The pull-in voltage U_{pi} = 12 V.

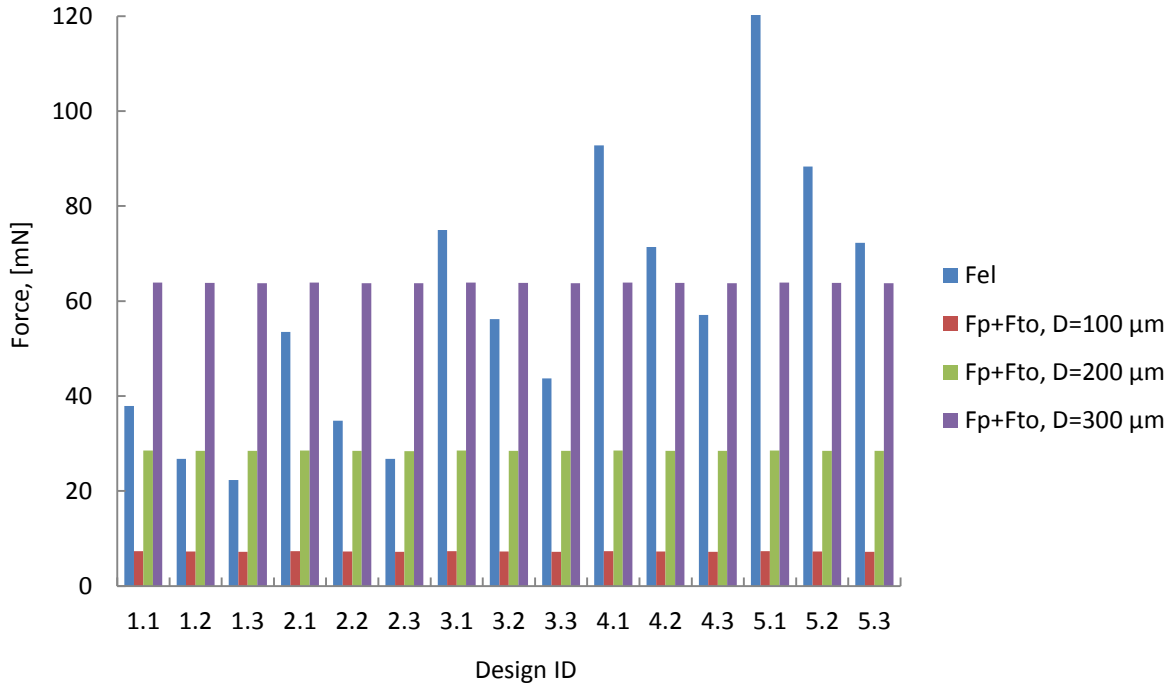

Figure 2.26: Comparison of forces acting on the actuator's beam in a pulled-in state (U_{pi} = 12 V)

Figure 2.26 shows that though as previously determined larger diameters return higher flows, they also lead to instability of the actuators state. Therefore, for the first production and characterization a minimal diameter of 100 µm was chosen.

2.3 Microactuator design summary

In the subsections 2.1 and 2.2, the main design parameters of the actuator and microvalve were considered and estimated. Fifteen design variants of the actuator were proposed. Table 2.4 summarizes the calculated values and the design variants to give an overview of the expected system performance.

Table 2.4: Summary of the calculated parameters for different actuator design variants

Design ID	St. defl. s_t at L_b, [µm]	Valve lift s at L_{gi}, [µm]	Pull-in voltage U_{pi}, [V]	Min. stand-off height h_b, [nm]	Reaction time t_r, [ms]	Inlet diameter D, [µm]	Flow rate V_{fr}, [ml/min]
1.1	13	6	8,4	200	1,6	100	31
1.2	13	6	8,4	200	1,6	100	31
1.3	13	6	8,4	200	1,6	100	31
2.1	19	9	9,3	200	2,4	100	46
2.2	19	9	9,3	200	2,4	100	46
2.3	19	9	9,3	200	2,4	100	46
3.1	26	12	9,8	200	3,0	100	62
3.2	26	12	9,8	200	3,0	100	62
3.3	26	12	9,8	200	3,0	100	62
4.1	35	15	10,4	200	4,3	100	77
4.2	35	15	10,4	200	4,3	100	77
4.3	35	15	10,4	200	4,3	100	77
5.1	44	19	11,1	200	5,1	100	98
5.2	44	19	11,1	200	5,1	100	98
5.3	44	19	11,1	200	5,1	100	98

For a production of the systems designed in this chapter, a set of photolithography masks was created. The drawings of the masks can be found in Appendix I.

3 Technology and fabrication

In this chapter, the aspects of technology and fabrication of the microactuator and its integration into simple prototype microvalve will be discussed. The chapter begins with an introduction subsection, in which the basic direction of the work on the technology as well as the main achieved results will be discussed. The following subsections will be dedicated to the detailed review of each of the topic.

3.1 Introduction

The following subsections will describe in detail experimental activities aimed on the development of the technological process for the production of the microactuator designed in the Chapter 2.

The entire process of the development of the technological process done in this work can be subdivided in several main phases. They include

I. investigation of the actuators producibility by means of electroplating
II. choice of substrate material
III. fabrication of a passive actuator (no bottom electrode)
IV. fabrication of an active actuator (with bottom electrode and contacts)
V. process development for integration of the actuator into a microvalve.

During phase I, it was necessary to define the critical parameters of the galvanic process of Ni deposition in order to find out, which of these parameters have the most significant influence on the internal stress gradient. Although it was earlier determined, that the most critical parameter would be current density [51], a set of new measurements was conducted, since the process appeared to be very sensitive to the variation of such factors as electrolyte pH value and temperature. Agitation of the electrolyte showed influence on the uniformity of the metal deposition over the wafer surface.

Phase II was dedicated to the choice of the substrate material. At first sight, it is obvious to simply take a standard Si substrate, as it has proven characteristics and is a standard both in MEMS R&D and in industry. However, a question of an alternative substrate introduction was considered. First, two variants were proposed: Al_2O_3 ceramic substrates and Flame Retardant Class 4 (FR-4) glass reinforced epoxy laminate being used for example for printed circuit boards (PCB) production. As it was thought, the use of such substrates could bring process simplification and consequently cost reduction. Furthermore, investigation of their integribility into standard production steps, especially electroplating, was of technological interest. Finally, for the reasons described in the dedicated subsections, it was decided to work with 4-inch Si substrates.

Phase III included several runs of subsequent surface micromachining steps focused on electroplating and wet etching of sacrificial layers in order to check the reproducibility of the

deposition process and correspondence of the actuators final geometry to the theoretical expectations.

During Phase IV, bottom electrodes were added in order to make the actuator functional.

In Phase V, a through silicon microchannel was introduced underneath the actuator structure, turning the chip into a microvalve element where the actuator can serve as an open-close element.

Microfabrication was performed in the clean-room of the Institute for Microsensors, actuators and systems (IMSAS) of the University of Bremen. The clean room is of class ISO6 (Class 1000 according to the US FED STD 209E).

3.2 Characterization of Ni electroplating process

Ni electroplating is the central part of the whole actuator fabrication process. Two subsequently plated layers of Ni form a microactuator beam. The process defines the beams geometry and its mechanical properties. The main challenge was to find out which process parameters influence the final characteristics at most.

As it was shown in earlier works dedicated to Ni electroplating and held out at the IMSAS [51], the most significant role belongs to the following parameters:

- current density
- electrolyte pH value
- electrolyte temperature

The shape of current, or voltage signal proved to be of little importance for the process [51].

The current density influences the internal stress of the layer. Hence, one had to find out the interrelation between these two parameters. Although this was also already investigated in the above mentioned works, the importance of the parameter claims that it must be additionally controlled.

To complete this task, a set of 25 4-inch 525 µm thick Si wafers were taken. Each wafer was wet oxidized with 500 nm of thermal SiO_2. Then, a plating base of 15 nm of chromium and 80 nm of gold was sputtered on the whole top surface of each wafer. After that, the wafers were ready for the electroplating of two Ni layers.

The set of 20 wafers was separated in two main groups. Group 1 included wafers from 1 to 12. This group was electroplated with Ni layer of thicknesses from approx. 2,4 µm to 3,0 µm.. Inside this group, the wafers were additionally subdivided into 4 subgroups of 3 wafers. Each subgroup was electroplated with different current density. Electrolyte used was a commercially available standard nickel sulfamate solution with pH of 3.5, which was controlled manually for every wafer. Process temperature was 52° C. Agitation of the electrolyte was involved. Table 3.1 illustrates the experimental setup.

Table 3.1: Ni layer stress measurement order. Wafers 1 to 12

Wafer ID	Layer material	Ni layer thickness, [µm]	Current density, [mA/cm^2]
1	Ni	2,69	6
2	Ni	2,89	6
3	Ni	2,87	6
4	Ni	2,91	11
5	Ni	3,03	11
6	Ni	2,83	11
7	Ni	2,83	17
8	Ni	2,73	17
9	Ni	2,80	17
10	Ni	2,39	25
11	Ni	2,72	25
12	Ni	2,75	25

The second group of wafers (wafers from 13 to 20) were electroplated with Ni layer of thicknesses from 5,6 µm to 6,1 µm using the same electrolyte under the same pH and temperature conditions with agitation. As in previous setup, wafers were additionally subdivided into 4 subgroups of 2 wafers. Again, each subgroup was electroplated with different current density. The experimental setup is shown in Table 3.2.

Table 3.2: Ni layer stress measurement order. Wafers 13 to 20

Wafer ID	Layer material	Ni layer thickness, [µm]	Current density, [mA/cm^2]
13	Ni	6,08	6
14	Ni	6,10	6
15	Ni	5,80	11
16	Ni	5,78	11
17	Ni	5,72	17
18	Ni	5,64	17
19	Ni	5,47	25
20	Ni	5,55	25

The measurements of the stress were held out with the stress measurement device “Eichhorn & Hausmann” MX-203 similar to the one shown in Figure 3.1.

Figure 3.1: Wafer geometry gauge Eichhorn & Hausmann MX-203 [66]

The device is capable of measuring one wafer per measurement run. The measurement run takes approximately 5 seconds. The wafer is normally measured at five points: left, right, top, bottom, and center. The whole measurement process is programmed and controlled by a PC with dedicated software. The measurement data are stored on the hard disc of the PC.

The graphs in Figure 3.2 and 3.3 show strong dependence of stress on current density for both thicknesses. Using these data, it was possible to adjust correct plating parameters to achieve the desired beam bending. The plating of the bottom and top Ni layers was found to be stable under the following conditions:

Layer 1 (bottom)

Temperature: T = 52 °C
Electrolyte pH: 3,2
Current density: 17 mA/cm^2
Stress: ≈ -20 MPa
Layer thickness: $d_1 \approx 2$ µm

Layer 2 (top)

Temperature: T = 52 °C
Elektrolyte pH: 3,2
Current density: 10 mA/cm^2
Stress: ≈ 12 MPa
Layer thickness: $d_2 \approx 18$ µm

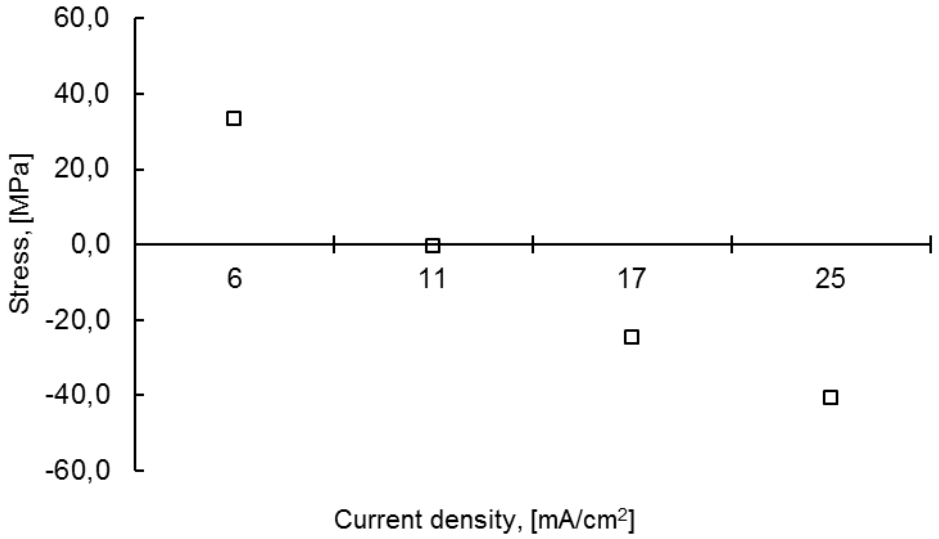

Figure 3.2: Ni layer stress vs. current density at layer thickness from 2.4 to 3 μm

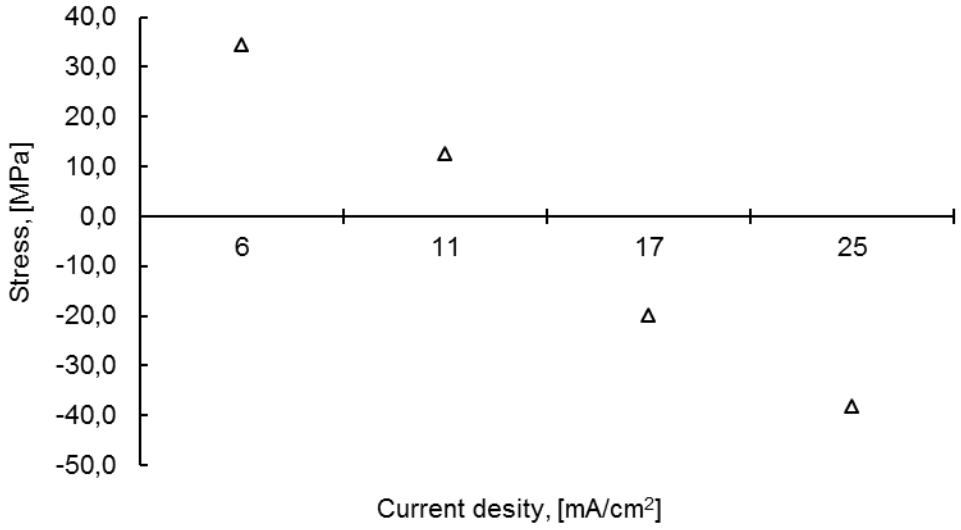

Figure 3.3: Ni layer stress vs. current density at layer thickness from 5.5 to 6 μm

These parameters had been later involved in the final technological flow.

3.3 Choice of substrate material

Three substrate materials were initially proposed:

- conventional silicon substrate,
- Al_2O_3 ceramic (alumina) substrate, and

- Flame Retardant Class 4 (FR-4) glass reinforced epoxy laminate substrate.

The two latter ones could have possible technological advance, since on the one hand, they are capable of being preprocessed. For example, electrical contacts and gas channels could be produced before actuator electroplating. On the other hand, these materials are isolators. Hence, no oxidation layers need to be deposited, as in case of silicon.

There was also a clear technological interest, if it was possible to integrate such substrates into a conventional electroplating, and to carry on other standard MEMS processes on them without too many changes.

On the other hand, very often, not only surface but also bulk micromachining must be performed somewhere in the technological flow. Such treatment is not usual for ceramics and FR-4. This could lead to complications and make the overall process very expensive. Moreover, unless high production volumes are provided, it is hard to find a supplier of such preprocessed substrates who could provide them for a reasonable price. In addition to that, a substrate must have a shape of a conventional 4-inch wafer, which is also not common for FR-4, but turned out to be possible for ceramics.

For these reasons, FR-4 was excluded from this work and remains open for future investigations. Alumina was investigated as described in the next subsection. Finally, conventional silicon substrates were chosen, due to their robustness, technological flexibility and availability in comparison to the others.

3.3.1 Al_2O_3 substrate study

3.3.1.1 Alumina: basic information

Aluminum oxide Al_2O_3 or alumina is the most important, widely used and cost effective oxide ceramic material. The material possesses strong ionic bonding, which determines its material properties:

- high mechanical strength (flexural strength) and hardness;
- high wear resistance;
- high resistance to chemical attacks of strong acids and alkali even at high temperatures;
- high stiffness;
- excellent insulating properties;
- low coefficient of thermal expansion;
- good fracture toughness;
- good thermal conductivity;
- good biocompatibility.

Aluminum ceramics parts are manufactured by the following technologies: uniaxial (die) pressing, isostatic pressing, injection molding, extrusion and slip casting. Aluminum ceramics are widely used in electronics and electrical engineering, metallurgical processes, chemical technologies, medical technologies, mechanical engineering, military equipment.

Aluminum ceramics are used for manufacturing insulators, capacitors, resistors, furnace tubes, sealing refractory parts, foundry shapes, wear pads, thermocouple protection tubes, cutting tools and polishing/grinding powders, ballistic armor, laboratory equipment, bio-ceramic parts for orthopedic and dental surgery, bearings and of course substrates.

The technical alumina ceramics contain at least 80% of aluminum oxide (KER 706)**.** There are also alumina types KER 708 (90% - 99% of Al_2O_3), and KER 710 (>99% of Al_2O_3). The rest of the material is usually SiO_2. In this work, 4-inch wafer shaped alumina substrates with purities of 91%, 96% and 99,6% were processed.

Wet and dry processing of alumina is possible. Dry etching can only be performed using very special and expensive techniques, such as [67]

- **Laser etching with CF_4**
  Gas: CF_4
  Energy source: XeCl-Laser, $\lambda = 308$ nm

- **RIE in a mixture of Cl_2 and Ar**
  Gas mixture: 71 Vol. % Ar; 29 Vol. % Cl_2
  Plasma conditions: 0.933 Pa, -750 V bias
  Energy source: XeCl-Laser, $\lambda = 308$ nm

- **RIE in CH_2F_2 or CH_3F**
  Gas: either 100% CH_2F_2 or CH_3F
  Plasma condition: 0.027 Pa
  Ion energy: 0.8 kV
  Ion flow density: 0.6 mA/cm^2 (angle of incidence 30°)

At the time of this project, these processes were not available at the IMSAS on the one hand, due to the lack of equipment. On the other hand, due to the fact that some important parts of the RIE tool are also made of ceramic materials and could be damaged during high power processing. Processing with lower power would not return reasonable etching rates.

Hence, the main focus was concentrated on the wet etching of the alumina. As it has been already stated above, the material has high resistance to such a processing. Therefore there is no much information on how to do it. Only several literature sources were found [68]. In these sources, however, very special techniques and tools were used to achieve the results. Nevertheless, it is known that alumina can be etched by phosphoric acid (H_3PO_4) and nitric acid (HNO_3) [68]. It is also known that the resistivity to chemical reaction is directly proportional to the purity and inversely proportional to the porosity of the alumina. The goal of this project part was to find out if it would be possible to etch the alumina using simpler wet etching approaches.

3.3.1.2 Wet etching experiments

Table 3.3 sums up the experimental setups used in this work to determine the etchibility of the alumina substrates in wet etchants.

Table 3.3: Wet etching experimental setups

Take No.	Substrate				Etchant		Time, h	Mask, Yes/No	Mask material	Result
	Supplier	Type	Purity, %	Surface roughness Ra, [µm]	Type	Temp., °C				
1.1	CeramTec	Rubalit 708S	96	0.1	PWS	35	3.5	No	-	+
1.2	CeramTec	Rubalit 708S	96	0.1	H_3PO_4 (85%)	55	3.5	No	-	+
2.1	N.D.	KER710	99.6	1	PWS	35	4	Yes	Cr	-
2.2	N.D.	KER710	99.6	1	H_3PO_4 (85%)	55	4	Yes	Cr	-
3.1	CeramTec	Rubalit 710	99.6	0.1	PWS	35	4	Yes	Cr	-
3.2	CeramTec	Rubalit 710	99.6	0.1	H_3PO_4 (85%)	55	4	Yes	Cr	-
4.1	CeramTec	Rubalit 710	99.6	0.1	PWS	65	6	Yes	Cr	-
4.2	CeramTec	Rubalit 710	99.6	0.1	H_3PO_4 (85%)	85	6	Yes	Cr	-
5.1	CoorsTek	KER708	91	>1	PWS	35	5	Yes	Photoresist TI35	-
5.2	CoorsTek	KER708	91	>1	H_3PO_4 (85%)	55	5	Yes	Photoresist TI35	-

An 85%-solution of phosphoric acid (H_3PO_4) and the PWS-solution[16] were used. The table also shows the result of the experiment. A "+"-sign in the right most column means that etching was observed. In the following, more detailed description of the experiments will be given.

Take 1

The first two substrates were rectangular pieces of ceramic type 708 with purity of 96%. Before etching, it was cleaned in peroxymonosulfuric acid[17]. Due to nonstandard shape of the substrate, no mask was used in this take. Hence, in order to find out if any etching took place or not, a set of 7 preliminary contact thickness measurements was done. After the etching, the thickness was measured again on the same positions. This is illustrated in Figure 3.4. Process parameters can be found in Table 1.3.

[16] PWS (Ger.: Phosphorsäure – Wasser - Salpetersäure) – a mixture of 80% of H_3PO_4, 16% of H_2O, and 4% of HNO_3.

[17] Also known as Caro's acid.

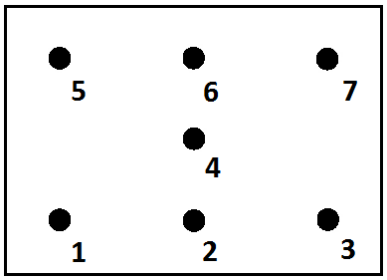

Figure 3.4: Contact thickness measurement points on the substrate.

For each point, five contact thickness measurements in a row were taken. The measurement results for both PWS and H_3PO_4 etching tests are represented on the graphs in Figures 3.5 and 3.6 respectively. In these graphs, the mean values and standard deviations σ are represented.

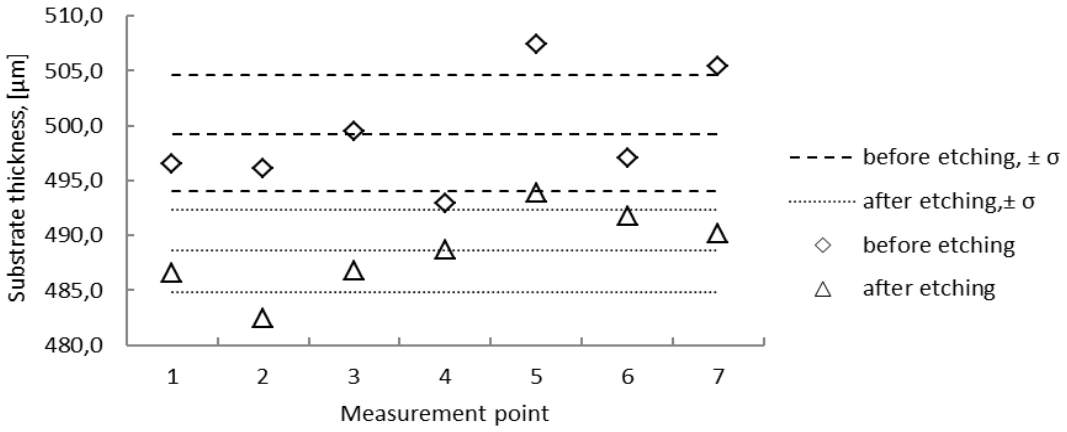

Figure 3.5: Graphical representation of the etching results in PWS.

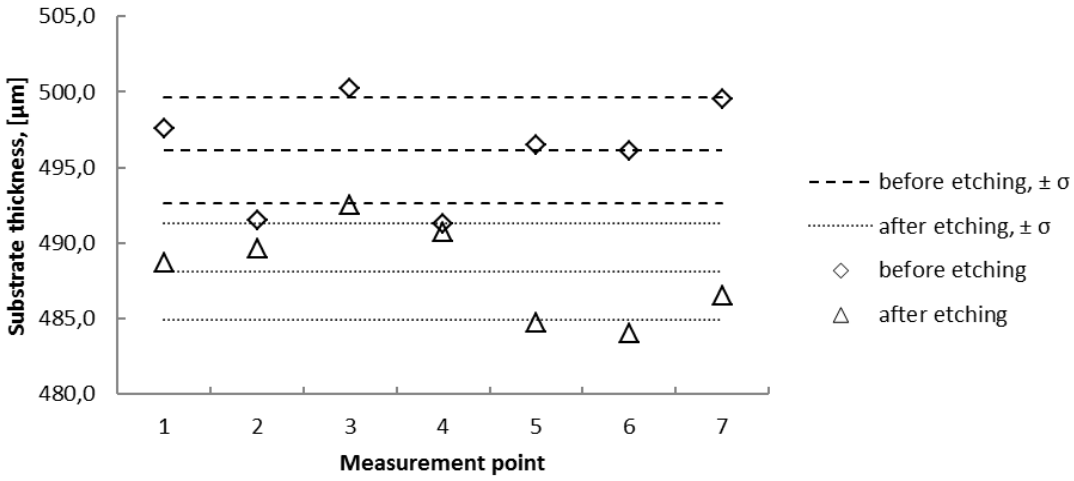

Figure 3.6: Graphical representation of the etching results in H_3PO_4.

Both graphs show that etching of the alumina of the type 708 is possible both with PWS and 85% solution of H_3PO_4. The etch rates were determined to be around 40 nm/min in H3PO4, and around 50 nm/min in PWS. PWS seems to etch a little faster on the first sight. Thought, taking into consideration the standard deviation of about 30% it is hard to say, which of two is really faster. It was also noted, that in both cases, etching in the center of the substrates (point 4) is much slower than on the edges. Possible explanation could be that the contact surface between the substrate and the chemical is larger on the edges, i.e. solution can attack not only from the top or the bottom, but also aside. Furthermore, some admixtures or contamination could occur in this area. Although, this is unlikely that contamination occurred exactly on the same position of several substrates.

After relatively successful etching without masking, further takes with patterned chromium or photoresist layers as masks were planned and executed.

Take 2

The second set of substrates of type KER710 with higher purity of 99.6% but lower surface roughness of Ra = 1 µm was also etched in PWS and 85% solution of H_3PO_4. Taking into consideration higher purity of the material, etching time was increased up to 4 hours for both solutions. The substrates had the shape of a 4 inch[18] square wafer. Thus, it was possible to process them, though with some restriction, with common tooling.

First, both substrates were cleaned in peroxymonosulfuric acid. A 50 nm thick chromium layer was then sputtered on the top side of the substrate. After that, a spin coating of a 2 µm thick positive photoresist and common exposure and development steps were done[19]. Two masks with different test structures were used for this and all the following takes. Then, chromium was wet etched in the commercially available "Chrom Etch 3144" solution by Honeywell. The remaining photoresist was stripped away with acetone and isopropanol. The back side of the substrates was then completely sputtered with 100 nm thick layer of chromium in order to avoid alumina etching elsewhere except of the opened areas on the front side.

Figure 3.7 shows two alumina substrates covered with patterned chromium layer.

[18] Side length

[19] Since it was only a single layer process, no precision mask alignment was needed. Later on, when a multilayer process was introduced, alignment problems due to surface roughness and scattering came into play. This issue will be described in a dedicated section below.

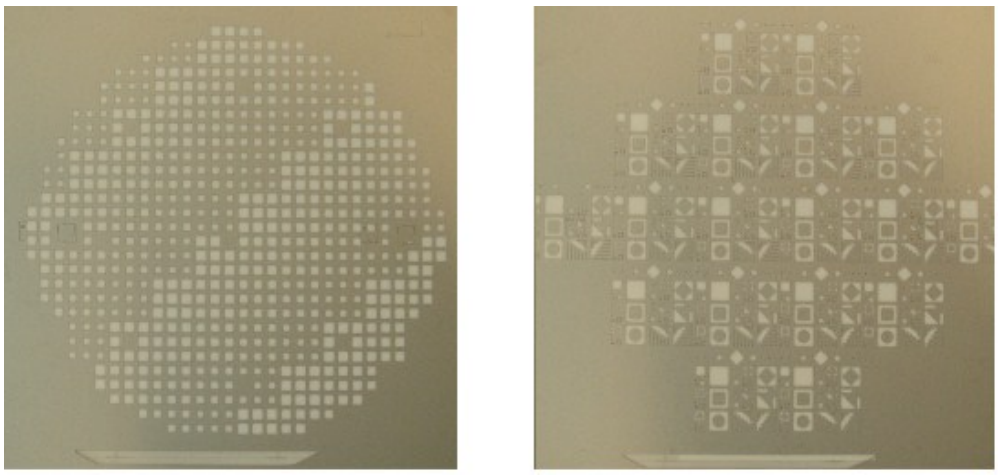

Figure 3.7: KER710 Substrates covered with patterned chromium layer:
mask variant 1 (left), mask variant 2 (right)

A step measurement on the contact profilometer Alpha-Step was done. But it did not show return any step between alumina surface and chromium surface due to very high surface roughness of alumina. It was expected, that after wet etching the step will be seen.

Finally, wet etching of the substrate 1 in PWS and substrate 2 in H_3PO_4 was performed and contact measurement of both substrates was done again. Unfortunately, as before, no difference was detected. Either no etching at all took place, or the sensitivity of the profilometer is too low to detect it compared to surface roughness.

It was expected that alumina with higher purity would possess higher durability against wet etching. Still, it was expected to find at least slight material removal. Therefore, it was decided to use the substrates of the same purity, but with finer surface.

Take 3

In this take, all the processes and parameters of the previous take were used. The only difference was in the substrates. This time, the substrates with surface roughness of Ra = 0.1 µm were taken. These substrates of type 710 provided by the company CeramTec had the shape of a common 4 inch silicon wafer. Thus, it was possible to process them with common tools without significant issues. Before wet etching, both substrates were broken into 4 parts in order to be able to process 1 wafer at least 4 times with different conditions, if needed (Fig. 3.8) Parts 1 and 2 were utilized in take 3, whereas parts 3 and 4 were postponed for take 4.

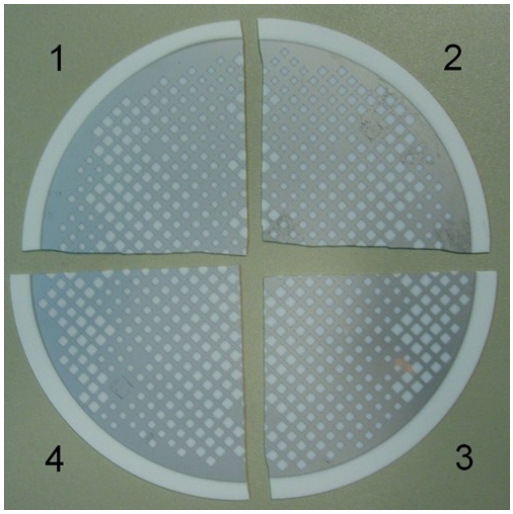

Figure 3.8: Broken CeramTec Rubalit 710 substrate covered with chromium mask

Unfortunately, after 4 hours of wet etching neither substrate 1, which was etched in PWS, nor substrate 2, which was etched in H_3PO_4, showed traces of the material removal.

Take 4

In this take, the same material as in previous take was utilized. The etching parameters were changed. First of all, temperature of both etchants was raised to 65°C for PWS and 85°C for H_3PO_4. Etching time was increased up to 6 hours for both runs.

After the runs, the step height was again measured with alpha-step contact profilometer. As before, no material removal was observed.

Take 5

In the final take, a material with lower purity was utilized. It was two alumina substrates of type 708with purity of 91% supplied by the company CoorsTek. This time, instead of chromium, a 3 μm thick positive photoresist TI35 was used as the mask for wet etching in order to reduce the costs of the experiment. This photoresist possesses a very high resistivity against wet etching solutions and high temperatures. Before coating with resist, an adhesion promoter was deposited on the surface of the substrates. The resist was then exposed and developed using standard procedures. Figure 3.9 shows the substrate covered with patterned resist mask.

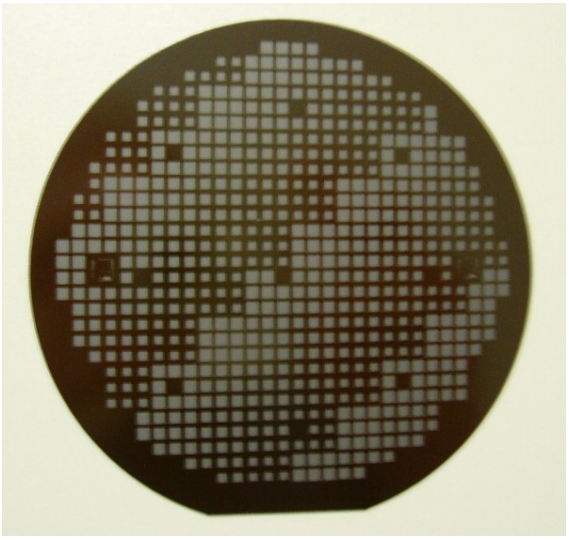

Figure 3.9: Alumina KER 708 91% covered with TI35 photoresist mask

The etching was performed in PWS and in 85% solution of H_3PO_4.

As in previous takes, contact measurements of the step height on different positions using alpha-step tool were performed both before and after the etching. No material removal was observed.

3.3.1.3 Electroplating of Ni onto an Al_2O_3 substrate

The point of the following experiment was to investigate a principal possibility to produce nickel actuator on a ceramic substrate by means of electroplating. This could ensure the utilization of such wafers in the processes where no bulk micromachining would be foreseen. In order to do it, an already existing at the moment electroplating process, described in literature before [51] was used. Since it was developed at the IMSAS, all the masks could also be directly used.

Five 4-inch 500 µm thick polished down to Ra = 0.1 µm alumina wafers of type Rubalit KER 710 supplied by CeramTec were taken for the experiment.

The production process began with conventional cleaning in the peroxymonosulfuric acid. Since alumina is an insulator, no substrate thermal oxidation was needed. After cleaning, a seed layer of 15 nm of Cr and 80 nm of Au was sputtered over the surface of the substrate followed by sputtering of 500 nm of Cu. Then, the first lithography step defining the opening in Cu for an anchor of the actuator was performed. First, wafers were heated on a hot plate at 120°C for 2 min. in order to remove possible moisture. Then, adhesive agent TI-Prime was spin-coated. Thereupon, the wafers were heated on a hot plate at 100°C for 2 min. After that, a positive 1,8 µm thick photoresist AZ®1518 was semiautomatically spin-coated over the surface of the wafer, followed by a softbake step on a hot-plate at 120°C for 2 min. The contact vacuum 2.2 sec. long exposure with UV-light was performed on a Süss MA6 mask aligner. At this point, no precision alignment was needed. After the development step, the resist was additionally hardbaked on a hot-plate for 2 min. at 100°C. After that, a descumming in oxygen plasma was done. This step ensures that no photoresist residuals are left in the developed zones. Cu was then wet etched in

the resist openings using a mixture of Alketch I and Alketch II 2:1 solution. After optical inspection under the microscope, the photoresist was stripped of with acetone and isopropanol.

Then, a second photolithography step defining the actuator geometry was performed. This time, a 20 μm thick positive photoresist AZ®4562 was spin coated in 2 steps. First, the wafers were heated on a hot plate at 120°C for 2 min. in order to remove possible moisture. Then, adhesive agent TI-Prime was spin-coated and the wafers were again heated on a hot plate at 100°C for 2 min. After that the first layer was spin-coated and the resist was hardbaked in oven for 5 min. at 90°C. The wafers were left at room temperature for 15 min. for cooling. Directly after that, the second coating was performed and the wafers were left in oven for 60 min at 90°C. Before the exposure the wafers were kept in a horizontal position at room temperature for 24 hours. The contact vacuum 60 sec. long exposure with UV-light was performed on a Süss MA6 mask aligner. This time, the actuator mask had to be precisely aligned against the alignment markings, defined on the surface of the wafer during the first lithography step. It turned out to be a problem, because these markings were hard to be seen on the surface of the ceramic substrate, or could be seen at all neither under the microscope nor at the monitor of the mask aligner. The issue, however, appeared only in the photolithography clean room under the yellow lighting. In the measurements clean room under normal day light the markings could be seen much better. The reason of that phenomenon remained unclear. However, a supposition was made, that surface roughness of Ra = 0.1 μm causes strong scattering and thus, is still not enough for MEMS production. Only two of five wafers could be aligned more or less precise in the way that the following sacrificial Cu layer etching could be made possible. No reliable repeatability could be guaranteed.

Nevertheless, the two successfully aligned wafers were further processed. After the development in AZ400K developer and descumming in oxygen plasma, the electroplating of two Ni layers was performed in the nickel sulfamate electrolyte with pH=3.5 under the conditions described above (see Section 1.2). The electroplating showed no differences with conventional plating on silicon substrates.

After the electroplating the wafers were rinsed in DI-water and photoresist was stripped off with acetone and isopropanol.

Figure 3.10: The released actuators on the alumina substrate

The etching of the sacrificial 500 nm thick Cu layer was done in an Alketch I+II 2:1 solution for 24 hours. The actuator beams were successfully released (Fig. 3.10)

3.3.2 Substrate choice: conclusion

Two alternatives to a conventional silicon substrate were chosen:

- Al_2O_3 ceramic (alumina) substrate, and
- Flame Retardant Class 4 (FR-4) glass reinforced epoxy laminate substrate.

The latter one was excluded from the experimental work due to difficulties with its small volume commercial availability in a 4 inch wafer shape.

Different types of Al_2O_3 were investigated. First, wet etching experiments were performed in an attempt to find out a simple and cost effective ceramic wet etching method as well as the most suitable ceramic type. In spite of some successful runs with the substrates of type 708 in the first take, the overall result is negative and no etching of the alumina ceramic using simple wet chemical approaches is possible and can be recommended for current work and further production. Separate research can be done in order to find out as to why only one of three types of the ceramic substrates could be processed. One possible explanation could be that ceramics of type 708 with 96% of Al_2O_3 has 4% of soluble silicate binding agents, whereas type 710 has only 0.4% of them. Thus, type 708 is more suitable for wet etching [69]. It is of course of interest, what chemical reactions run in this case. This does not, however, explain why 91% ceramic could not be etched, either, although it has even greater part of silicate binding agents. In future work, other ceramic types must be investigated.

Nevertheless, the utilization of such wafers in the processes where no bulk micromachining would be foreseen had to be checked as well. In order to do this, a set of five 4-inch 500 μm thick polished down to Ra = 0.1 μm alumina wafers of type Rubalit KER 710 supplied by CeramTec was taken. Using the technology of the passive actuator from previous works [51], it was proven, that most of ceramic substrates of this type are in principal suitable for most of the conventional silicon technology steps involved.

The only serious issue found was impossibility of precise and repeatable alignment of the photoresist coated substrate during the second lithography step due to almost invisible alignment markings. This issue makes the whole process unreliable. The reason of it remained unclear. Although the assumption was made that the roughness of the substrate surface must be much better than Ra = 0.1 μm. This, however, would make the substrates more expensive.

Based on the experimental material collected above, it can be concluded, that for the R&D work conventional silicon substrates remain the most effective solution.

3.4 Actuator fabrication

In this subsection, the production related questions are discussed in detail. Precise descriptions of technological flows for production of passive and active (with electrical contacts) actuators as well as for a microvalve are given.

3.4.1 Fabrication of photomasks

The process of the actuator/valve fabrication incorporated from 2 to 5 photolithography steps depending on the complexity of the device[20]. In order to reduce the costs, it was decided not to purchase the expensive chromium-glass masks, but to produce them at the IMSAS using preordered foil masks. The dimensions of the structure as well as not very strict resolution requirements allowed doing so.

For that purpose, 4 inch borosilicate glass wafers were utilized. After conventional cleaning in the peroxymonosulfuric acid, the wafers were sputtered with 100 nm of Cr. Then, a photolithography with 2 µm thick positive photoresist and a corresponding foil mask was done similar to the first photolithography step described in Subsection 1.3.1.3. The foil masks were glued to the glass in order to make the placement into the mask aligner and the exposure possible. Cr was then etched with "Chrom Etch 3144" etcher, and the resist was stripped off with acetone and isopropanol. Figure 3.11 shows an example of one of the produced masks.

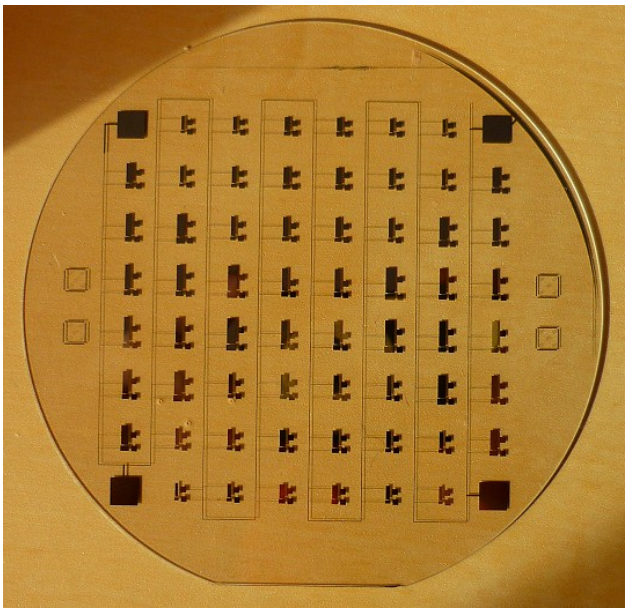

Figure 3.11: First design of a borosilicate glass photomask for bottom electrodes

3.4.2 Fabrication of a passive actuator

In this subsection, the fabrication of a passive actuator will be described. Passive actuator has neither bottom electrode nor contacts. No isolation layer was deposited, neither. The structure only incorporates seed layer, insulation layer and an actuator beam. This makes the fabrication much simpler. However, the flow includes many core processes, such as electroplating, PVD, lithography, wet and dry etching. The aim of the experiments was to tune these core processes before a step to more advanced processes could be made.

First, a step-by-step description of the process flow will be given. Then, the issues met during the work will be discussed, following by a short conclusion.

[20] From simple passive actuator to a complex integrated microvalve

3.4.2.1 Process flow description

Figure 3.12 gives a schematic representation of the process flow of the passive actuator production.

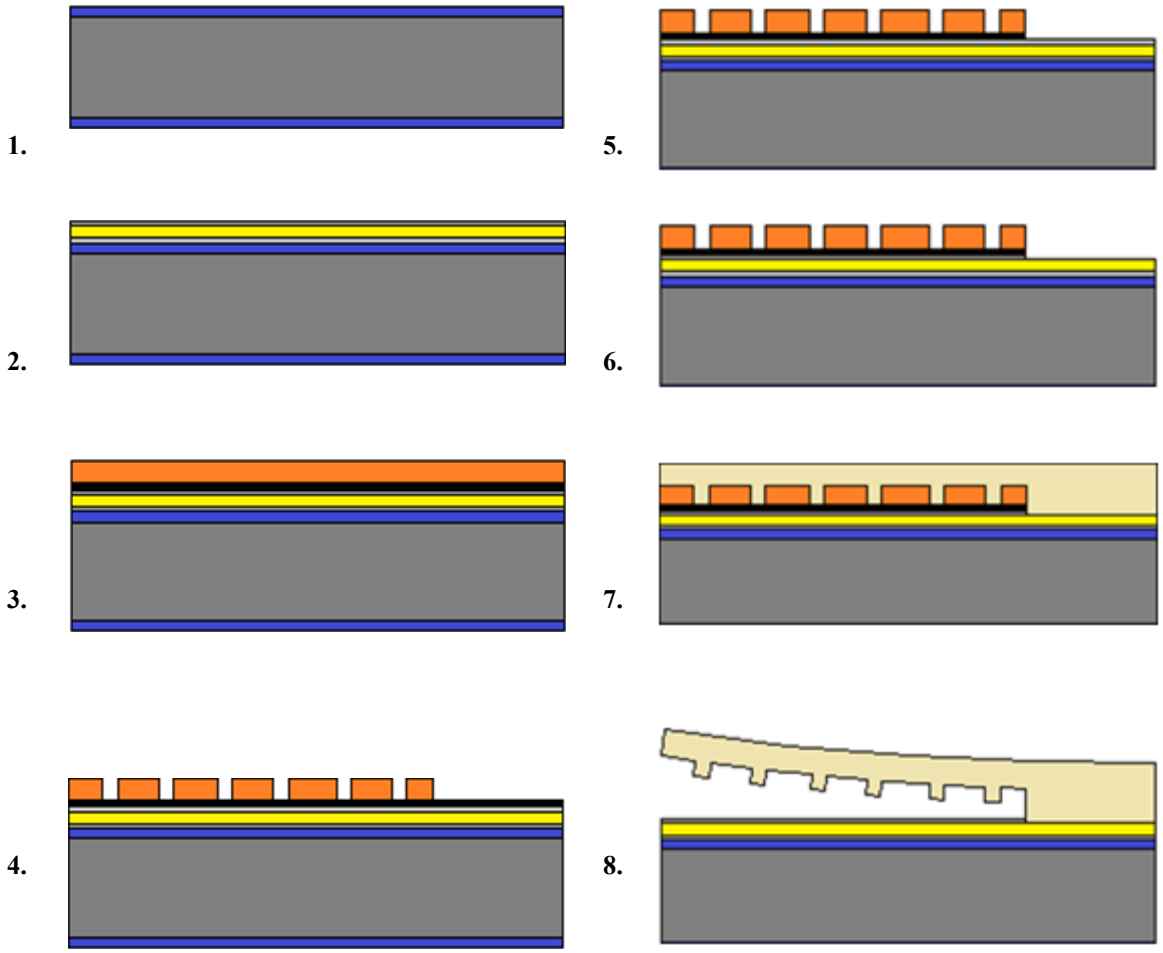

Figure 3.12: Passive microactuator production flow

A production lot with five 4 inch 380 µm thick silicon wafers was used for the production. The process began with conventional cleaning in the peroxymonosulfuric acid. Thereupon, a wet thermal oxidation was done. SiO_2 of 500 nm thickness was grown on both sides of the wafer (Fig. 3.12.1). Next, a seed layer of 15 nm of Cr and 80 nm of Au was sputtered over the surface of the substrate followed by sputtering of additional 15 nm of Cr (Fig. 3.12.2). The latter would be used as a material for bottom electrodes in the next technology research phase. Here, it was sputtered in order to study its reliability and interaction with other basic processes. It was not structured. Hence, no real electrodes were present.

The next step was a subsequent sputtering of 100 nm of Ti and 300 nm of Cu as a sacrificial layer for the future actuator release etching (Fig. 3.12.3). Then, the first and second lithography steps defining the antistiction bumps and actuator attaching area were performed (Fig 3.12.4). First, wafers were heated on a hot plate at 120°C for 2 min. in order to remove remaining

moisture. Then, adhesive agent TI-Prime was spin-coated and the wafers were again heated on a hot plate at 100°C for 2 min. After that, a positive 2 µm thick photoresist AZ®1518 was spin-coated over the surface of the wafer, followed by a softbake step on a hot-plate at 120°C for 2 min. The contact vacuum 2.2 sec. long exposure with UV-light was performed on a Süss MA6 mask aligner. After the development step, the resist was additionally hardbaked on a hot-plate for 2 min. at 100°C. Next, a descumming in oxygen plasma was done. Cu was then wet etched in the resist openings using a mixture of Alketch I and Alketch II 2:1 solution diluted with H_2O (1:10). Etching time was about 10 sec. Petri dishes were used. After that Cu was completely etched away from the resist-free zones.

Figure 3.13 shows circular bump openings in a Cu layer. Ti can be seen on the bottom of the opening.

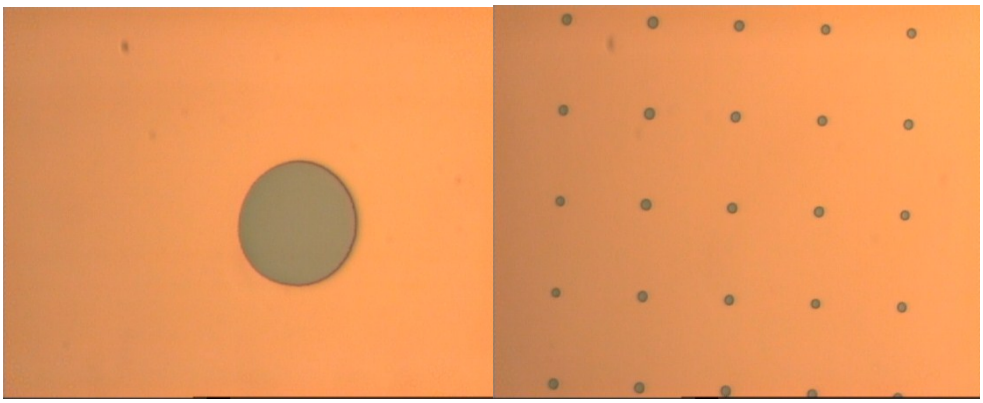

Figure 3.13: Wet etched cavity for a stand-off bump in a Cu layer:
left – single opening
right – array of openings

After that, the actuator attaching areas were defined. This time, a 10 µm thick layer of the AZ®4562 photoresist was used. Before coating with the resist, wafers were heated on a hot plate at 120°C for 2 min. Then, the adhesive agent TI-Prime was spin-coated and the wafers were again heated on a hot plate at 100°C for 2 min. After coating, the wafers were softbaked on the hotplate at 100°C for 10 min. and left at room temperature for 30 min. The wafers were contact exposed in the MA6 for 35 seconds and developed using AZ 400K developer. One more postbake step was then performed on a hotplate at 110°C for 60 sec. The resist residuals were removed by descumming in oxygen plasma. Titanium was then wet etched in the SiO_2 etcher. Etching time was approx. 10 minutes. During this step, backside layer of SiO_2 was etched (Fig 3.12.5). Subsequently, Cr was wet etched in a Petri dish in “Chrom Etch Plus” for 10 minutes (Fig. 3.12.6).

Then, third photolithography step defining the actuator geometry for electroplating was performed. A 30 µm thick positive photoresist AZ®4562 was spin coated in 2 steps. First, wafers were heated on a hot plate at 120°C for 2 min. Then, adhesive agent TI-Prime was spin-coated and the wafers were again heated on a hot plate at 100°C for 2 min. After that the first layer was spin-coated and the resist was hardbaked in oven for 5 min. at 90°C. The wafers were left at room temperature for 15 min. for cooling. Directly after that, the second coating was performed and the wafers were left in oven for 60 min at 90°C. Before the exposure, the wafers were kept in

a horizontal position at room temperature for 24 hours. The contact vacuum 60 sec. long exposure with UV-light was performed in a Süss MA6 mask aligner.

After the development in AZ400K developer and descumming in oxygen plasma, the electroplating of two Ni layers was performed in the nickel sulfamate electrolyte with pH 3.5 under the conditions descried in Section 1.2. Thereupon, the wafers were rinsed in DI-water and photoresist was stripped off with acetone and isopropanol (Fig. 3.12.7). The sacrificial Ti/Cu layer was wet etched (Fig. 3.12.8). Cu was etched in Alketch I+II solution in a Petri dish for 24 hours. Ti was etched in SC1[21] for 30 – 60 min[22] in a beaker on a hot-plate. The solution was constantly agitated. Wafers were fixed inside the beaker with polymer single wafer holder. The wafers were then washed in DI-water in a quick dump rinser and dried in a spin rinse dryer.

3.4.3 Fabrication of an active actuator

In the following, the fabrication process of an active device variant will be described. This process basically had three additional steps in comparison with the one discussed in the previous subsection:

- definition of the bottom electrodes and electric contacts
- deposition of the isolation layer
- formation of the contact openings in the isolation layer

Definition of the bottom electrode included

- deposition of the electrode and contacts layer
- photolithography of the electrodes and contacts layout
- etching of the electrodes

Si_3N_4 was chosen as an isolation layer. It was deposited over the electrodes using PECVD technique.

The contact openings in the Si_3N_4 layer were made by wet etching in the Oxide Etch solution.

3.4.3.1 Process flow description

Since all the steps except those for electrodes, contacts and isolation layer formation are the same as before, it makes no sense to repeat them again. Detailed description of only the newly developed ones will be given.

Bottom electrodes

The process of the electrodes and contacts formation begins with sputtering of a sandwich of Cr/Au/Cr layer with thicknesses of 15 nm / 80 nm / 15 nm respectively over the oxidized surface

[21] 1:1:5 solution of $NH_4OH + H_2O_2 + H_2O$ at 80 °C

[22] Time depends on the size of the actuator.

of a 4 inch 380 µm silicon wafer. Then, a lithography step with 30 µm thick positive resist AZ®4562 was performed. Before the exposure, the wafers were hardbaked in oven under 90°C for 60 min. and afterwards left for 24 hours under room temperature. One more hotplate postbake step at 110°C for 60 sec. was done after the development.

It had to be decided about the method for etching the Cr layer. Two possibilities existed:

- Wet etching with solutions available at hand: "Crom Etch Plus" from Candor Chemie and "Crom Etch 3144" from Honeywell
- Dry plasma etching in STS-Tool

First, wet etching with a commercially available "Crom Etch 3144" solution from Honeywell Intl. was performed. Average etching rate was measured to be approx. 65 nm/min. Thus, only a short 10 sec. dip was needed to etch away a 15 nm thick layer of Cr.

Optical inspection after the etching showed disproportionally deep (3 to 4 µm) underetching of Cr (Fig. 3.14).

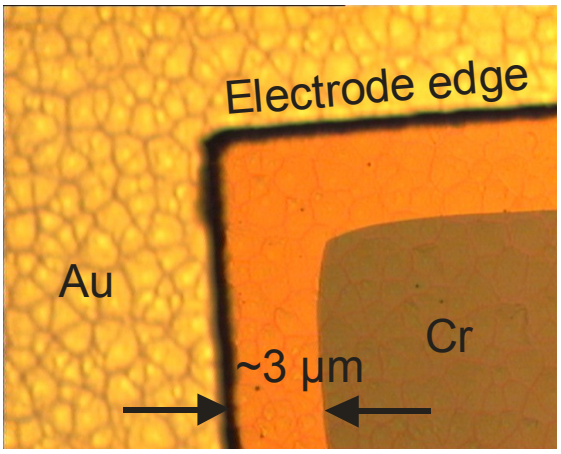

Figure 3.14: Chrome underetching in Chrom-Etch 3144 after 10 sec. dip

Some thin structures were severely damaged or even stripped away (Fig. 3.15).

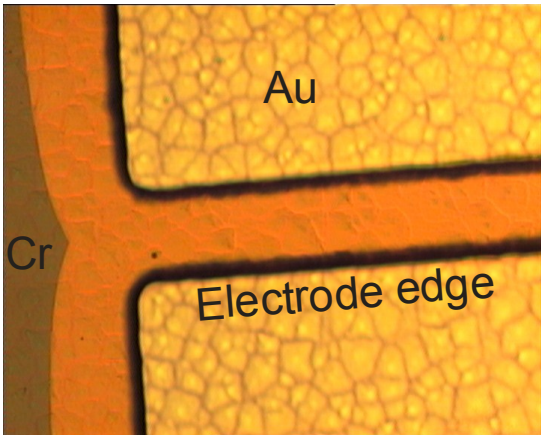

Figure 3.15: Chrome underetching in "Chrom-Etch 3144": thin structure destroyed

First suggestion was bad resist adhesion. Thus, a rework was done. All the metallic layers were etched away, wafers were cleaned and then metallic layers were redeposited. After that, a lithography sequence of 30 µm thick positive resist AZ®4562 was performed with preliminary Ti Prime adhesive agent was performed. After that, a lithography sequence of 30 µm thick positive resist AZ®4562 was performed with preliminary Ti Prime adhesive agent was performed. Post-development bake step was done with 120°C for 60 sec. Chrome was then 10 sec. dip etched in "Chrom Etch 3144". The result was the same: wide underetching profiles.

After several discussions [70], the conclusion was made that the reason for such a phenomenon is the so called electrochemical corrosion of chrome due to a big difference between the electrochemical potentials of chrome (-0.74) and gold (+1.52) being together in the acidic environment of a "Chrom-Etch 3144" solution.

Another chrome etching solution was used: "Chrom Etch Plus". In spite of all preliminary procedures to avoid attacking of photoresist by this solution, the resist was severely damaged by "Chrome Etch Plus".

Thus, dry etching of chrome in argon plasma in an STS machine was then investigated. The wafers were sputtered with Cr/AuCr layers and covered with 1.8 µm, 6.5 µm and 10 µm thick photoresist. Several etching experiments were conducted. First, five wafers with thinnest 1.8 µm thick photoresist were processed with following parameters:

Power: 20 Watt
Ar-flow: 20 sccm.
Pressure: 8 mTorr
Time: 30 min.

Result: no etching was seen.

The second set of parameters was:

Power: 50 Watt
Ar-flow: 20 sccm.
Pressure: 8 mTorr
Time: 15 min. + 15 min. without pause

Result: chrome was only partly etched. Resist was almost etched away.

For the next try, five wafers with 6 µm thick photoresist were taken. The etching parameters were

Power: 50 Watt
Ar-flow: 20 sccm.
Pressure: 8 mTorr
Time: 15 min.

Result: resist was partly damaged, but not etched away. After the resist strip-off, the etched profile of the upper chrome layer was measured with the Alpha-Step contact profilometer. The etching rate was determined to be approximately 2 - 3 nm/min.

Next, five wafers with 30 μm thick resist were processed. This time, it was tried to remove the Cr/Au/Cr sandwich completely

Power: 50 Watt
Ar-flow: 20 sccm.
Pressure: 8 mTorr
Time: 60 min. without pauses +15 min. +15 min. for the lower Cr layer
Postprocessing: short dip into "Chrome Etch Plus"

Result: Bubbling of the resist, damage of the electrodes geometry.

The next experimental set used five wafers with 10 μm thick photoresist and the following parameters:

Power: 50 Watt
Ar-flow: 20 sccm.
Pressure: 8 mTorr
Time: 8×15 min. with pause after each 15 min.
Postprocessing: short dip into "Chrome Etch Plus"

The function of pauses is to let the wafer cool down in order to avoid the damage or burning of the resist.

Result: Cr/Au/Cr sandwich is almost completely etched away; resist ashes on the surface (Fig. 3.16), which could not be cleaned chemically but only manually with the towel dipped in acetone.

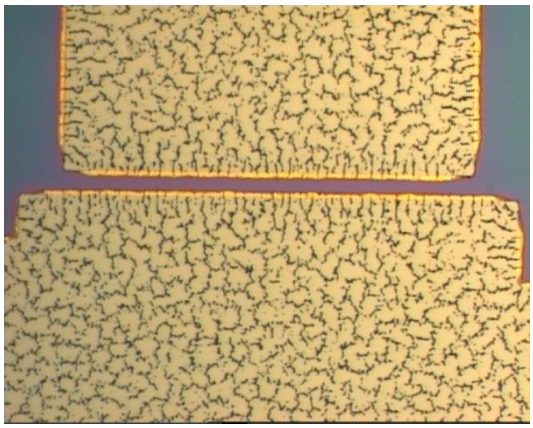

Figure 3.16: Resist ashes on the Cr electrodes surface after Ar-plasma etching

It was then obvious that overheating of wafers during the processing is responsible for bad results. Increase of pause time did not help. Therefore, a special thermal paste was applied on the back side of the wafer in order to prevent the overheating during the processing. This paste was then stripped from the wafer and the vacuum chamber of the STS machine manually with the acetone and towel. The etching was done with the following parameters:

Power: 50 Watt
Ar-flow: 20 sccm.
Pressure: 8 mTorr
Time: 8×15 min.
Postprocessing: short dip into “Chrome Etch Plus”

The etching result is shown on Figure 3.17.

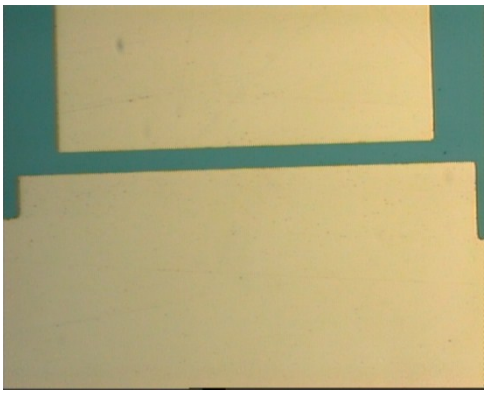

Figure 3.17: Dry etched Cr/Au/Cr electrodes: etching with thermal paste

One more experimental setup was used in order to check, if one more solution could be used. Five wafers with Cr/Au/Ti (15nm/80nm/50nm) layer electrodes were etched. The upper Ti layer was first wet etched in a 7:1 Oxide Etch solution for 45 – 60 sec. The rest was etched in argon plasma for 75 min with thermal paste and pauses each 15 min. Power was 50 Watt, Ar-flow was 20 sccm. und 8 mTorr pressure. Etching was successful. The result is represented on Figure 3.18.

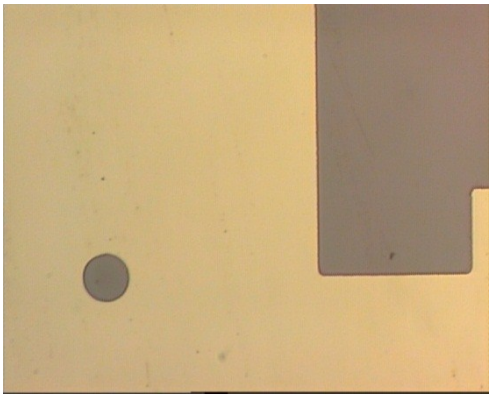

Figure 3.18: Etching result of a Cr/Au/Ti electrode.
Ti layer was wet etced, Cr/Au were dry etched in Ar-plasma

It was decided to proceed with the Cr/Au/Cr stack, since later on titanium sacrificial layer would be etched. Hence, using titanium as a part of the electrode could be risky.

Isolation layer

After successful etching of bottom electrodes, the wafers had to be deposited with an isolation layer that had to protect the electrodes against short circuiting during the operation. Many dielectric materials can serve as isolation layers: Si_3N_4, SiO_2, Al_2O_3 to name a few. Alumina was excluded due to technologically difficult etching processes, which were described in Chapter 1.3 of this work. SiO_2 could be an attractive solution, but the technological process of the system production included several oxide etch steps where this layer could be directly attacked and therefore, made SiO_2 impossible for use.

PECVD Si_3N_4 was finally chosen as an isolation layer due to its good dielectric properties and technological availability. The disruptive strength of Si_3N_4 is $E_{D,Nitride} \approx 5\times10^6$ V/cm [71], which makes a 100 nm thick layer capable to withstand the voltages up to 100V. In order to guarantee reliable function of the isolation layer, it was suggested to keep its thickness between 200 nm and 400 nm. Low-stress Si_3N_4 layer was deposited. The deposition parameters were:

Deposition time: 18 min.
N_2 flow: 1960 sccm
NH_3 flow: 50 sccm
SiH_4 flow: 40 sccm
Power lf/hf: 31/27 W
Pressure: 902 mTorr

After deposition, the thickness of Si_3N_4 layer was measured. It ranged from 293.6 to 304.6 nm.

Contact openings

The function of the contact openings is to provide electrical contacts between the voltage source and the electrodes. The openings must be etched in the Si_3N_4 isolation layer that covers the top surface of the wafer completely. Before that, a sacrificial layer of 100 nm of Ti and 300 nm of Cu was sputtered above the layer of Si_3N_4. Hence, these two materials also had to be etched. Simultaneous etching of three materials saved at least one lithography step. But on the other hand, a set of etchants had to be carefully chosen in such a manner that each etching step would only attack right materials. After a convenient lithography step with 10 μm thick positive photoresist AZ®4562, the etching procedure was done as follows:

- etching of Cu with Alketch I+II solution for 10 sec. Process stops at Ti layer.
- etching of Ti and Si_3N_4 with Oxide Etch solution for 10 min. using underlying Cr as an etch-stopper.
- etching of top Cr layer of the Cr/Au/Cr sandwich with Chrom Etch Plus solution for 10 min. to open Au, which is better for contacts.

The method described above retuned very well defined and precise golden contact openings. The rest of the process in general repeats the flow for a passive actuator described in Subsection 3.4.2.

3.4.4 Fabrication of a microvalve

As it was stated in Chapter I of this work, one of the most frequently occurred practical applications of an electrostatic actuator is microvalves. A microvalve is a complex system that includes flow inlet and outlet channels, electric contacts, an actuator, or several actuators to open and close the channels, and finally housing with all the necessary electric and fluid connections to the outer world. In this work, principal possibility of the actuator integration into a microvalve and its functionality had to be proven.

From the design point of view, a microvalve chip only differs from an active actuator chip by having a gas inlet channel underneath the actuator. The actuator itself must also have a so called boss against the channel opening to ensure better sealing.. From the technological point of view, these design differences significantly complicate the production process. The most challenging tasks were:

- implementing a boss element into the actuator
- etching of the gas inlet channel in a 380 μm thick Si wafer
- sacrificial layer etching

The boss is nothing more but a big bump. Therefore, the first task was solved by redesigning the stand-off bumps photomask and implementing it during the appropriate process step. After that, the electroplating was done as it was already described in the previous subsections. The remaining problems were more challenging. First of all, the etching of the gas inlet channel had to be performed from the back side of the wafer. Hence, backside alignment and backside alignment markings had to be foreseen. Second, the etching of the channel stopped on a thin (500 nm) film of the SiO_2. This thin membrane should not be damaged in order not to ruin the entire process.

The etching of the sacrificial layer was the last process step. Hence, it should have been done very carefully in order not to damage any of the other layers. On the other hand, sacrificial layer had to be removed completely. Otherwise, short circuiting of the electrodes would happen.

Taking into consideration the points described above as well as the already researched and solved tasks, a production flow was designed. Its detailed description is given in the following subsection.

3.4.4.1 Microvalve production flow

A lot of ten 380 μm thick Si wafers was taken as a starting material. The process began with conventional cleaning in the peroxymonosulfuric acid. Thereupon, a wet thermal oxidation was

done. SiO_2 of 500 nm thickness was grown on both sides of the wafers (Fig. 3.19), after which cleaning in the peroxymonosulfuric acid was repeated.

Figure 3.19: Microvalve flow: thermal oxidation

After that, a 50 nm thick layer of Cr was sputtered on the back side of wafers. After the first lithography step with 10 µm thick positive photoresist AZ®4562, the etching of Cr in "Chrom Etch Plus" was done in order to achieve the back side alignment markings (Fig. 3.20).

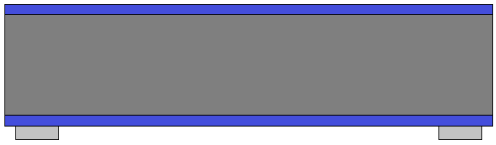

Figure 3.20: Microvalve flow: back side alignment markings

Then, the adhesion and bottom electrodes layer of 15 nm of Cr, 80 nm of Au and other 15 nm of Cr was sputtered on the top side of the wafers (Fig. 3.21).

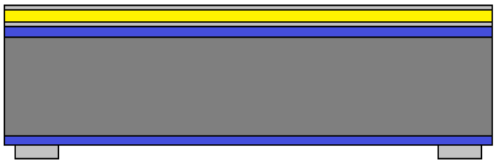

Figure 3.21: Microvalve flow: adhesion and bottom electrodes layer

After the second photolithography step[23], this metal sandwich was then dry etched in Ar-plasma as described in Subsection 1.4.3.1 (Fig. 3.22). Thermal paste was used to avoid overheating of the substrate and burning of the photoresist. The etching was done with the following parameters:

Power: 50 Watt
Ar-flow: 20 sccm.
Pressure: 8 mTorr
Time: 8×15 min.
Postprocessing: short dip into "Chrome Etch Plus"

[23] Backside alignment

In order to avoid the etching of the back side alignment markings during the dip into "Chrome Etch Plus", they were manually covered with photoresist using a brush before the dip.

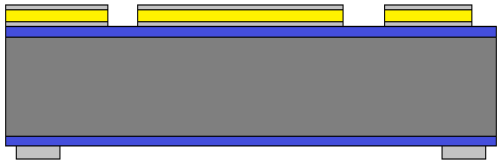

Figure 3.22: Microvalve flow: structured bottom electrodes

Then, a complex photolithography step was done. First, a thin 1,8 µm protective layer of a positive photoresist AZ®1518 was spinned on to the electrodes. The wafers were then heated on the hot plate for 2 minutes at 120°C. After that the back side was covered with a 10 µm thick positive photoresist AZ®4562. In order to avoid the DRIE of the alignment marking fields[24] on the wafer, the markings on the mask were manually covered with pieces of dark plastic. After that, an additional photolithography of 3 mm edge exclusion with one more special mask was done[25]. After these procedures the DRIE process was performed (Fig. 3.23).

Three first wafers were lost due to strong chirping at the edge. The reason of chirping was not clearly determined. It was assumed to be a problem of the Alcatel DRIE tool. DRIE of the gas inlet channels crowns the process of the microvalve part of the flow. The subsequent steps generally repeated the flow developed for the production of an active microactuator and described in the Subsection 3.4.3. However, there were some differences connected with now more fragile and more sensitive to the external coercions structure.

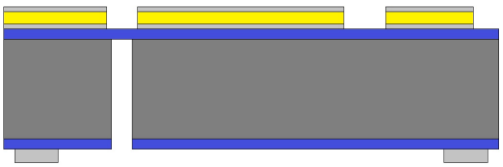

Figure 3.23: Microvalve flow: DRIE of gas inlet channels

As it can be seen on Figure 3.23, there is a very thin (500 nm) SiO_2 membrane, which covers the top of the inlet channel. Thus, careful handling had to be performed during the subsequent operations. It was not possible to use normal vacuum chucks (e.g. during photoresist spray coating) any more, since it could damage or even destroy the membranes and ruin the entire process. Special vacuum chucks were used instead. These chucks stick fast only to the edge region of the wafer.

After optical inspection under the microscope, PECVD of low-stress Si_3N_4 isolation layer over the top side of the wafers was done (Fig. 3.24).

[24] They were also transparent on the mask

[25] Requirement of the DRIE-Process, standard mask was used during lithography.

Figure 3.24: Microvalve flow: PECVD of Si3N4 isolation

Figure 3.25 depicts a gas inlet opening without SiO2 membrane.

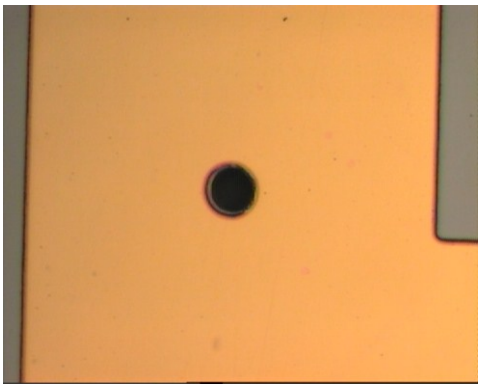

Figure 3.25: Gas inlet from the top side

The picture was taken after the whole microvalve production process was completed. The actuator was then torn off to make this photo possible.

Then, one more optical inspection step was performed in order to check the integrity of the membranes. After that, a sacrificial layer of 100 nm of Ti and 300 nm of Cu was sputtered (Fig. 3.26).

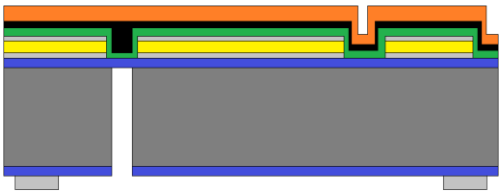

Figure 3.26: Microvalve flow: PVD of Ti/Cu sacrificial layer

In order to achieve the designed actuator geometries during future electroplating, Ti/Cu layer was structured in two lithography steps (Fig. 3.27). Also, Cr was wet etched from the areas where the actuator is attached to the bottom electrode. Contact openings were etched, too. These procedures are described in detail in the subsection 3.4.2.1.

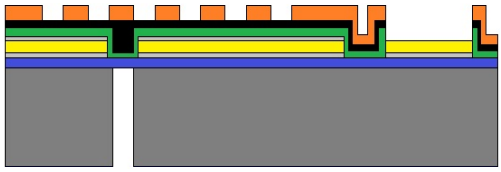

Figure 3.27: Microvalve flow: wet etching, microactuator geometry definition

Since no further backside alignment was needed, the backside alignment markings were not protected and hence, etched from the back side of the wafer as well as the backside layer of SiO_2.

Next, after photolithography with 30 µm thick positive photoresist AZ®4562, two layers of Ni were electroplated as described in Sections 1.4..2.1 and 1.2 respectively (Fig. 3.28).

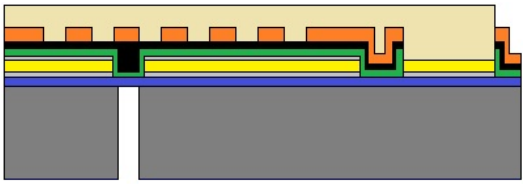

Figure 3.28: Microvalve flow: Ni electroplating

After the stripping of thick photoresist, the following step was to etch the SiO_2/Si_3N_4 membrane from the back side (Fig. 3.29). In order not to attack Si_3N_4 on the front side, it was laminated with so called dry photoresist. After that, the wafers were plunged into Oxide Etch 7:1 solution for 15 minutes. After that, they were cleaned in DI water and dried in a spin rinse dryer. Then, dry photoresist was exposed with UV-light in Süss MA6 mask aligner. After that the resist was stripped off in a Petri dish filled with photoresist developer.

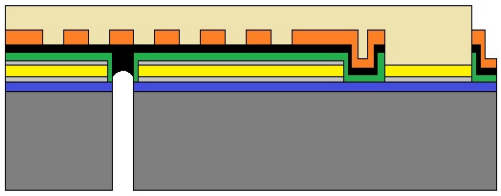

Figure 3.29: Microvalve flow: back side etching of the SiO_2/Si_3N_4 membrane

Now, the actuators had to be released and electrically disconnected from the bottom electrodes by etching of Ti/Cu sacrificial layer. First, Cu layer was completely etched with Alketch I+II solution in a Petri dish for 24 hours. Then, Ti was etched in SC1 for 30 – 60 min as described in Subsection 1.4.2.1. After that, the actuators were released (Fig. 3.30). The wafers were then washed in DI-water in a quick dump rinser and dried in a spin rinse dryer.

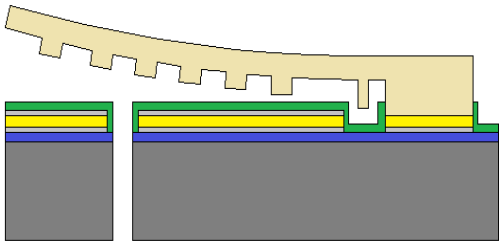

Figure 3.30: Microvalve flow: actuator release

In order to make sure that the electrodes were electrically disconnected and there was no short circuit, some actuators were torn off. Figure 3.31 illustrates a complete etching of Ti/Cu sacrificial layer.

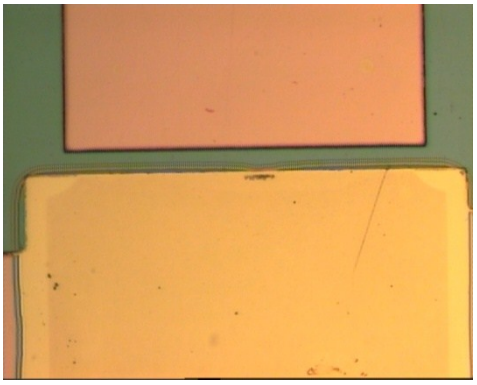

Figure 3.31: Electrically disconnected electrodes after Ti/Cu etching

For the upcoming characterization, single chips were needed. Hence, wafers had to be diced into single microvalve chips. Dicing procedure could be destructive for the actuators because of strong water flow introduced. This flow could detach the actuators from the surface. Therefore, second lamination with dry photoresist was done. Then, dry photoresist was exposed with UV-light in Süss MA6 mask aligner. Only after that the wafers were diced. And the resist was stripped off from single chips in a Petri dish. An REM photo (Fig. 3.32) represents a microvalve chip with microactuator and electrical contacts on top of it. Gas inlet channel is covered by microactuator beam and thus cannot be seen on this photo.

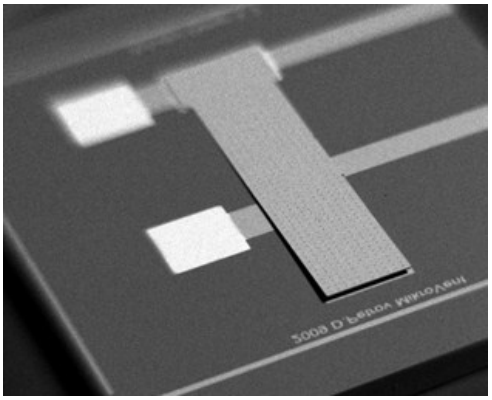

Figure 3.32: Fabricated microactuator on a chip (REM representation)

The system is a normally-open 2/2 microvalve. In accordance with specifications, it is possible to build a 3/2 microvalve by using two chips on the same platform inside one package.

3.5 Conclusion

Chapter 3 described the microactuator and microvalve production related topics. Among the most important once were:

- characterization of Ni electroplating process
- choice of alternative substrate material and study of its properties
- design of technological microactuator and microvalve production flow

The study of the electroplating process revealed that internal stresses in a deposited Ni layer mainly depend on the current density. Thus, it is possible to produce bended structures with desirable geometry by separately plating the layers one above the other using different current densities.

A study of the alternatives to conventional Si substrates showed that though there are many materials, which could be readily used as substrates (ceramics, FR-4, glass), from technological and financial point of view, Si remains the best choice. The closest competitor could be Al_2O_3 ceramic (alumina). This material is very widely used in industry; its costs are comparable with Si and it is available in a shape of wafers. Moreover, ceramic is a natural insulator. This fact saves oxidation step and potentially reduces the costs of the process. Thus, several types of Al_2O_3 of different purity were checked on their technological suitability to the process developed in this work. Wet etching, photolithography and electroplating with these substrates were studied. The studies revealed that there was no simple and cheap way to remove ceramic material by wet etching, though some slow removal took place in case of type Rubalit 708. Photolithography was in general possible, but the alignment of a mask to the pattern on the substrate surface in the yellow room was very problematic since no structures could be seen under the microscope even on the finest surface with Ra = 0,1 μm. Electroplating revealed no problems and run as usually done with conventional Si substrates. Summarizing the above mentioned facts, it was decided to go on with Si substrates leaving ceramic for future R&D work.

The design of the technological flow was divided into three main phases:

- fabrication of a passive actuator (no bottom electrode)
- fabrication of an active actuator (with bottom electrode and contacts)
- process development for integration of the actuator into a microvalve

The first phase included several runs of subsequent surface micromachining steps focused on electroplating and wet etching of sacrificial layers in order to check the reproducibility of the deposition process and correspondence of the actuators final geometry to the theoretical expectations.

During the second phase, bottom electrodes were added in order to make the actuator functional. RIE dry etching method was developed to achieve well defined bottom electrodes.

In the last phase, a through silicon microchannel made by DRIE was introduced underneath the actuator structure. All the separately developed flow steps were combined into a final technological flow resulting in a 2/2 microvalve chip where the actuator serves as an active open-close element.

4 Characterization

In this chapter, microactuators and microvalves designed and built as described in Chapter 2 and 3 are characterized. Mechanical and electrical behavior of the system was tested. Microvalve functionality was proven. In the first subsection, mechanical tests of the microactuators are discussed. They include shear-test, drop-test and temperature test. Additionally, the results of the actuators deflection before and after thermal cycling are presented. The second subsection is dedicated to the electrical tests of the system. The measurements of pull-in voltage and switching speeds of the actuators are discussed. The third subsection includes the description of microvalve functional tests. The fourth subsection discusses possible improvements in the design of microactuator and microvalve as well as in the measurement and test methods.

4.1 Mechanical tests

The tests described below characterized the quality of the production process and hence, the robustness of the system. Microactuator is an active part of the system. Therefore, it bears the most mechanical loads and its durability against mechanical shock must be proved.

4.1.1 Shear-test

At first, shear- tests of actuators were conducted. Shear testing is a simple, fast, and cost effective method to check system elements integrity on both wafer or chip level, both for process control and reliability monitoring. In this work, separate chips were tested. The scheme of the experiment is shown in Figure 4.1.

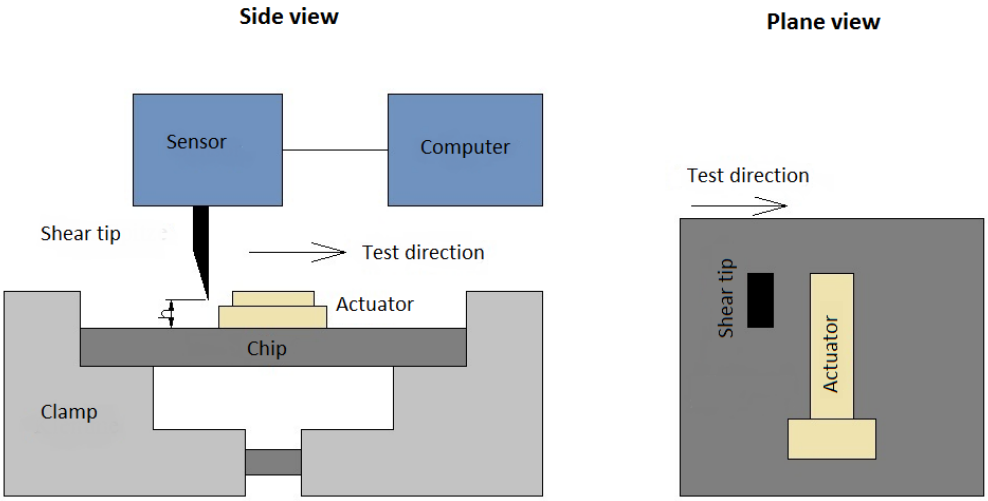

Figure 4.1: Shear test diagram (not to scale)

The tests were conducted in IMSAS with XYZTEC Condor 100 tool. The experimental setup is shown in Figure 4.2.

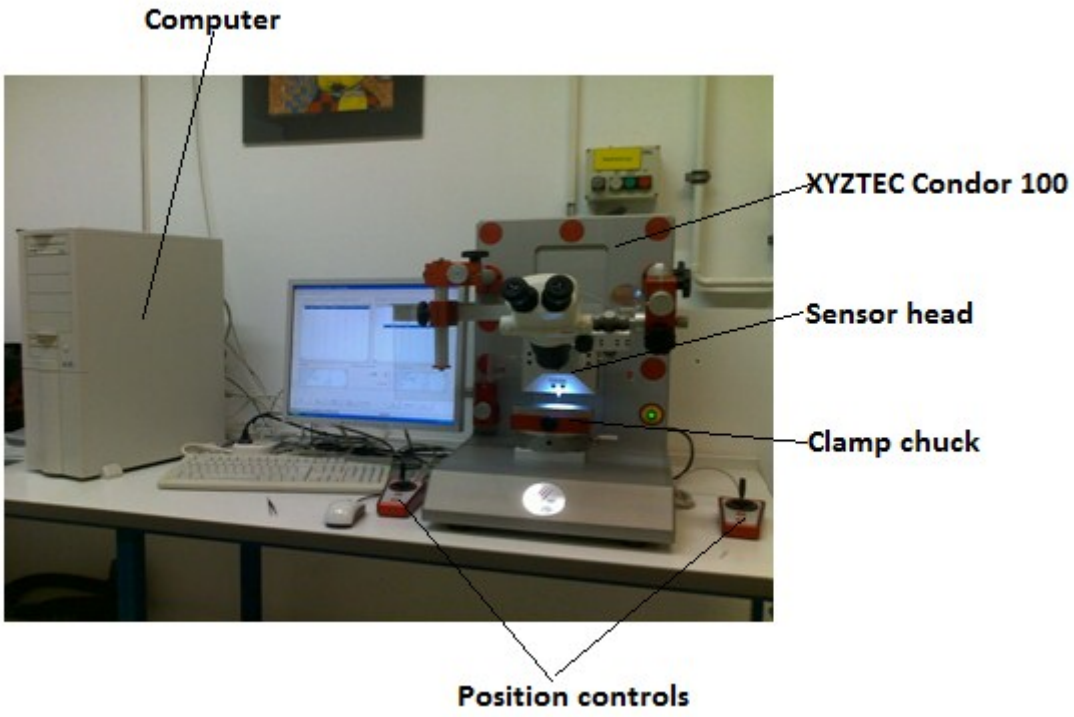

Figure 4.2: Shear test setup with XYZTEC Condor 100 tool

First, a chip was fixed in the clamp in such a position that the shear tip moved perpendicularly to the actuator as it is shown in Figure 4.1 (left). The shear force was always applied at the tip of the actuator to achieve the highest moment and hence, to simulate the worst load case. The positioning of the chip against the shear tip was performed by using the vertical and horizontal position controls and the microscope. The measurement process at the XYZTEC Condor 100 tool was controlled by a PC with dedicated software, where all the necessary parameters could be adjusted.

The following parameters were used during the tests:

Sensortype: Shear 100
Max. force range: 196,13 N
Starting speed: 80,0 µm/s
Tip height, *h*: 10 µm
Test speed: 100,0 µm/s
Test distance: 1000 µm

The test was performed for 5 different actuator designs with different length of the beam: design 1.2, 2.1, 3.1, 4.3 and 5.1. Five samples per design variant were tested. Shear tests before and after drop-down and thermal cycling were done. The set up for thermal cycling and drop-down tests will be described in the following subsections.

The results of the tests are represented in the Figure 4.3, where the force at which the actuator was broken vs. the length of the actuator beam are shown.

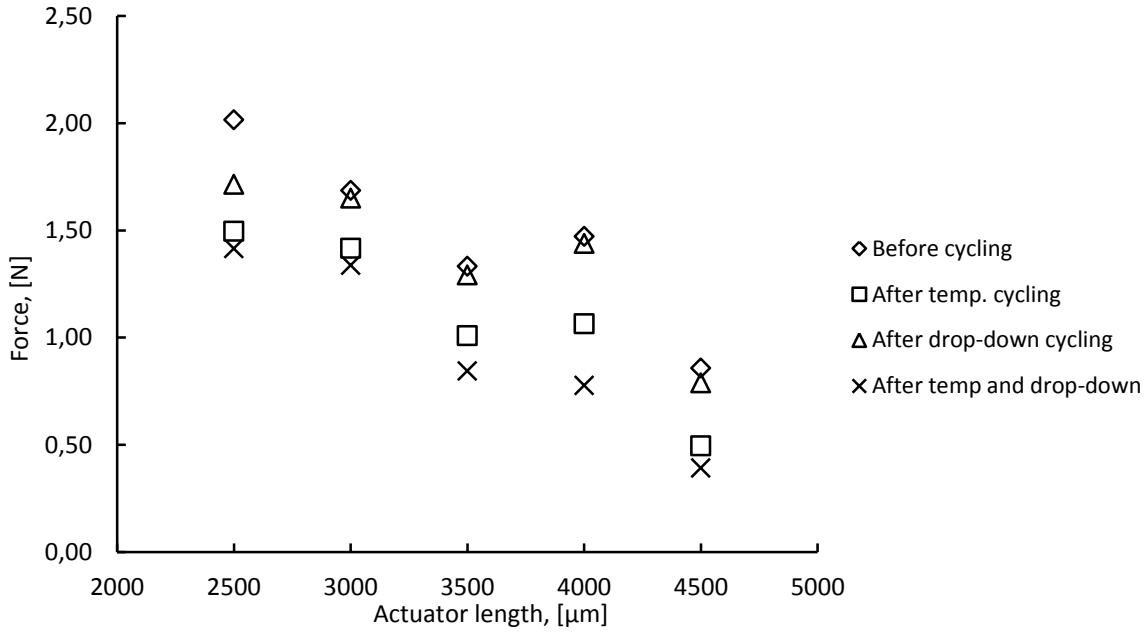

Figure 4.3: Failure force for different actuator designs

It can be clearly seen that actuator breakage force diminishes after cycling and that drop-down tests show less influence on the robustness of the samples than thermal cycling or combined load. Looking at statistical data (Fig. 4.4) one can say that the samples of design 2.x and 3.x perform the best stability out of all the designs.

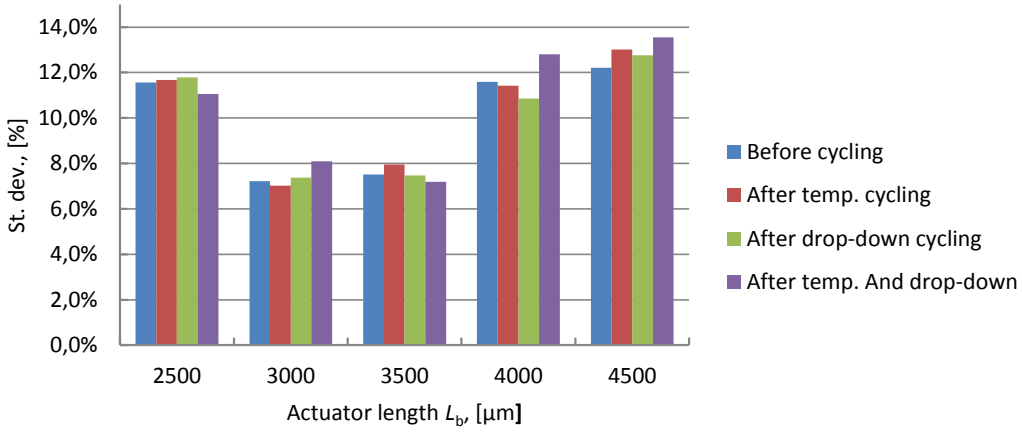

Figure 4.4: Standard deviation of the failure measurement for differnt actuator designs

Samples of smaller size (design 1.x, L_b = 2500 µm) as well as samples of the designs 4.x and 5.x (L_b = 4000 µm and L_b = 4500 µm) demonstrate somewhat worse results. In case of smaller

actuators an explanation can be that the etching of Ti/Cu was not complete for some devices (Fig. 4.5) in the case of these very small samples of the design 1.x and therefore, the actuators held stronger on the chip.

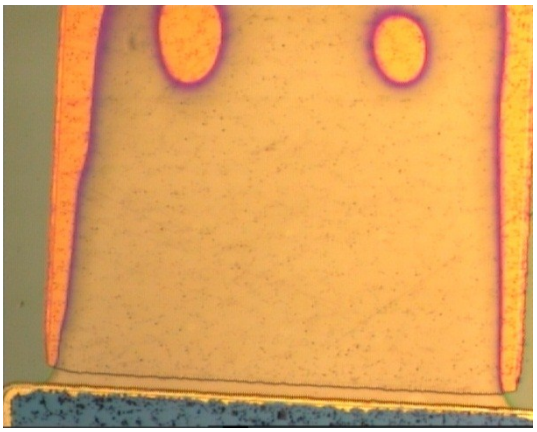

Figure 4.5: Remains of the sacrificial layer (actuator removed)

The etching of Ti/Cu was successful for the devices of the designs 4.x and 5.x. In this case, the measurement method could return errors. This could be due to the elastic deformation of the beam before failure.

As it was stated above, thermal cycling and drop-down tests were also done in combination with shear tests.

4.1.2 Drop-down test

Drop-down or simply drop tests serve for reliability testing of the system under extreme shock conditions. These tests are very important for the investigation of system behavior in real-life applications, when extreme accelerations often occur for example, automotive, medical, and aerospace applications.

The JEDEC standard JESD22-B111 [72] contains the regulations for the drop test procedures of electronic equipment. The peak deceleration of 1500 g for the duration of 0.5 ms is recommended by the standard. Figure 4.5 illustrates the typical half sinusoidal graph of deceleration vs. time.

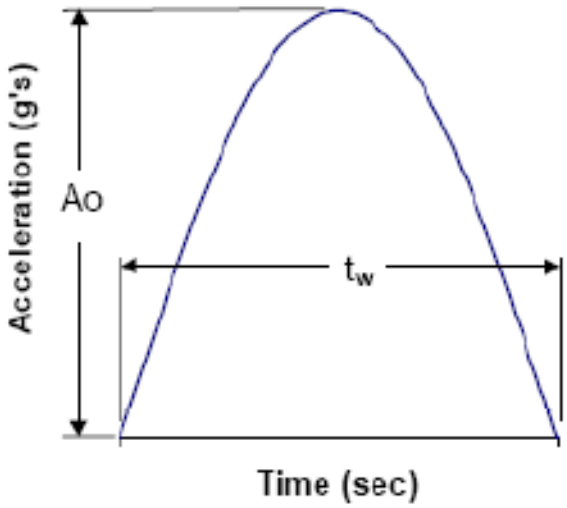

Figure 4.6: Typical half sinusoidal form of the deceleration vs. time (adapted from [72])

The deceleration A is the function of time

$$A(t) = A_0 \sin\left(\frac{\pi t}{t_w}\right), \tag{4.1}$$

where t_w is the width of the half sinusoidal graph.

Deceleration A also relates with the drop height H as

$$\sqrt{2gH} = \frac{2A_0}{C}\frac{t_w}{\pi}, \tag{4.2}$$

where C is the rebound factor (1.0 for no rebound, 2.0 for full rebound).

Theoretically, Eq. 4.2 can be used to determine the necessary drop height H to achieve the appropriate G. However, the peak deceleration and the pulse duration is a function of not only the drop height but also the strike surface. The strike surface effect is not included in *(4.2)*. Thus, experiments with different strike surfaces may be needed to obtain the desired peak deceleration value and duration.

According to the standard requirements, special equipment is needed to run a drop test [72]. In this work, a very simple approach was used. The soldered systems were just fixed in the stand at the height of approximately 20 cm and then dropped onto the rigid metal surface of the stands base. This is illustrated by Figure 4.6.

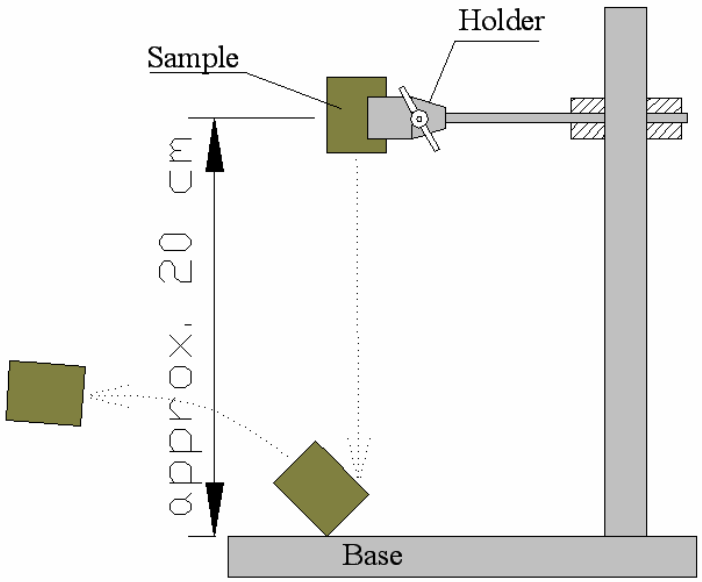

Figure 4.7: Scheme of a drop test set up

The drop test served only for the observation of the systems capability to survive it immediately after production. For each sample, a set of 10 drops in a row were done. The values of the shear force were measured after each set and compared to the initial shear test results (Fig. 4.3). By this, the influence of the drop test on the system reliability was observed.

4.1.3 Thermal cycling

A variation of temperature is a common condition in the real-life operation of electronic and MEMS devices. Materials used in the assembly of such systems commonly have different coefficients of thermal expansion (CTE). When temperature changes different deformations of the assembly occur. Consequently, stresses potentially leading to damages arise in the system. Thus, temperature cycling tests are widely used during the design and optimization of electronic systems in order to get the information about their reliability in different temperature conditions.

Figure 4.8 shows the setup for thermal cycling. The set up consists of a conditioning cabinet WEISS SB22160 and a PC with dedicated controlling software capable to regulate the temperature, duration and a number of other parameters of the test. In this work, temperature varied between -20°C and +70°C, which corresponds to the technical requirements of the systems operation (-10°C to 60°C, see Chapter II). The duration of one test was 48 hours.

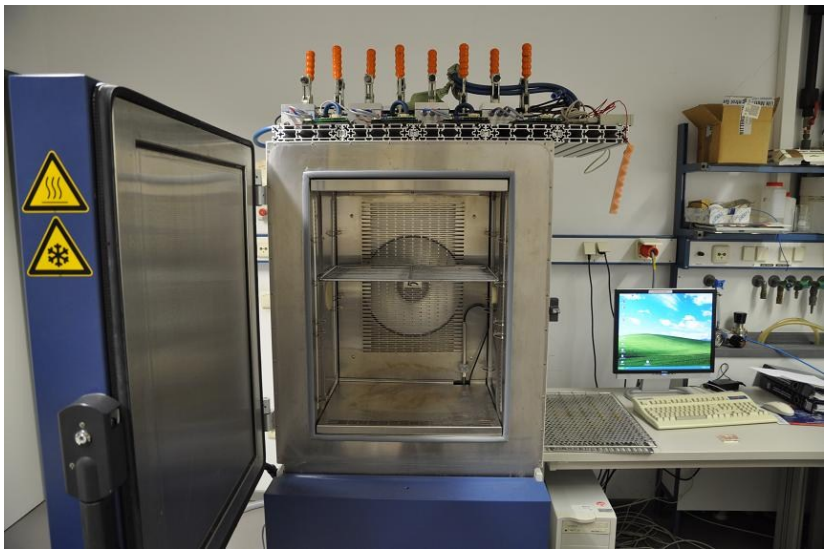

Figure 4.8: Thermal cycling set up

Figure 4.9 demonstrates a temperature profile used during tests. Horizontal axis represents time in hours. Temperature is shown along vertical axis.

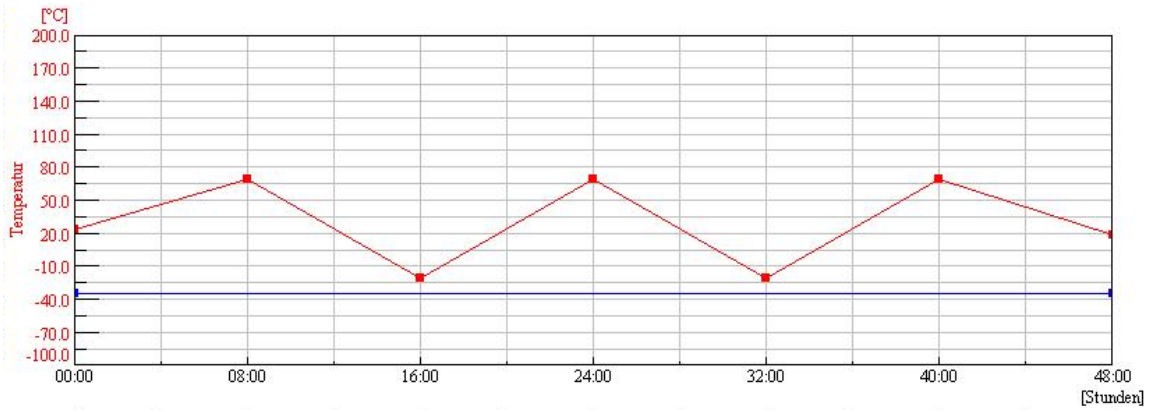

Figure 4.9: Thermal cycling temperature profile

After that, shear tests were done for one group of samples. For the other group of samples, drop tests were done after temperature cycling and then they were taken for the shear tests. The results are gathered in Figure 4.3.

The deflection of the actuator *s* is one of the most important parameters of the system since it determines the operating voltage and e.g. flow rate of the microvalve. Thermal loading could influence this parameter. Therefore, deflection was measured before and after thermal cycling. The measurement was performed optically under the microscope by tuning the sharpness of the image at the anchor and at the tip of the actuator and subsequently subtracting the heights of the microscope table. The results are represented in Figure 4.10.

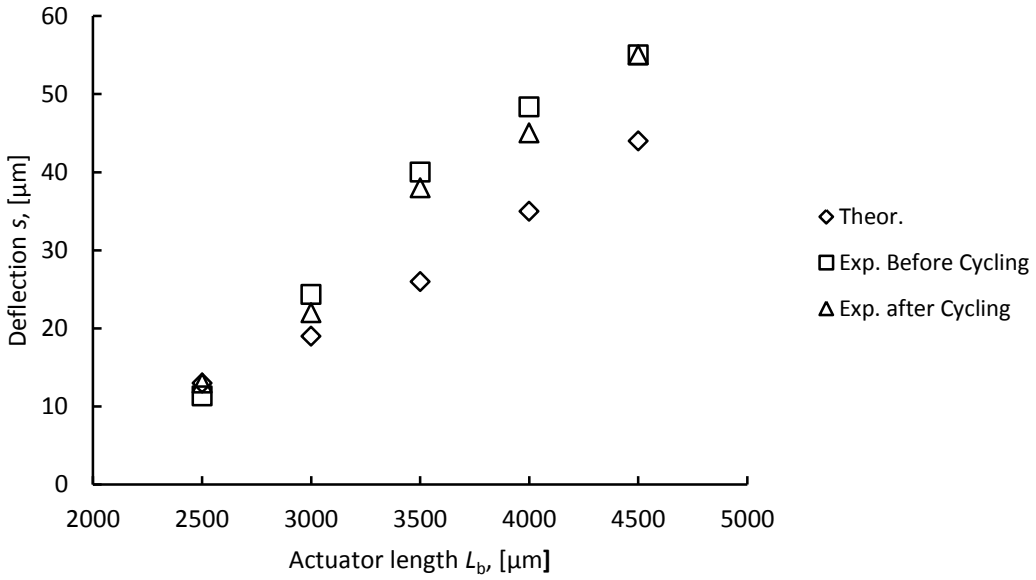

Figure 4.10: Deflection of the actuator *s* before and after thermal cycling compared with theory

The experimental data in Figure 4.10 are mean values taken out of five measurements done for each design variant. It can be seen that thermal cycling almost did not affect the deflection of the actuators. For small actuators (L_b = 2500 µm and L_b = 3000 µm), the experimentally measured deflection matches theoretical expectations almost perfectly. For longer beams, a certain deviation occurs. Measured values of deflection are higher than the theoretical ones with some trend to come closer to theory for the longest beams (L_b = 5000 µm).

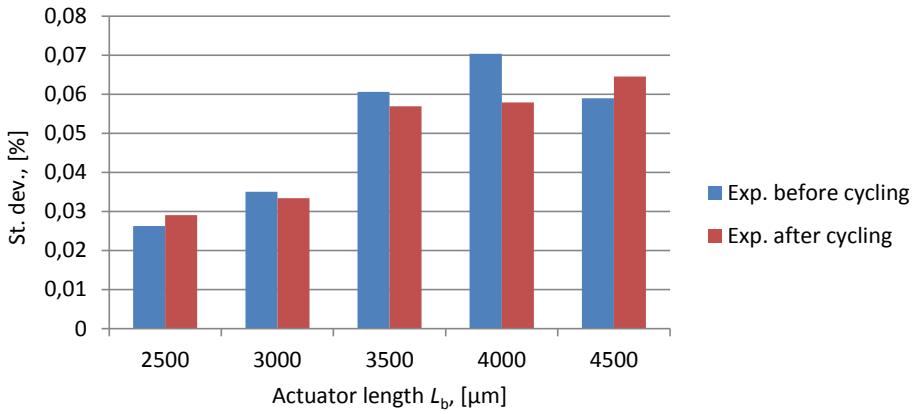

Figure 4.11: Standard deviation in % of the beam deflection measurements

A possible explanation of such behavior can lie in the fact that electroplated layers have non-uniform thickness distribution over the wafer. The structures, which are closer to the edge of the substrate, would be deposited thicker due to higher electric field. A map of design distribution

across the wafer can be found in Appendix II. From this map, it is clear, that the designs 3.x, 4.x and 5.x (L_b = 3500 µm, 4000 µm and 4500 µm) are mostly distributed around the center of the wafer. This also explains why statistical distribution of the measurement results is worse for these design variants (Fig. 2.11).

4.1.4 Mechanical tests: summary

Mechanical tests proved the capability of the devices to withstand extreme loads. None of the samples was lost after drop test, thermal cycling or after combined thermal-drop loading.

However, shear-tests showed some weakening of the structure after mechanical loads (Fig. 4.3). Hence, further production process improvements are to be done. First of all, choice of materials can be changed to improve the matching of the CTEs. Then, single process steps can be updated.

4.2 Electrical tests

The most important electrical parameters of the actuator are pull-in voltage and their switching time as they determine the limits of systems applicability. According to the requirements, pull-in voltage must be less than 60 V and minimal switching time should be less than 3 ms.

4.2.1 Measurement of pull-in voltage

In order to measure pull-in voltages, a microvalve chip was connected to a voltage source. This was done by gluing of a chip onto a simple FR4 circuit board and wire-bonding of the chip contacts to the contacts on the board. Figure 4.12 shows an example of such an assembly.

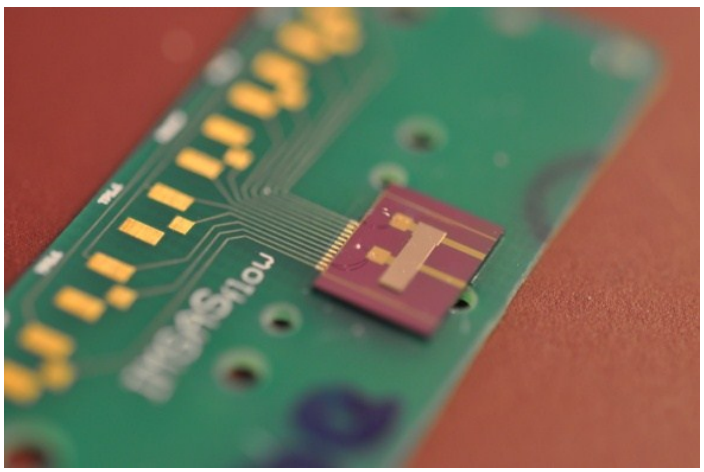

Figure 4.12: Microvalve chip on a circuit board ready for electrical tests

Two wires with connectors were soldered to the contacts at the board. The connectors were then attached to a standard voltage generator. Continuously increasing voltages from 1 V with

step of 0,1 V were applied to the system. In order to control the pull-in visually, the assembly was placed under the microscope (Fig. 4.13).

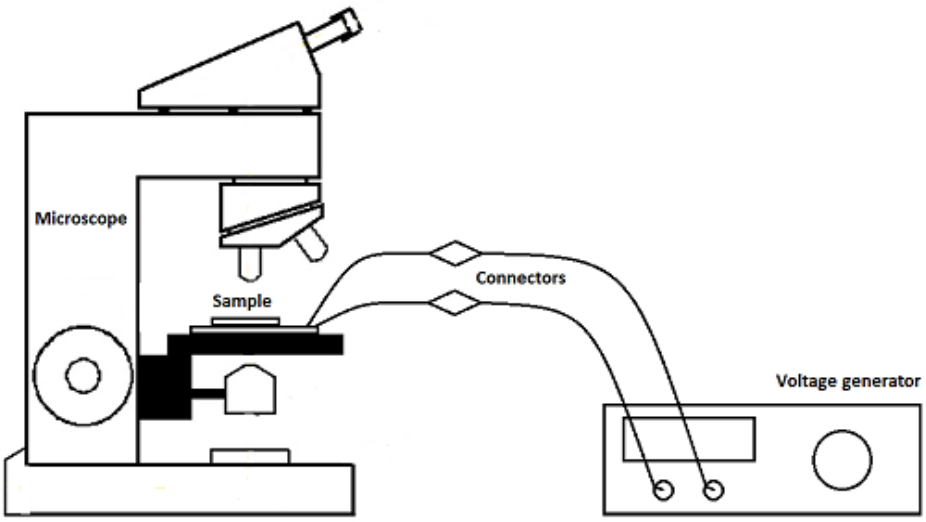

Figure 4.13: Pull-in voltage test set up

Five samples per design variant were measured at room temperature T = 23°C. The measurements of pull-in voltage were then repeated after drop test and temperature cycling (see Subsection 4.1). The measurement results are represented in Figure 4.14.

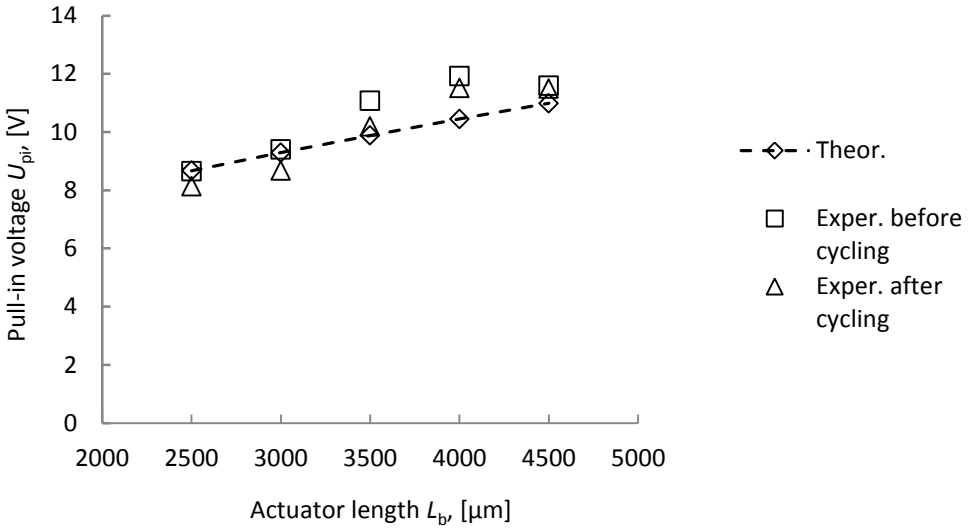

Figure 4.14: Pull-in voltage measured for different actuator designs

Measured values of pull-in voltage indicate good coincidence to the theoretically calculated ones. For the samples of design 3.x, 4.x and 5.x there is a slight increase of values. This is due to a higher value of deflection *s* (see Fig. 2.10).

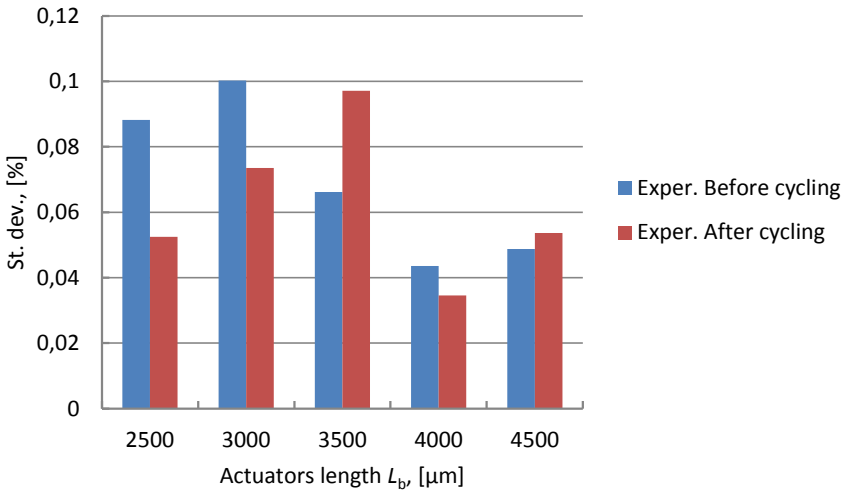

Figure 4.15: Standard deviation in % for pull-in voltage measurements

Figure 1.15 represents standard deviation distribution for experimental runs of different actuator designs. The most stable results were demonstrated by the samples of design 4.x. and 5.x. Except of the design 3.x, all the designs showed better standard deviation after cycling.

4.2.2 Reaction time tests

As it has been shown in Chapter II, the reaction time t_r will increase with the increasing actuator length (Fig. 2.16). According to the Table 2.4, the expected values of t_r must be between 1,6 ms and 5,1 ms for the designs 1.x to 5.x respectively. The specification limit was set to be 3 ms.

In order to measure the reaction time, a simple method was planned to be used. This method would allow measuring a resonance frequency of the actuator beam and thus, determining the maximal reaction time[26]. A test set up should have included a frequency generator, an amplifier and an optical microscope and look very similar to the set up on Figure 4.13 for pull-in voltage measurements. A square-wave signal from the generator had to be amplified by the amplifier and then applied to the electrodes of an actuator making it move. This movement could be then optically detected in microscope. Increasing the frequency of the square-wave, the operator could have found the point, at which the movement would have stopped. This would be a resonant frequency. After that, the reaction time could have been calculated using Equations 2.50 and 2.51.

The measurements could not be done due to the insufficient gain factor of the amplifier which could not deliver the necessary voltage.

[26] The same principle was used for the calculation of the reaction time in Chapter II.

4.2.3 Electrical tests: summary

The actuators pull-in voltage demonstrated good coincidence with the theoretically calculated values. Minimal values of less than 10V were measured. Actuators proved to deliver repeatable values of pull-in voltage also after thermal and mechanical cycling. The most stable performance was shown by the samples of the design 3.x.

A setup concept for the reaction time measurement was proposed. However, only theoretical estimations of the switching time were possible.

4.3 Microvalve functionality test

The principal characteristic to be proven during the microvalve functionality test was the flow rate. The expected values for different designs lie between 31 ml/min and 98 ml/min.

4.3.1 Flow rate test

A simple measurement method was used to prove the functionality of the microvalve. The scheme of the measurement set up is shown in Figure 4.16.

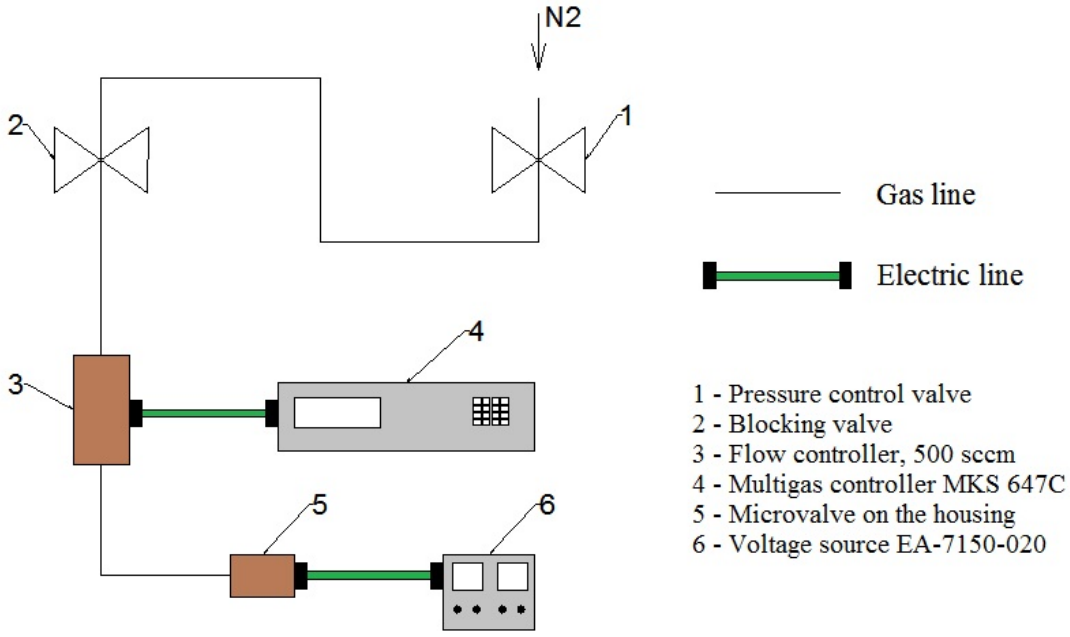

Figure 4.16: Flow rate measurement set up diagram

Figure 4.17 demonstrates the measurement working place.

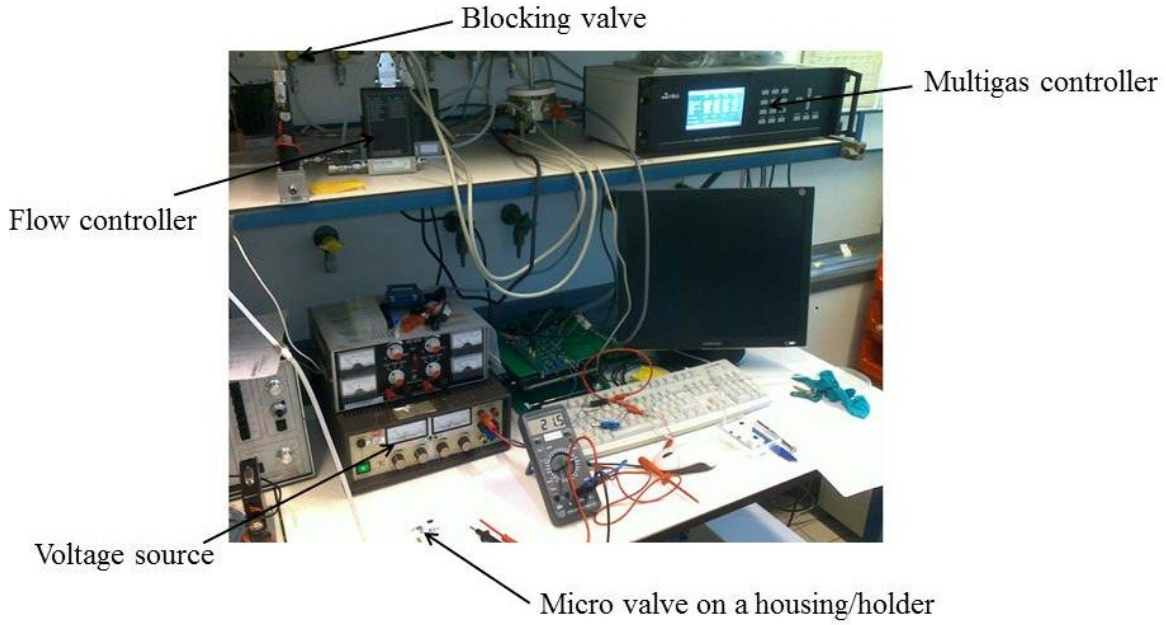

Figure 4.17: Flow rate measurement working place (pressure control valve (2) not shown)

The set up consisted of a flow controller, which limited the flow at 500 sccm, a multigas controller MKS 647C to control the gas flow, pressure control valve to adjust the nominal pressure, a blocking valve to open/close the gas flow, a voltage source to control the microvalve and a microvalve on a housing/holder (Fig. 4.18). A microvalve sample chip was leak-proof attached to the housing/holder using DELO "Katiobond 4557" (drying for 15 min. under 600W UV-light). The housing/holder was specifically designed for the samples used in this work. The technical drawing can be found in Appendix III.

Figure 4.18: A microvalve on a housing/holder

Nitrogen was used for the tests. The pressure of 2 bar was adjusted with the control valve (1). Then the minimal gas flow value of 25 sccm and a maximal value of 250 sccm was adjusted on the Multigas Controller MKS 647C (4). The values of the flow could then be changed within this

range. The actual values of the flow were then measured by the flow controller (3). Both adjusted and measured values could be monitored on the screen of the Multigas Controller MKS 647C (4). The connections between the gas lines, devices and valves were sealed with specialized sealing tape. For the measurements, only not cycled[27] samples were used. For the flow rate measurements, no voltage was applied to a microvalve sample leaving it open. In this case the actual flow was that adjusted on the Multigas Controller. The adjustment was done with the steps of 5 sccm: 25 sccm, 30 sccm etc… At the point, where the maximum allowable flow through the valve was achieved, increase of the measured actual flow stopped. Similarly to the previous measurements, five samples per design were measured. The results are represented in Figure 4.19.

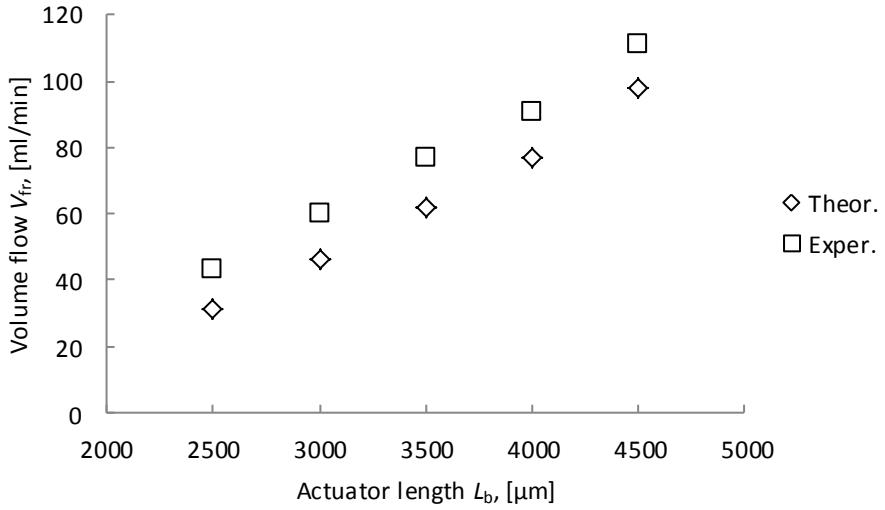

Figure 4.19: Results of the flow rate measurement for different microactuator designs

The results show approximately 5 to 10 ml/min higher flow rates for all the designs. The reason of this can be in a leakage somewhere in the measurement system. In order to prove, which of the designs showed the most stable results, a standard deviation was calculated (Fig. 4.20).

[27] No drop-tests, no temperature cycling

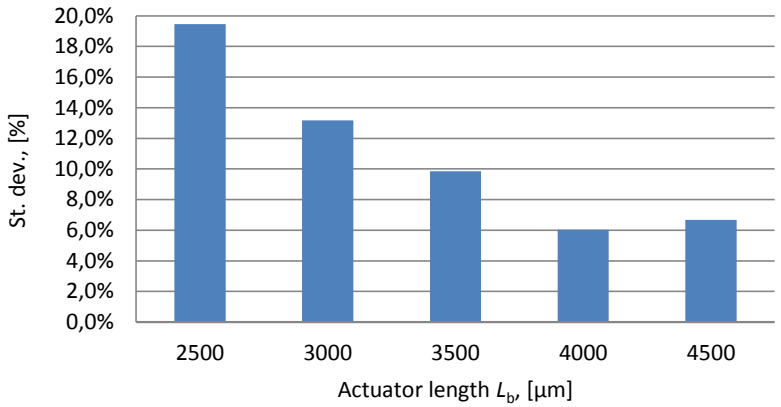

Figure 4.20: Standard deviation in % for microvalve flow rate measurements

For the designs 1.x and 2.x (L_b = 2500 µm and 3000 µm) very high standard deviations were received meaning that the flow rate is unstable for those designs. The designs 3.x, 4.x and 5.x showed better behavior, though standard deviations remained relatively high.

In order to prove the functionality of the valve in a closed state, a pull-in voltage was applied to it as nitrogen was flowing through. The actual flow values dropped as the necessary voltages were applied meaning the open/close function was performed.

4.3.2 Microvalve functionality test: summary

A gas-flow measurement setup was built in order to prove the ability of the microvalves to deliver the calculated flows. The tests of microvalve functionality showed the results close to theoretical ones (Fig. 4.19). Nevertheless, high values of standard deviation force the assumption that either design, or calculations or rather measurement method and measurement set up must be improved. It is assumed that for such a precise test, a vacuum chamber is needed, in which leak-proof electrical connections and gas-lines must be foreseen.

5 Conclusions and suggestions for future research

In this work, a technological process for production of electrostatically driven curved microactuator for pneumatic applications was presented. Using the process, fifteen design variants of the microactuator integrated into a 2/2-microvalve chip were produced and then characterized. The microvalve proved to deliver the flow rates up to 110±5 ml/min at differential pressure of 2 bar and driving voltages of 11,6 V. As a basis for this work, a broad overview of the existing microactuators and microvalves as well as the techniques of their production was given.

During the design of the actuator, a model for the calculations of the mechanical and electrical properties of the actuator was proposed. Basic microvalve performance was also estimated. Electrostatic actuation principle was chosen for its good scaling properties to small dimensions, low power consumption, smaller size and higher switching speed. Curved shape of the actuator allowed to reduce the pull-in voltage and thus to increase the amplitude of motion as compared to the parallel-plate structures.

Nickel was chosen as a material of the actuator for its good mechanical properties and relative simplicity of processing. Double layer nickel electroplating was used to produce the microactuator. The layers have different stress gradients controlled by current density during the electroplating process, making it possible to achieve the desired bending of the structure. Compared to bimetallic bending cantilever actuators, the curvature of the single-metal beam is less dependable on temperature and aging. Thus, more stable performance under changing working conditions was ensured. In order to avoid sticking of the microactuator to the isolation layer in the closed state, an array of stand-off bumps was added on the back-side of the beam. These bumps reduce the contact area and increase the distance between the actuator and the isolation layer.

The technology developed in this work is a 6 photolithography layer process based on standard 4-inch Si substrates. But the possibility of alternative substrates utilization was also examined. The study showed that though there are many materials, which could be readily used as substrates (ceramics, FR-4, glass), from technological and financial point of view, Si remains the best choice. The closest competitor could be Al_2O_3 ceramic (alumina). This material is very widely used in industry; its costs are comparable with Si and it is available in a shape of wafers. Moreover, ceramic is a natural insulator. This fact saves oxidation step and potentially reduces the costs of the process. Thus, several types of Al_2O_3 of different purity were checked on their technological suitability to the process developed in this work. Wet etching, photolithography and electroplating with these substrates were studied. The studies revealed that there was no simple and cheap way to remove ceramic material by wet etching, though some slow removal took place in case of type Rubalit 708. Photolithography was in general possible, but the alignment of a mask to the pattern on the substrate surface in the yellow room was very problematic since no structures could be seen under the microscope even on the finest surface with Ra = 0,1 μm. Electroplating revealed no problems and run as usually done with

conventional Si substrates. Summarizing the above mentioned facts, it was decided to go on with Si substrates leaving ceramic for future R&D work.

The design of the technological flow was divided into three main phases:

- fabrication of a passive actuator (no bottom electrode)
- fabrication of an active actuator (with bottom electrode and contacts)
- process development for integration of the actuator into a microvalve

The first phase included several runs of subsequent surface micromachining steps focused on electroplating and wet etching of sacrificial layers in order to check the reproducibility of the deposition process and correspondence of the actuators final geometry to the theoretical expectations.

During the second phase, bottom electrodes were added in order to make the actuator functional. RIE dry etching method was developed to achieve well defined bottom electrodes.

In the last phase, a through silicon microchannel made by DRIE was introduced underneath the actuator structure. All the separately developed flow steps were combined into a final technological flow resulting in a 2/2 microvalve chip.

During characterization, mechanical stability of the actuators and microvalves as well as the electrical performance and flow rates were studied. Mechanical robustness was examined by means of drop, temperature and shear-tests. All the samples passed mechanical tests successfully. Shear-tests of the microactuator showed good adhesion of the beams to the underlying layers (up to 2 N) However, some weakening of the shear-force was observed after thermal and drop-down cycling. Pull-in voltage was examined before and after temperature and drop-down tests. The values of the pull-in voltage appeared to be slightly higher (approx. 0,5 – 0,6 V) for two design variants. It was proved that temperature and drop-down loads did not significantly influence this parameter. The deflection of the actuator beams was measured before and after thermal cycling and also showed the results comparable with theoretical expectations in both cases. The measurements of the actuators reaction time could not be performed. But theoretically calculated results lie in the region of 3 ms that corresponds to the specifications.

Measured flow rates of the microvalves (up to 110±5 ml/min) were also about 10 ml/min higher than the expected theoretical ones. In this case, some leakage in the measurement system was responsible for this offset.

The process and the system designed in this work resulted in a robust, effective and cheap microactuator that could be integrated into a microvalve and provide performance comparable to the similar systems reported in literature. However, the realization of the complete microvalve on a single substrate can be seen as a step forward in comparison to the other systems. Moreover, the process developed in this work possesses high flexibility and can be used not only for the production of microvalves, but also for microrelays and other MEMS components.

Future research work must be concentrated on further examination of the alternative substrates and higher effectiveness of the electroplating process. New electrode isolation materials and actuator geometries can be investigated. The methods of system characterization must be improved. System packaging concept should be developed.

References

[1] J. Perkins, "MEMS Market Overview," Yole Development, Anaheim, 2010.

[2] P. Rai-Choudhury, MEMS & MOEMS: technology and application, SPIE - The International Society for Optical Engineering, 2000, pp. 35-39.

[3] Seiko Epson Corporation, "Digital Photography," 27 March 2007. [Online]. Available: http://dpnow.com/3762.html. [Accessed 26 02 2011].

[4] J. Jahns and K.-H. Brenner, Microoptics: from technology to application, Springer-Verlag, New York, LLC, 2004.

[5] J. K. Robertson, "An electrostatically-actuated integrated microflow controller," Michigan, 1996.

[6] F. Ibrahim, N. Abu Osman, J. Usman and N. Kadri, "A review of MEMS drug delivery in medical application," in *Biomed 06, IFMBE Proceedings* , 2007.

[7] K. W. Oh and A. C. H., "A review of microvalves," *Journal of Micromechanics and Microengineering,* no. 16, pp. R13-R39, 24 March 2006.

[8] V. Varadan, K. Vinoy and K. Jose, RF MEMS and ther applications, John Wiley & Sons Ltd, 2003.

[9] J. G. Krovnik and O. Paul, MEMS: A practical guide to design, analysis and application, William Andrew Inc., 2006.

[10] R. G. Gilbertson and J. D. Busch, "A survey of micro-actuator technologies for future spacecraft missions," *The Journal of The British Interplanetary Society,* no. 49, pp. 129-138, 1996.

[11] Robert Bosch GmbH, "Bosch Sensor Datasheet," Robert Bosch GmbH, 2010.

[12] M. Tabib-Azar, Microactuators: Electrical, Magnetic, Thermal, Optical, Mechanical, Chemical and Smart Structures, Kluwer Academic Publishers, 1998.

[13] E. Quandt, "Magnetostriktive Schichten als Aktoren in der Mikrosystemtechnik," Karsruhe, 1993.

[14] I. Shimoyama, O. Kano and H. Miura, "3D Micro-structures folded by Lorentz force," in *Proceedings IEEE Transducers 1998*, 1998.

[15] M. J. Madou, Fundamentals of Microfabrication: the science of miniaturization, 2nd ed., CRC Press LLC, 2002.

[16] L. K. Lagorce, O. Brand and M. G. Allen, "Magnetic Microactuators Based on Polymer Magnets," *IEEE Journal of Microelectromechanical Systems,* vol. 8, no. 1, March 1999.

[17] G. T. Kovacs, Micomachined Transducers Sourcebook, WCB/McGraw-Hill, 1998.

[18] "Just What is Photostriction?," Montana State University, [Online]. Available:

http://www.physics.montana.edu/eam/photostriction/photostriction.htm. [Accessed 25 March 2011].

[19] K. Uchino and J. R. Giniewicz, Micromechatronics, Marcel Dekker Inc., 2003.

[20] R. Maeda, J. Tsaur, S. Lee and M. Ichiki, "Piezoelectric Microactuator Devices," *Journal of Electroceramics,* no. 12, pp. 89-100, 2004.

[21] A. Lee, D. Ciarlo, P. Krulevich, S. Lehew, J. Trevino and M. Northrup, "A Practical Microgripper by Fine Alignment, Eutectic Bonding and SMA Actuation," in *Proceedings of International Solid-State Sensors and Actuators Conference (Transducers '95)*, Stockholm, Sweden, 1995.

[22] D. Bien, S. Mitchell and H. Gamble, "Fabrication and characterization of a micromachined passive valve," *Journal of Micromechanics and Microengineering,* no. 13, pp. 557-562, 14 May 2003.

[23] S. Terry, J. Jerman and A. J.B., "A gas chromatographic air analyzer fabricated on a silicon wafer," *IEEE Trans. Electron Devices,* no. 26, pp. 1880-1886, 1979.

[24] K. Oh, A. Han, S. Bhansali and C. Ahn, "A low-temperature bonding technique using spin-on fluorocarbon polymers to assemble microsystems," *Journal of Micromechanics and Microengineering,* no. 12, pp. 187-191, 2002.

[25] S. Shoji and E. Masayoshi, "Microflow devices and systems," *Journal of Micromechanics and Microengineering,* no. 4, pp. 157-171, 1994.

[26] J. M. Park, "A piezoelectrically actuated cryogenic microvalve with integrated sensors," University of Michigan, Michigan, 2009.

[27] T. Ohnstein, T. Fukiura, J. Ridley and U. Bonne, "Micromachined Silicon Microvalve," in *Proceedings of IEEE Workshop on Micro Electro Mechanical Systems*, Napa Valley, CA, USA, 1990.

[28] X. Yang, A. Holke, S. Jacobson, J. Lang, S. M.A. and S. Umans, "An electrostatic, on/off microvalve designed for gas fuel delivery for the MIT microengine," *Journal of Microelectromechanical Systems,* no. 13, pp. 660-668, 2004.

[29] D. Roberts, H. Li, J. O. Steyn and S. Spearing, "A piezoelectric microvalve for compact high-frequency, high-differential pressure hydraulic micropumping systems," *Journal of Microelectromechanical Systems,* no. 12, pp. 81-92, 2003.

[30] T. Rogge, Z. Rummler and W. Schomburg, "Polymer micro valve with a hydraulic piezo-drive fabricated by the AMANDA process," *Sensors and Actuators,* no. 110, pp. 206-212, 2004.

[31] P. Shao, Z. Rummler and W. Schomburg, "Polymer micro piezo valve with a small dead volume," *Journal of Micromechanics and Microengineering,* no. 110, pp. 305-309, 2004.

[32] H. Jerman, "Electrically activated, normally closed diaphragm valves," *Journal of Micromechanics and Microengineering,* no. 4, pp. 210-216, 1994.

[33] M. Zdeblick, "Thermopneumatically-Actuated Microvalves and Integrated Electrofluidic Circuits," in *Solid-State Sensor and Actuator Workshop*, 1994.

[34] H. Takao, K. Miyamura, H. Ebi, M. Ashiki, K. Sawada and K. Ishida, "A MEMS microvalve with PDMS diaphragm and two-chamber configuration of thermo-pneumatic actuator for integrated blood test system on

silicon," *Sensors and Actuators,* no. 119, pp. 468-475, 2005.

[35] C. Rich and K. Wise, "A high-flow thermopneumatic microvalve with improved efficiency and integrated state sensing," *Journal of Microelectromechanical Systems,* no. 12, pp. 201-208, 2003.

[36] X. Yang, C. Grosjean and T. Y-C., "Design, fabrication, and testing of micromachined silicone rubber membrane valves," *Journal of Microelectromechanical Systems,* no. 8, pp. 393-402, 1999.

[37] N.-T. Nguyen and S. T. Wereley, Fundamentals and applications of microfluidics, Artech House, Inc., 2002.

[38] M. Kohl, D. Dittmann, E. Quandt and B. Winzek, "Thin film shape memory microvalves with adjustable operation temperature," *Sensors and actuators,* no. 83, pp. 214-219, 2000.

[39] P. Barth, "Silicon microvalves for gas flow control," in *Proceedings 8th Int. Conf. on Solid-State Sensors and Actuators (Transducers '95), and Eurosensors IX*, Stockholm, Sweden, 1995.

[40] C. Pemble and B. Towe, "A miniature shape memory alloy pinch valve," *Sensors and Actuators,* no. 77, pp. 145-148, 1999.

[41] I. Fazal, M. Louwerse, H. Jansen and M. Elwenspoek, "Stepper Motor Actuated Microvalve," *Journal of Physics: Conference Series,* no. 34, pp. 1032-1037, 2006.

[42] C. Goll, W. Bacher, B. Büstgens, D. Maas, M. W. and W. Schomburg, "Microvalves with bistable buckled polymer diaphragms," *Journal of Micromechanics and Microengineering,* no. 6, pp. 77-79, 1996.

[43] S. Bohm, G. Burger, M. Korthorst and F. Roseboom, "A micromachined silicon valve driven by a miniature bi-stable electro-magnetic actuator," *Sensors and Actuators,* no. 80, pp. 77-83, 2000.

[44] D. Bosh, B. Heimhofer, G. Muck, H. Seidel, U. Thumser and W. Welser, "A silicon microvalve with combined electromagnetic/electrostatic actuation," *Sensors and Actuators,* no. 37/38, pp. 684-692, 1993.

[45] D. Dissanayake and S. Al-Sarawi, "Designing remotely activated microvalves for biomedical applications," SPIE Newsroom, 2007.

[46] "Physorg.com," 20 May 2005. [Online]. Available: http://www.physorg.com/news4188.html. [Accessed 12 March 2011].

[47] "Wikipedia The free Encyclopedia," [Online]. Available: http://en.wikipedia.org/wiki/Coulomb's_law. [Accessed 10 May 2011].

[48] V. Kaajakari, "MEMS Material," [Online]. Available: http://www.kaajakari.net/~ville/research/tutorials/pull_in_tutorial.pdf. [Accessed 12 May 2011].

[49] D. Petrov, W. Lang and W. Benecke, "A nickel electrostatic curved beam actuator for valve applications," in *Proceedings Eurosensors XXIV, September 5-8*, Linz, Austria, 2010.

[50] J. Schimkat, "Grundlagen und Modelle zur Entwicklung und Optimierung von Silizium-Mikrorelais," Berlin, 1996.

[51] M. Becker, "Entwurf einer Antriebsstruktur für ein MST-basiertes Mikrorelais zur Anwendung im Automobil," Bremen, 1999.

[52] "Wikipedia the Free Encyclopedia," [Online]. Available: http://en.wikipedia.org/wiki/Neutral_axis. [Accessed 14 May 2011].

[53] G. Gerlach and W. Dötzel, Grundlagen der Mikrosystemtechnik, München: Carl Hansen Verlag, 1997.

[54] Y. Hu, J. Yang and S. Kitipornchai, "Pull-in analysis of electrostatically actuated curved micro-beams with large deformation," *Smart Materials and Structures,* no. 19, 17 May 2010.

[55] K.-S. Ou, K.-S. Chen, T.-S. Yang and S.-Y. Lee, "A Novel Semianalytical Approach for Finding Pull-In Voltages of Micro Cantilever Beams Subjected to Electrostatic Loads and Residual Stress Gradients," *Journal of Microelectromechanical Systems,* vol. 20, no. 2, pp. 527-537, 2011.

[56] C. W. Leow, M. Abu Bakar and M. K. Norazan, "Analytical Modeling For Determination Of Pull-In Voltage For An Electrostatic Actuated MEMS Cantilever Beam," in *ICSE2002 Proceedings*, Penang, Malaysia, 2002.

[57] "Wikipedia the free Encyclopedia," [Online]. Available: http://en.wikipedia.org/wiki/Paschen's_law. [Accessed 01 June 2011].

[58] L. Germer, "Electrical breakdown between close electrodes in Air," *Journal of Applied Physics,* vol. 30, no. 1, pp. 41-47, 1959.

[59] E. Clark, R. Yeske and H. Birnbaum, "The Effect of Hydrogen on the Surface Energy of Nickel," *METALLURGICAL TRANSACTIONS A,* vol. 11A, 1980.

[60] S. Timoshenko and S. Krieger, Theory of Plates and Shells, New York: McGraw-Hill, 1959.

[61] I. Voiculescu, M. E. Zaghloul, R. A. McGill, E. J. Houser and G. K. Fedder, "Electrostatically Actuated Resonant Microcantilever Beam im CMOS Technology for the Detection of Chemical Weapons," *IEEE Sensor Journal,* vol. 5, no. 4, 2005.

[62] M. Kampmann, "Theoretische Bestimmung der Geometrie- und Durflussparameter eines Mikroventils," Bremen, 2010.

[63] H. Sigloh, Technische Fluidmechanik, 6 ed., Springer, 2008.

[64] S. Messner, "Elektrostatisch angetriebenes 3/2-Wege-Mikroventil für pneumatische Anwendungen," Freiburg im Breisgau, 2000.

[65] A. Henning, Interviewee, *Personal communication.* [Interview].

[66] "Richter Elektronik Handelsb[ro Heise, Produkte," [Online]. Available: http://www.richterelektronik.de/prod_mx203.htm. [Accessed 03 September 2011].

[67] M. Köhler, Ätzverfahren für die Mikrotechnik, Wiley-VCH, 1998.

[68] B. Zhou and F. W. Ramirez, "Kinetics and Modeling of Wet Etching of Aluminum Oxide by Warm Phosphoric Acid," *Journal of Electrochemical Society,* vol. 143, no. 2, pp. 619-623, 1996.

[69] D. Krell, Interviewee, *Personal communication (e-mail).* [Interview].

[70] A. Bödecker, Interviewee, *Personal communication (e-mail).* [Interview]. 23 April 2009.

[71] D. Petrov, "Prozessentwicklung für die Herstellung elektrostatischer Abrollaktoren für pneumatische Mikroventile," Bremen, 2009.

[72] D. Petrov, "Modeling, fabrication and characterization of internal connections for bare die applications," Hamburg, 2006.

Acknowledgments

My warmest thanks go to Professor Dr.-Ing. Wolfgang Benecke for all of his help, support and belief. I would also like to thank Professor Dr.-Ing. Walter Lang who provided a lot of advice and support during my work on the project.

My very special thanks go to Azat Ibragimov whose share of experience and assistance were invaluable especially for the theoretical calculations and practical work in a clean room. He also helped me very much with some literature sources.

Additionally, I would like to acknowledge the technical assistance of Mohammad Shafi for his help with electroplating and lithography, Ingrid Michels for her collaboration with samples preparation and dicing. My thanks go also to Adam Sklorz for his friendly support and advise every time it was needed.

I would like to thank all the team of the IMSAS for their kind collaboration and warm atmosphere they created during my work.

Finally, I would like to say thank you to my wife, Kira, to my parents and friends for a positive influence they all had on my attitude.

Appendix I

Photolithography masks

This appendix is a collection of the patterns used to produce foil photomasks. The patterns were designed by the author. Due to the microscopically small size of some structures, not all of them can be recognizable on the drawings.

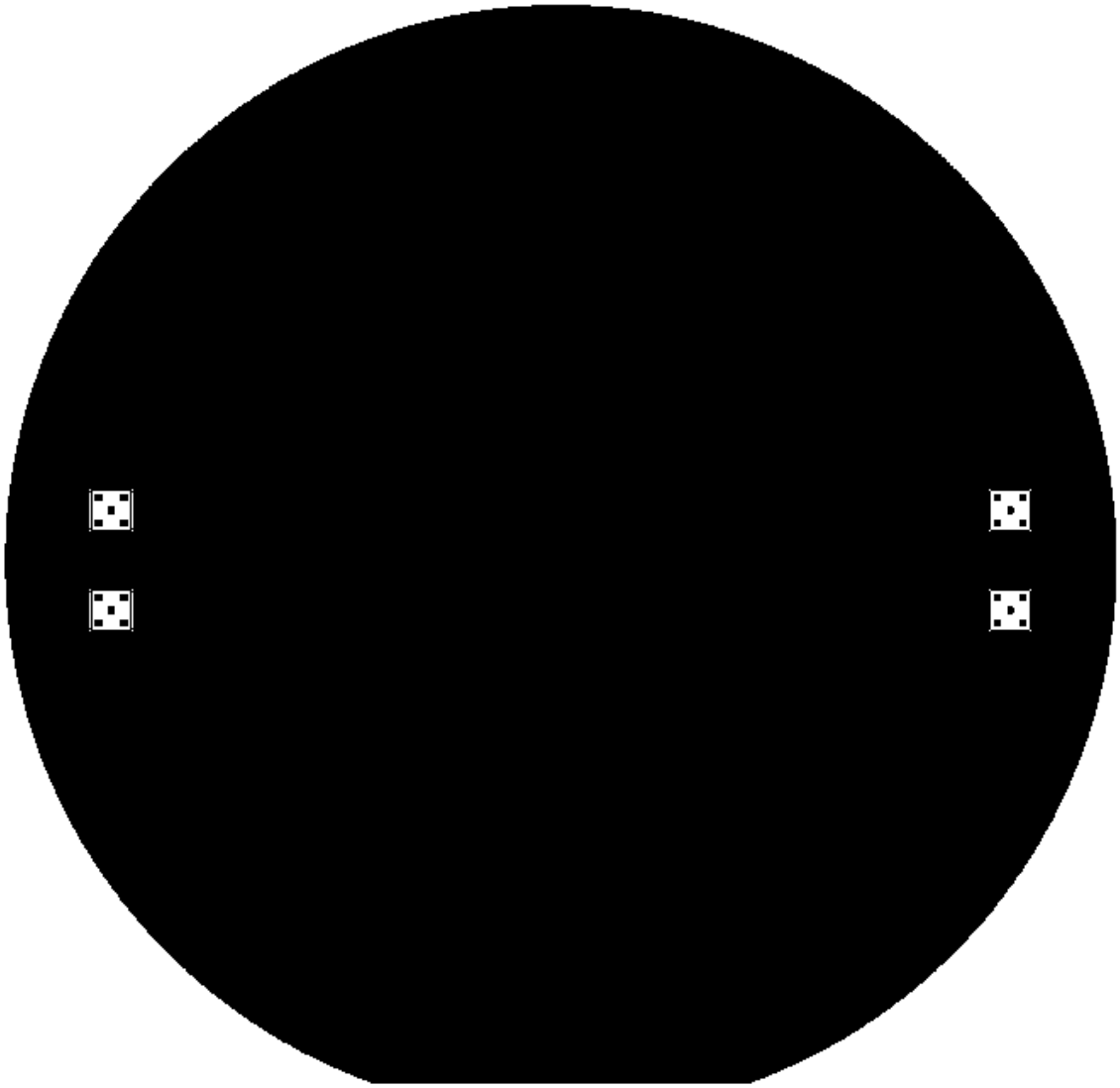

Figure A1.1: Mask 1 Back-side alignment markings

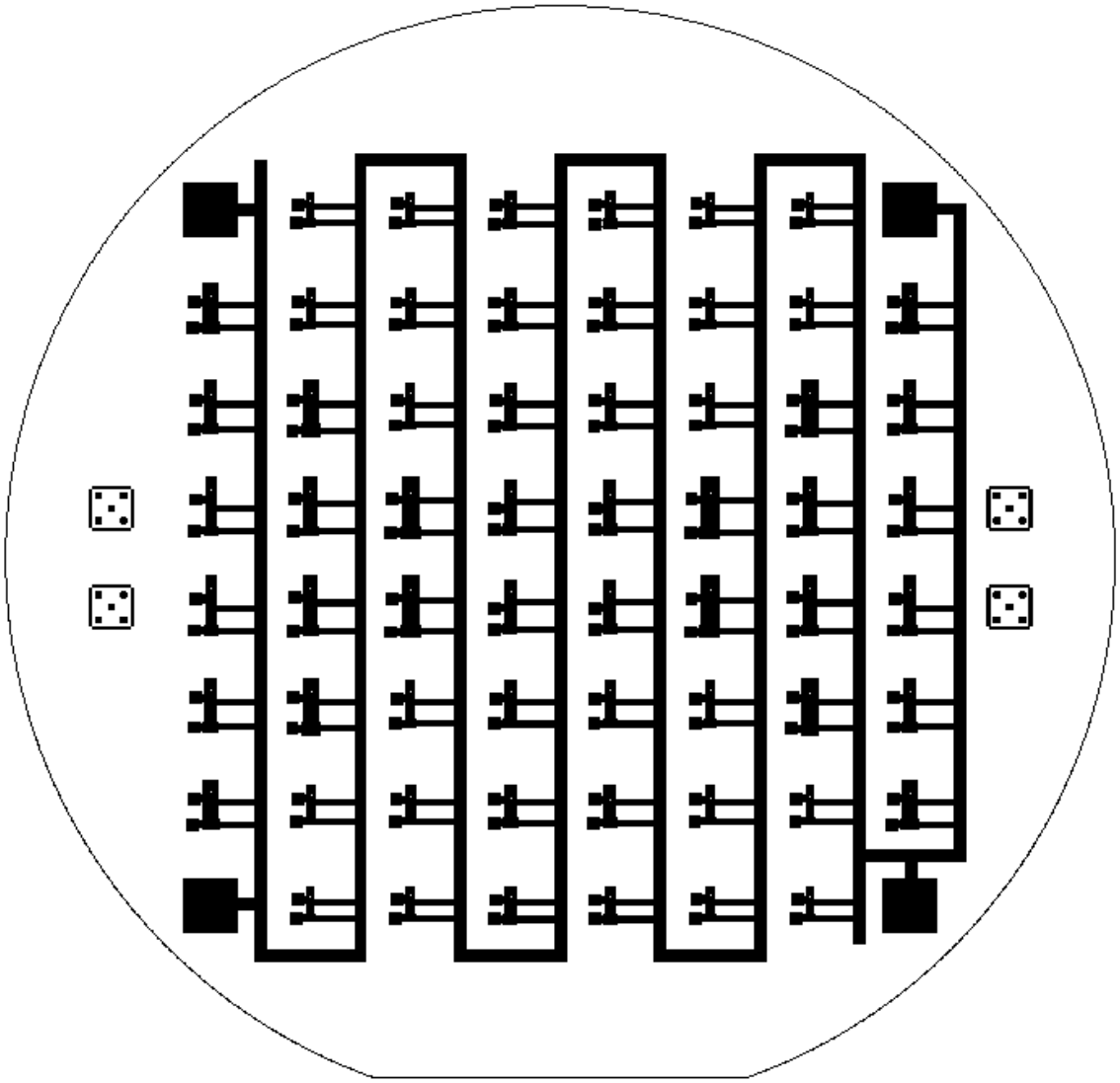

Figure A1.2: Mask 2 Bottom electrodes

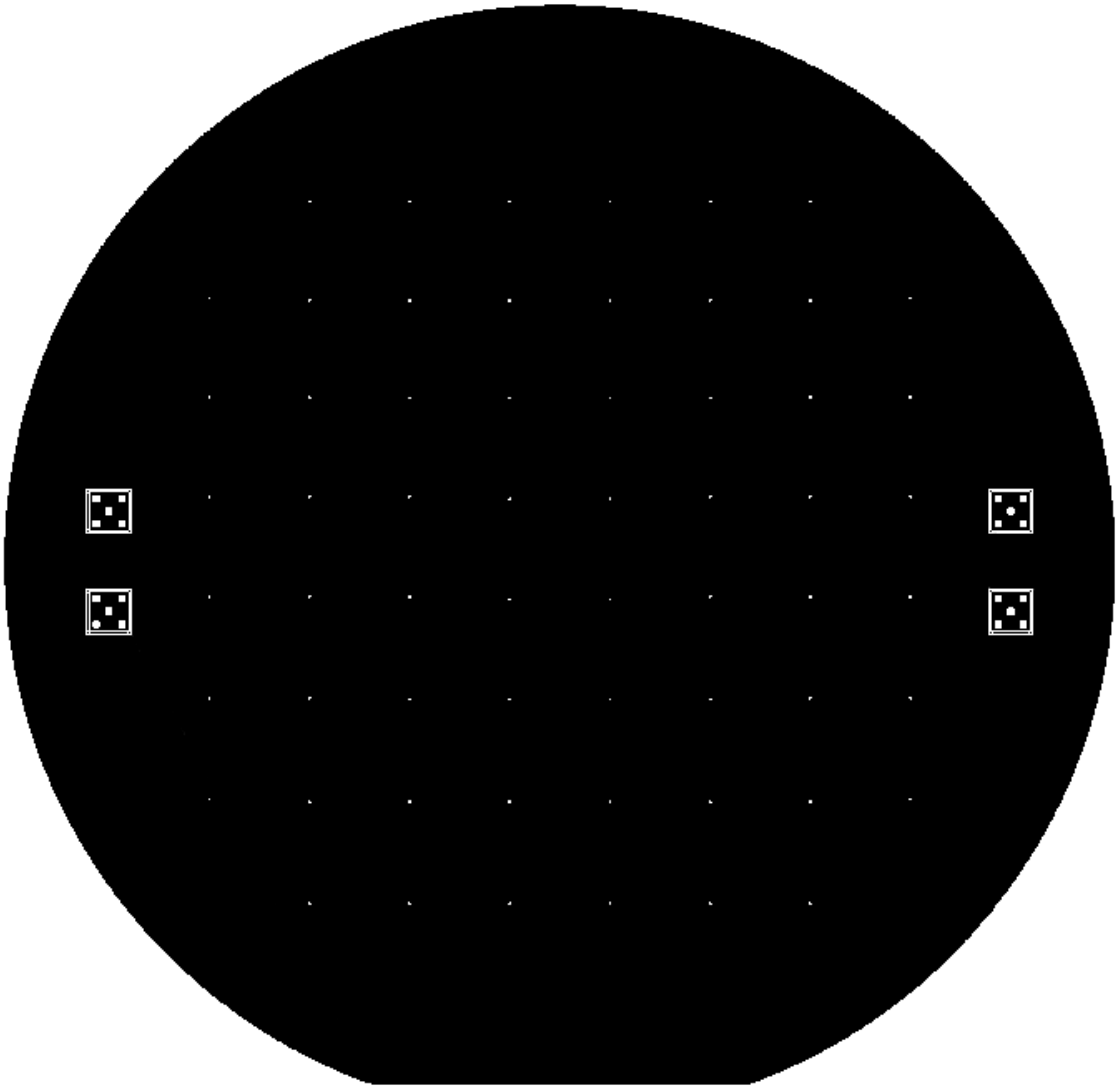

Figure A1.3: Mask 3 Gas-inlet channels

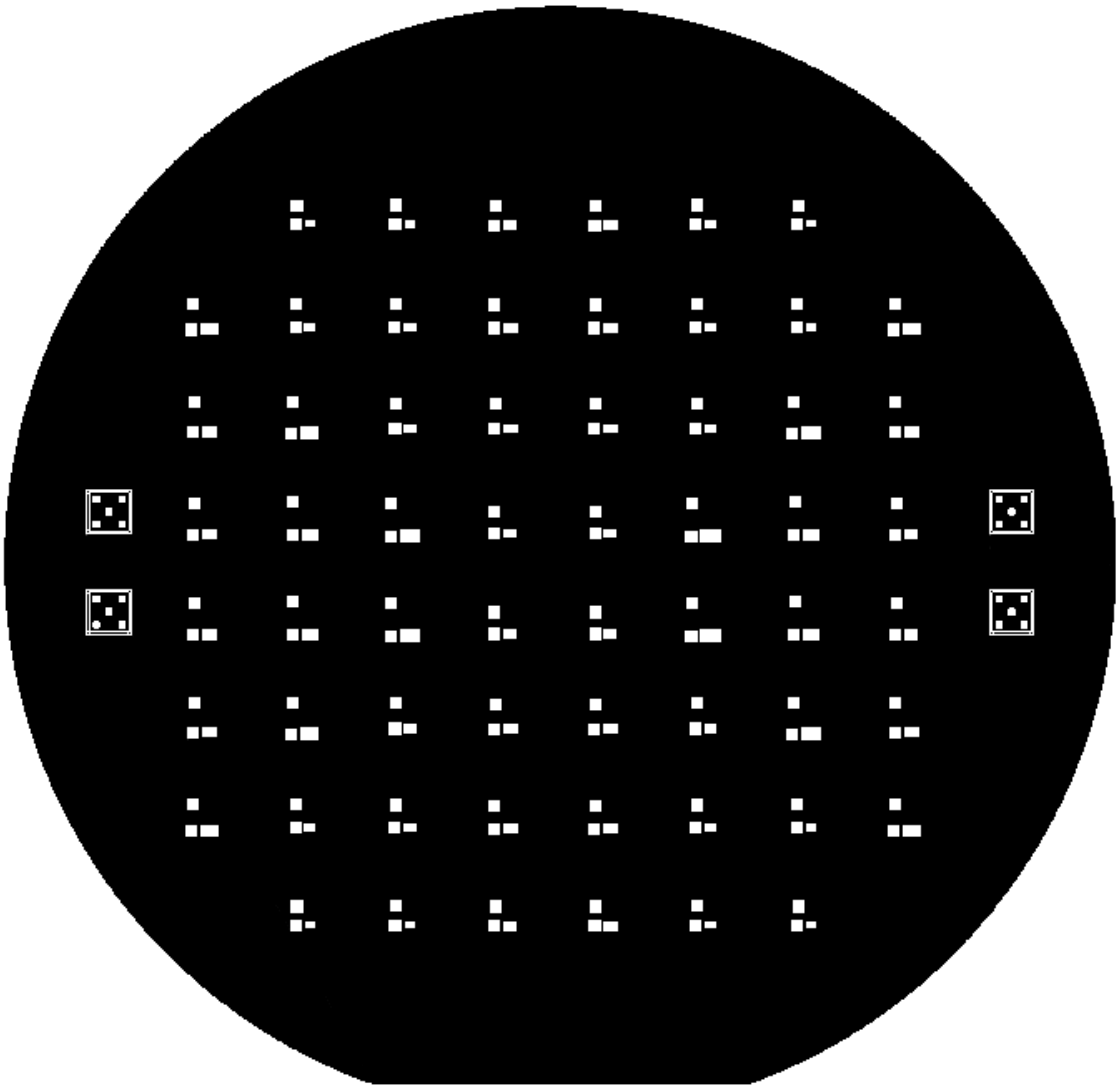

Figure A1.4: Mask 4 Anchor and electrodes openings

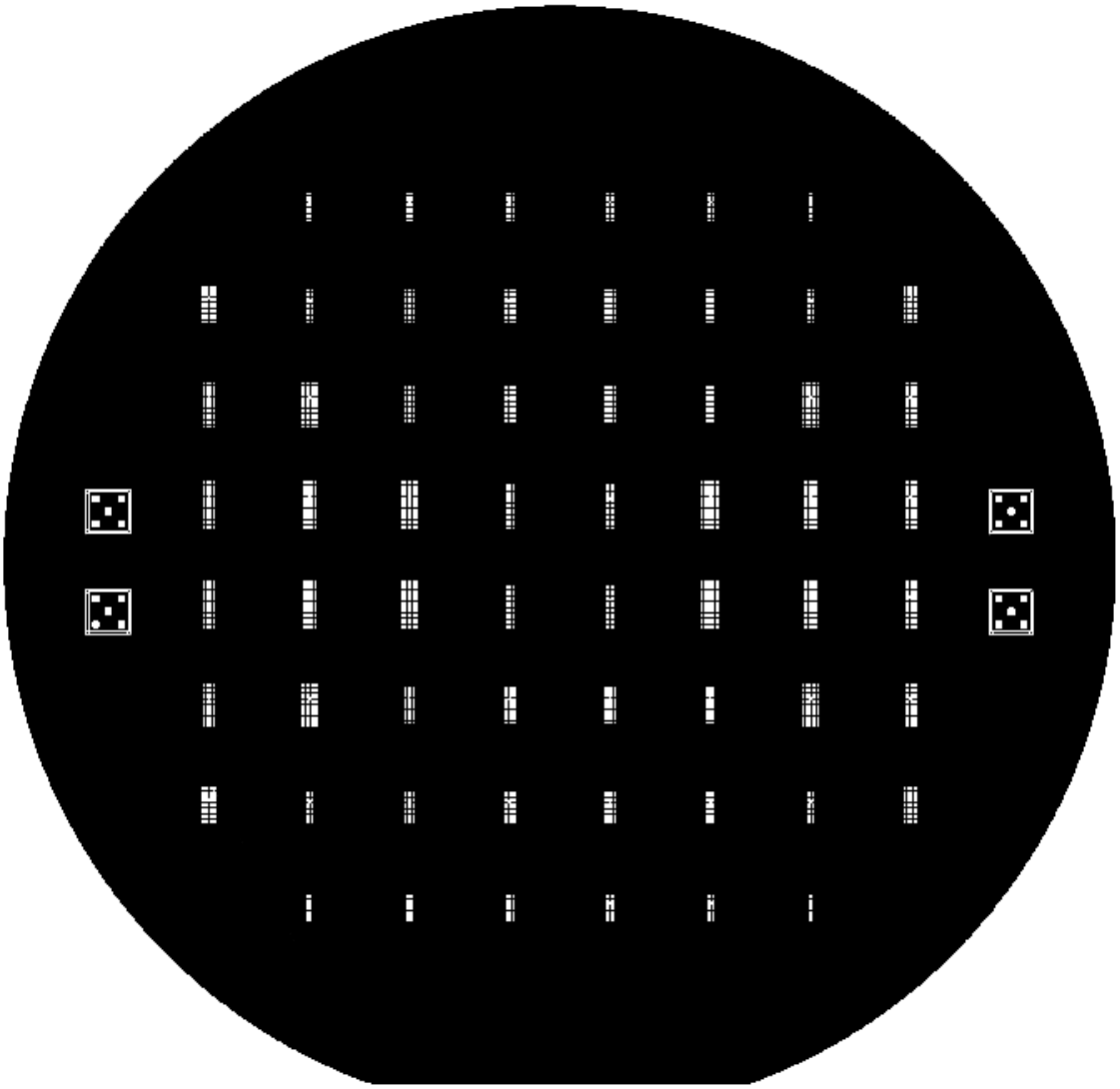

Figure A1.5: Mask 5 Stand-off bumps

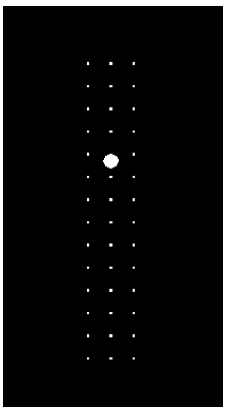

Figure A1.6: Mask 5 Stand-off bumps (one structure magnified)

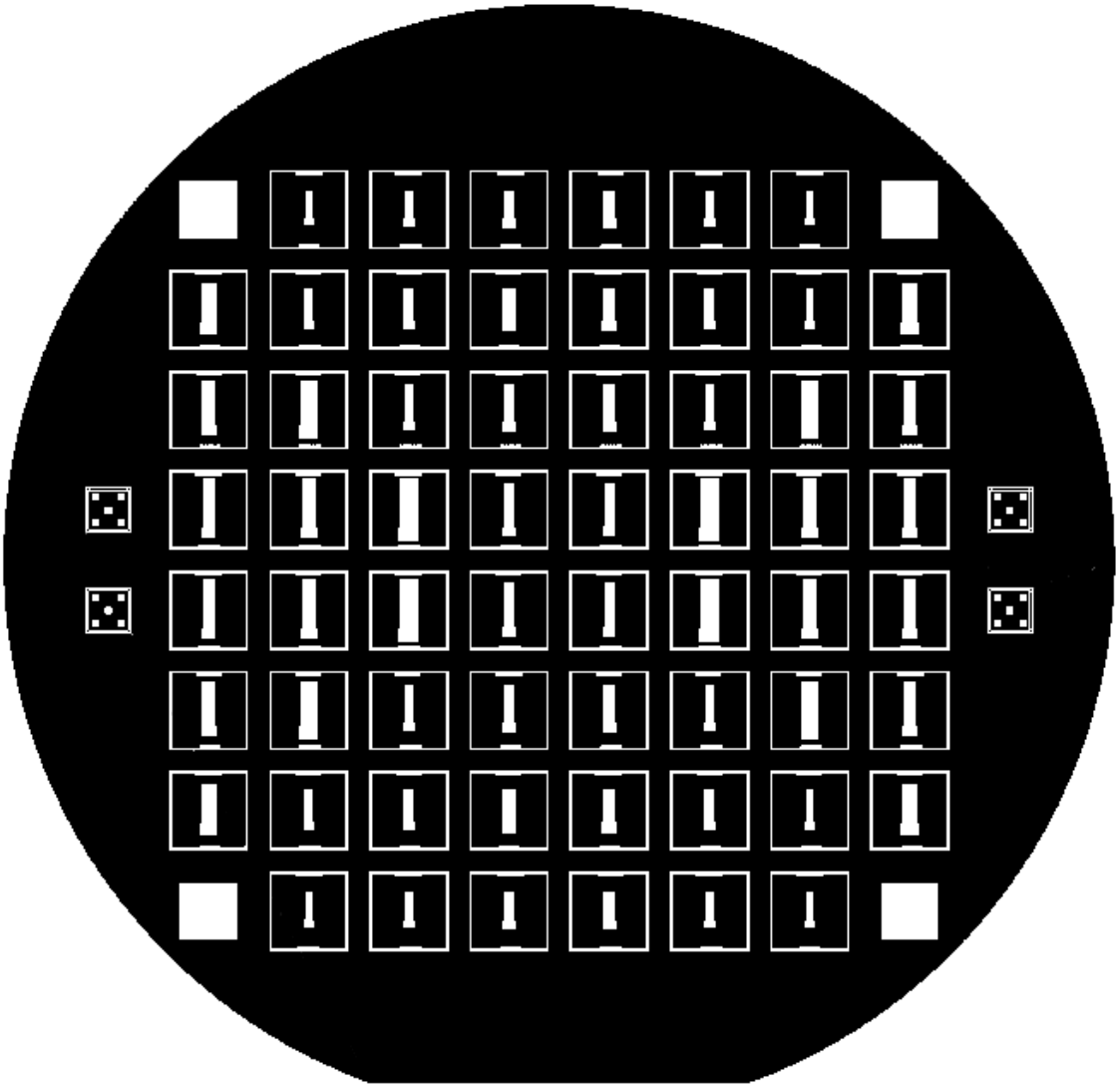

Figure A1.7: Mask 6 Actuator

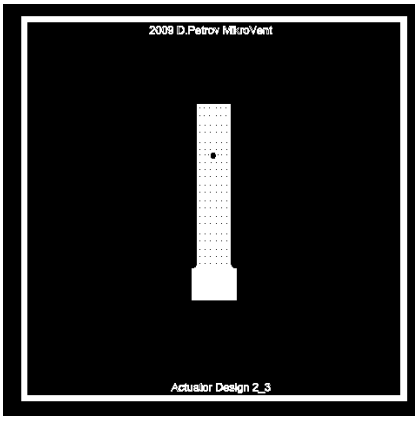

Figure A1.8: Mask 6 Actuator (one structure magnified)

Appendix II

A map of microactuator design distribution over the waver

This Appendix contains a drawing explaining how the designs were distributed on the wafer

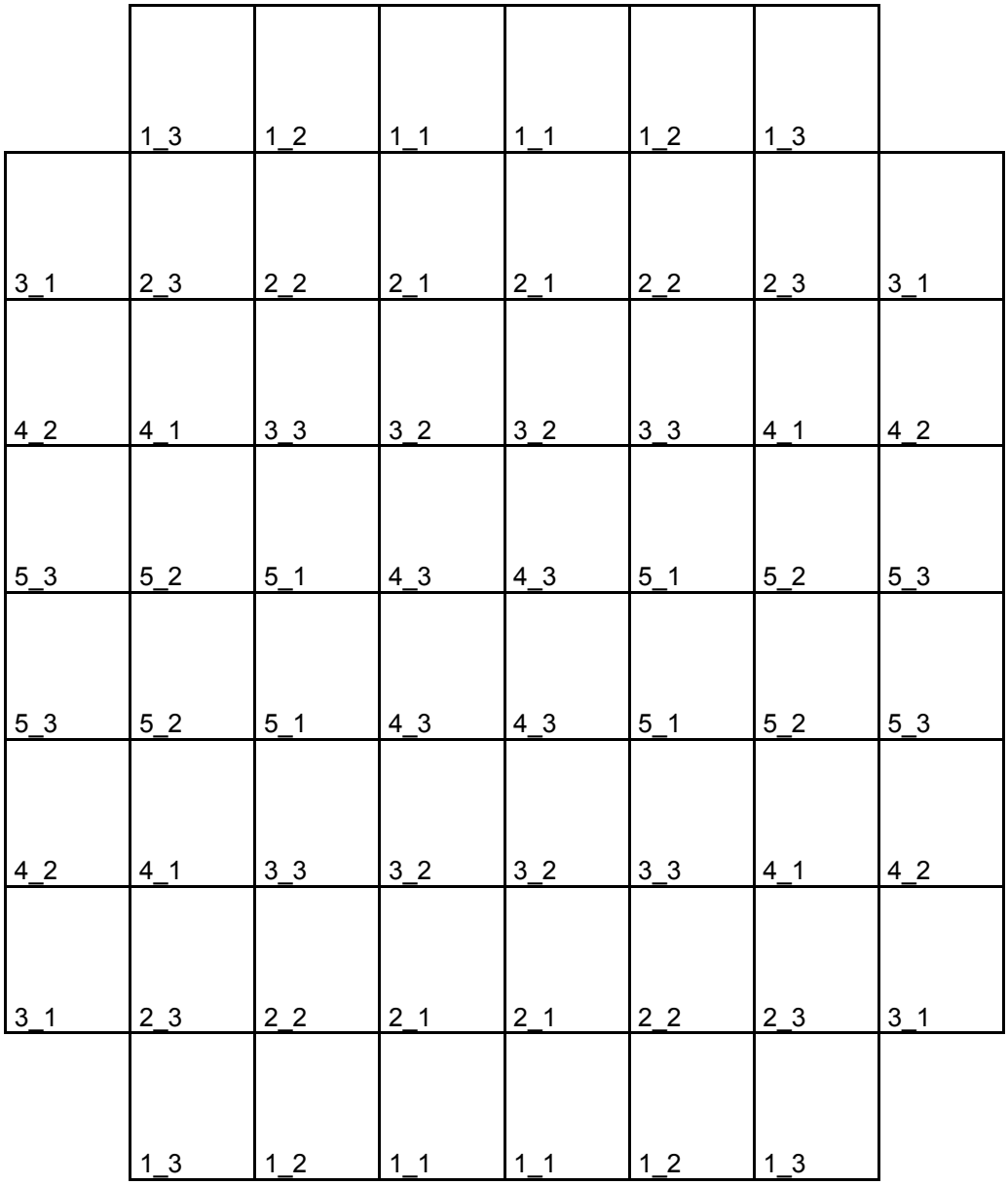

Figure A2.1: Microactuator designs distribution on the wafer

Appendix III

Microvalve housing/holder for flow rate measurements

This Appendix contains a technical drawing used by tool operators in the workshop to make a housing/holder used to characterize the flow rate of a microvalve.

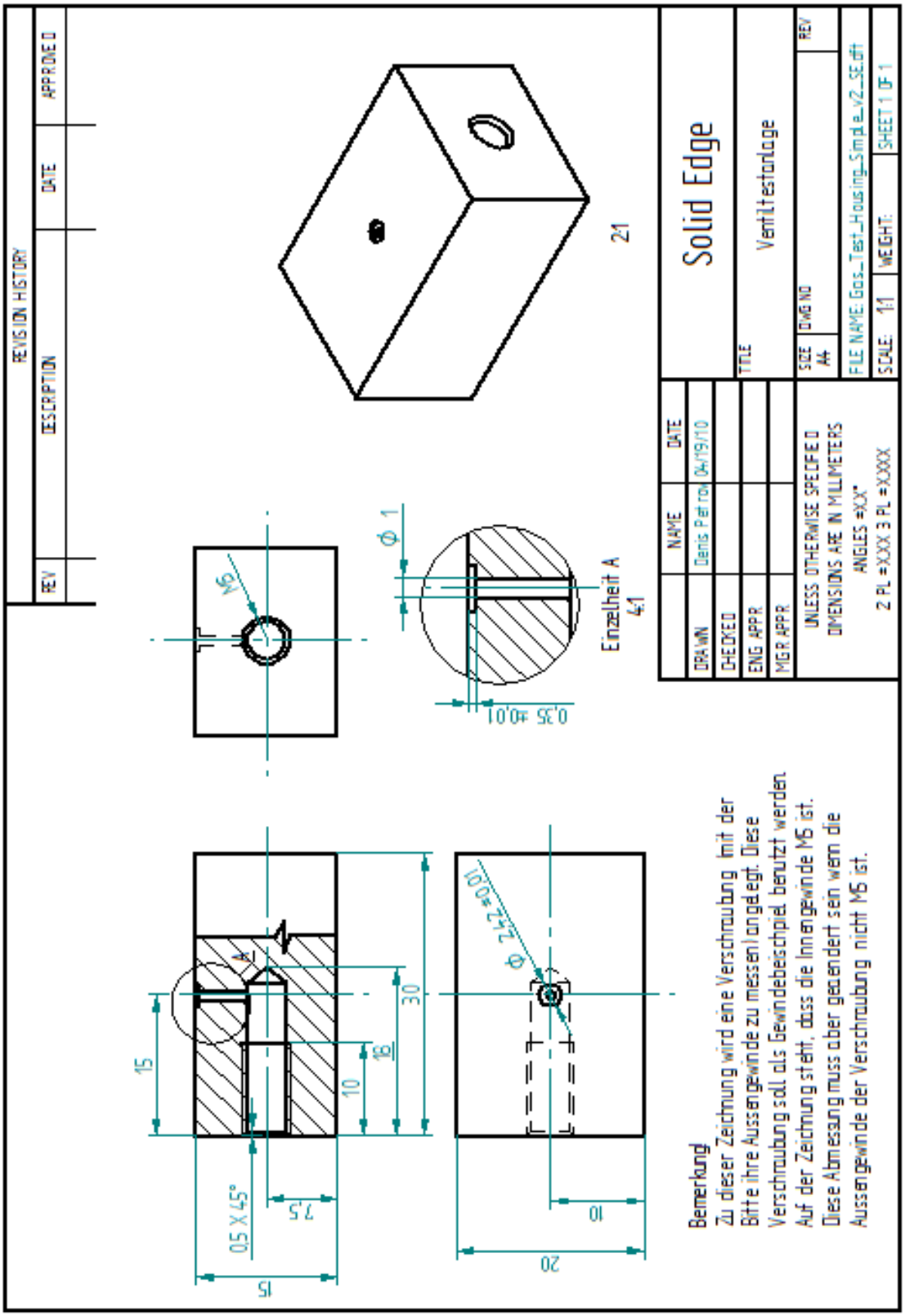

Figure A3.1: Microvalve housing/holder for flow rate measurements

List of figures

List of tables

Declaration

Herewith, I assure that present work has been done independently, with use of listed literature sources and additional materials.

Denis A. Petrov
Pinneberg, March 2012